PRACA
DOKTORSKA

PhD Thesis

Molecule imprinting in molecular biology: from determination of oligonucleotides to synthesis of new biocompatible polymer materials

Katarzyna Bartołd

Supervisor
Prof. Włodzimierz Kutner, Ph.D., D.Sc.

Auxiliary supervisor
Agnieszka Pietrzyk-Le, Ph.D.

Molecular
Films
Research

Kutner
Group

The thesis prepared within the International Doctoral in Chemistry Studies at the Institute of Physical Chemistry of the Polish Academy of Sciences in Warsaw in the Task Team of Molecular Films Research

Warsaw, June 2019

Statement of originality

I, Katarzyna Bartold, confirm that the research included within this thesis was carried out by myself or in collaboration with and supported by others, which is described in acknowledgements. Moreover, the previously published material is listed below.

I attest that I have exercised reasonable care to ensure that the work is original, and does not to the best of my knowledge break any Polish law, infringe any third party's copyright or other Intellectual Property Right, or contains any confidential material.

I accept that the Polish Academy of Sciences has the right to use plagiarism detection software to check the electronic version of the thesis.

I confirm that my thesis has previously not been submitted for the award of a degree by IPC PAS or any other institute or university.

The copyright of this thesis rests with the author and no quotation from it or information derived from it may be published without the prior written consent of the author.

Signature:

Date:

Acknowledgements

First of all, I would like to express my sincere gratitude to my supervisors, Professor Włodzimierz Kutner and Doctor Agnieszka Pietrzyk-Le, for proposing this PhD project and giving me the opportunity to accomplish it. I am very grateful for their support, scientific guidance and patience.

I deeply thank all members of the Task Team of Molecular Films Research for their kindness, help, and support. Especially, I am thankful to Doctor Tan-Phat Huynh for introducing me to the field of molecular imprinting, teaching me new techniques, and giving me scientific advices at the beginning of my studies.

Moreover, I would like to thank my colleagues, particularly Aga, Karolina, and Patrycja, for their friendship and emotional support through my PhD studies.

Besides, I express my gratitude to:

- Prof. D'Souza and Dr. Marta Sosnowska for synthesizing functional monomers **11**, **12**, and **13**
- Dr. Paweł Borowicz and Dr. Jacek Jemielity for performing PM-IRRAS experiments and discussing nucleic acid interactions
- Prof. Tiziana Benincori for providing cross-linking monomer **14**
- Prof. Francesco Sannicolò, Prof. Patrizia R. Mussini, and Dr. Silvia Cauteruccio for synthesizing cross-linking monomer **14** and PNAs **6**, **7**, **8,** and **9**
- M.Sc. Karolina Gołębiewska for AFM imaging
- Dr. Zofia Iskierko for EG-FET involving experiments
- Dr. Małgorzata Wszelaka-Rylik for assistance in the isothermal titration calorimetry experiments
- Dr. Alexandra Siklitskaya and Dr. Piotr Zaleski-Ejgierd for DFT calculations
- Prof. Wojciech Lisowski for performing XPS experiments
- Dr. Maciek Cieplak and Dr. Ievgen Obraztsov for help with drawing structural formulas of organic compounds and artwork
- Mr. Jerzy Szaniawski for artwork.

Finally, I wish to express my deep love and appreciation to my husband and my other close family members for their continuous support, encouragement, and help.

Publications

Papers published

1. Sannicolò, F.; Mussini, P. R.; Benincori, T.; Martinazzo, R.; Arnaboldi, S.; Appoloni, G.; Panigati, M.; Quartapelle Procopio, E.; Marino, V.; Cirilli, R.; Casolo, S.; Kutner, W.; Noworyta, K.; Pietrzyk-Le, A.; Iskierko, Z.; **Bartold, K.**, Inherently Chiral Spider-Like Oligothiophenes. *Chem. Eur. J.* 22, **2016**, 10839-47 (2017/2018 Impact factor: 5.16).

2. Iskierko, Z.; Sharma, P. S.; **Bartold, K.**; Pietrzyk-Le, A.; Noworyta, K.; Kutner, W. Molecularly imprinted polymers for separating and sensing of macromolecular compounds and microorganisms, *Biotechnol. Adv.* 34, **2016**, 30–46 (2017/2018 Impact factor: 11.452).

3. **Bartold, K.**; Pietrzyk-Le, A.; Huynh, T-H.; Iskierko, Z.; Sosnowska, M.; Noworyta, K.; Lisowski, W.; Sannicolò, F.; Cauteruccio, S.; Licandro, E.; D'Souza, F.; Kutner, W., Programmed transfer of sequence information into molecularly imprinted polymer (MIP) for hexa(2,2'-bithien-5-yl) DNA analogue formation towards single nucleotide polymorphism (SNP) detection. *ACS Appl. Mater. Interfaces* 9, **2017**, 3948-3958 (2017/2018 Impact factor: 8.097).

4. **Bartold, K.**; Pietrzyk-Le, A.; Golebiewska, K.; Lisowski, W.; Cauteruccio, S.; Licandro, E.; D'Souza, F.; Wlodzimierz Kutner, W., Oligonucleotide Determination via Peptide Nucleic Acid Macromolecular Imprinting in an Electropolymerized CG-Rich Artificial Oligomer Analogue, *ACS Appl. Mater. Interfaces* 10, **2018**, 27562–27569 (2017/2018 Impact factor: 8.097).

5. **Bartold, K.**, Pietrzyk-Le, A., Lisowski, W., Karolina Golebiewska, Siklitskaya, A., Borowicz, P., Shao, S., D'Souza, F., and Kutner, W., Promoting bioanalytical concepts in genetics: A TATA box molecularly imprinted polymer as a small isolated fragment of the DNA damage repairing system. *Mater. Sci. Eng. C.* 100, **2019**, 1-10 (2017 Impact factor: 5.080).

6. **Bartold, K.**, Pietrzyk-Le, A., D'Souza, F., and Kutner W., *Trends Biotechnol.*, **2019**, in press, "Oligonucleotide analogues and mimics for macromolecular biocompounds sensing". DOI:10.1016/j.tibtech.2019.04.003 (2017/2018 Impact factor: 13.578).

Patents awarded and patent applications

1. Patent awarded

1.1 **Bartołd, K.**, Pietrzyk-Le, A., Huynh, T.-P., Iskierko, Z., Noworyta, K., Sosnowska, M., Lisowski, W., Kutner, W., Sannicolò, F., Mussini, P. R., Polish Pat. No. PL-229917, 14 March 2016, Appl., No. P-409328, published in BUP 29 August 2014, „1-Tyminooctan 4-(di-2,2'-bitien-5-ylometylo)fenylu i sposób jego wytwarzania, warstwa przewodzącego polimeru wdrukowywanego molekularnie z zastosowaniem pochodnych tiofenu i sposób jej wytworzenia oraz jej zastosowanie do selektywnego wykrywania i oznaczania oligonukleotydu TATAAA" ("New DNA probe containing derivatives of thiophene and method for producing it, conductive layer of the polymer in-printed by molecular typing method using these derivatives and method for producing it, as well as the application of this probe for selective detection and determination of TATAAA oligonucleotide").

2. Patents pending

2.1 Pietrzyk-Le, A., **Bartołd, K.**, Noworyta, K., Lisowski, W., Kutner, W., D'Souza, F., Licandro, E., Sannicolò, F., Mussini, P. R., Appl., No. P.409329, 29 August 2014, published in BUP 14 March 2016, „Nowy sztuczny oligomer o sekwencji zasad nukleinowych ATATTT komplementarny do promotorowej sekwencji TATAAA, sztuczna nić promotora DNA zawierająca ten oligomer i jej zastosowanie do selektywnego wykrywania i oznaczania oligonukleotydu TATAAA" ("New artificial oligomer with the sequence of nucleobases ATATTT, complementary to the promoter sequence TATAAA, artificial DNA promoter string containing this oligomer and its application for selective detection and determination of TATAAA oligonucleotide"). Granted 9 December 2015.

2.2 **Bartołd, K.**, Pietrzyk-Le, A., Kutner, W., Appl. No. P.412848, 25 June 2015, published in BUP 14 March 2016, „Sposób wytwarzania polimeru z promotorową sekwencją TATAAA w sztucznej kasecie TATA oraz zastosowanie tego polimeru do rozpoznawania i/lub selektywnego oznaczania sześcionukleotydowej sekwencji DNA" ("Method for producing polymer with the promoter sequence TATAAA in artificial cassette TATA and application of this polymer for recognizing and/or selectively determining hexanucleotide sequence of DNA").

2.3 **Bartołd, K.**, Pietrzyk-Le, K., Golebiewska, K., Lisowski, W., Cauteruccio, S., Licandro, E., D'Souza, F., Kutner, W., Appl. No. P.422867, 18 Sep 2017, „Nowy bisbitiofenowy analog oktanukleotydu o sekwencji nukleotydów CGCCGCCG, sposób jego otrzymywania, czujnik elektrochemiczny zawierający ten analog, sposób wytworzenia tego czujnika i jego zastosowanie" ("A new bisbithiophene analog of octanucleotide of the CGCCGCCG sequence, a method of its preparation, electrochemical sensor containing this analog, a method of fabrication of this sensor and its application").

2.4 Garcia-Cruz, A., Pietrzyk-Le, A. **Bartołd, K.**, Pasierbiewicz, K., Majewska, M., Borowicz, Spólnik, G., Sharma, P. S., Cieplak, M., Nikiforow, K., Noworyta, K.,

Pięta, P., Danikiewicz, W., Lisowski, D'Souza, F., W., Kutner, Appl. No. P.423557, 28 Nov 2017, „Syntetyczny polimer nukleotydowy z warstwą rozpoznającą, jego wytwarzanie i zastosowanie do selektywnego oznaczania rakotwórczej heterocyklicznej aminy aromatycznej za pomocą czujnika chemicznego” ("Synthetic nucleotide polymer recognition film, its preparation and application for selective determination of cancerogenic heterocyclic aromatic amine using a chemical sensor").

Presentations at scientific conferences

1. **Bartold, K.**; Pietrzyk-Le, A.; Huynh, T-H.; Iskierko, Z.; Ciesielczuk, A., 6th International Workshop on Surface Modification for Chemical and Biochemical Sensing - SMCBS'2013 (Łochów, Polska), 08-12 Nov 2013, "A molecular imprinted polymer approach to detection of the TATAAA oligonucleotide".

2. **Bartold, K.**; Pietrzyk-Le, A.; Huynh, T-P.; Iskierko, Z.; Sosnowska, M., XXI Round Table on nucleosides, nucleotides and nucleic acids, (Poznań, Polska), 24-28 Aug 2014, "A Molecularly Imprinted Polymer Film For Recognition of a Six Nucleobase Sequence of The TATAAA".

3. **Pietrzyk-Le, A.**; Bartold, K.; Huynh, T-H.; Iskierko, Z.; Noworyta, K.; Sosnowska, M.; Kutner, W.; D'Souza, F.; Sannicolò, F.; Mussini, P. R.; Licandro, E., 65th Annual Meeting of the International Society of Electrochemistry, (Lozanna, Szwajcaria), 31 Aug - 5 Sep 2014, "Determination of the TATAAA oligonucleotide via hybridization of the electrosynthesized molecularly imprinted polymer (MIP) bearing complementary adenine and thymine nucleobases".

4. **Bartold, K.**; Pietrzyk-Le, A.; Kutner, W., 7th International Workshop on Surface Modification for Chemical and Biochemical Sensing - SMCBS'2015 (Pultusk, Polska), 06-10 Nov 2016, "Promoting bioanalytical concepts to genetics: The promise and the price".

5. **Bartold, K.**; Pietrzyk-Le, A.; Huynh, T-H.; Iskierko, Z.; Sosnowska, M.; Noworyta, K.; D'Souza, F.; Kutner, W., XIII Warszawskie Seminarium Doktorantów Chemików - ChemSession'16 (Warszawa, Polska), 10 June 2016, "Artificial ssDNA analogue and its hybridization resulting in the TATAAA promoter sequence: molecularly imprinted polymer (MIP) in genetics chemosensing".

6. **Bartold K.**, Pietrzyk-Le A., Kutner W., 60. Zjazd Naukowy Polskiego Towarzystwa Chemicznego (Wrocław, Polska), 17-21 Sep 2017, „Polimery wdrukowane molekularnie określoną sekwencją zasad nukleinowych w oznaczaniu wybranych oligonukelotydów".

List of abbreviations

A – adenine

AEG – 2-amino-ethyl-glycine

AFM – atomic force microscopy

AIBN – azobisisobutyronitrile

AgNC – silver nanocluster

AuNP – gold nanoparticle

ATRP – atom transfer radical polymerization

ATR – attenuated total reflection

BE – binding energy, eV

BOC – *tert*-butyloxocarbonyl (protecting group)

bpy – 2,2'-bipyridine

C – cytosine

C.E. – counter electrode

CI – capacitive impedimetry

CLRP – controlled/living radical polymerization

ctDNA – circulating tumor DNA

CV – cyclic voltammetry

D – drain (of transistor)

DFT – density functional theory

DMEM – Dulbecco's Modified Eagle's Medium

DMF – dimethylformamide

DMSO – dimethylsulfoxide

DPV – differential pulse voltammetry

DSC – differential scanning calorimetry

dsDNA – double-stranded DNA

EG-FET – extended-gate field-effect transistor

EIS – electrochemical impedance spectroscopy

EQCM – electrochemical quartz crystal microbalance

FIA – flow-injection analysis

G – gate (of transistor)

HEPES – 2-[4-(2-hydroxyethyl)piperazin-1-yl]ethanesulfonic acid

HPV – human papilloma virus

HSA – human serum albumin

ITC – isothermal titration calorimetry

ITO – indium-tin oxide

LNA – locked nucleic acid

LOD – limit of detection

LSAW – leaky surface acoustic wave

LSPR – localized surface plasmon resonance

mRNA – messenger RNA

MB – molecular beacon

miRNA – microRNA

MIL – minimum inactivating length

MIP – molecularly imprinted polymer

MO – morpholino oligomer

NAA – nucleic acid analogue

NP – nanoparticle

NIP – non-imprinted polymer

ODN – oligodeoxyribonucleotide

ON – oligonucleotide

PBS – phosphate buffered saline

PCR – polymerase-chain reaction

PDI – polydispersity index

PEG – poly(ethylene glycol)

PM – piezoelectric microgravimetry

PM-IRRAS – polarization-modulation infrared reflection-absorption spectroscopy

PNA – peptide nucleic acid

PSA – prostate specific antigen

QCM – quartz crystal microbalance

QCR – quartz crystal resonator

R.E. – reference electrode

RI – resolution of identity (density fitting)

RAFT – reversible addition-fragmentation chain transfer

ROMP – ring-opening metathesis polymerization

rpm – rotations per minute

RTESP – rotated tapping etched silicon probe

S – source (of transistor)

SNP – single-nucleotide polymorphism

SPR – surface plasmon resonance

SPW – surface plasma wave

ssDNA – single-stranded DNA

ssRNA – single-stranded RNA

T – thymine

Trt – trityl (triphenylmethyl)

$(TBA)ClO_4$ – tetrabutylammonium perchlorate

TBP – TATA binding 180-(amino acid) protein

TMS – tetramethylsilane

U – uracil

VDAT – 2-vinyl-4,6-diamino-1,3,5-triazine

XPS – X-ray photoelectron spectroscopy

List of symbols

A – electrode surface area, cm^2

A_{acoust} – acoustically active resonator area, cm^2

C – capacitance, F

C_{dl} – electrical double-layer capacity, $F\ m^{-2}$

c_M^X – concentration of injected macromolecule, M

$c_{Red/Ox}$ – bulk concentration of redox species, M

CPE – constant phase element, $F\ cm^{-2}\ s^{\forall-1}$

c_M – concentration of a macromolecular compound in proximity of the sensor surface, M

c_{L_0} – total ligand concentration, M

$D_{Red/Ox}$ – diffusion coefficient of a redox species, $cm^2\ s^{-1}$

d_{dl} – double-layer thickness, cm

E – potential, V

E_i – initial potential, V

E_f – final potential, V

E_{OCP} – open circuit potential, V

E_p – peak potential, V

ΔE_p – pulse amplitude, mV

E_{pa} – anodic peak potential, V

E_{pc} – cathodic peak potential, V

E_0 – voltage amplitude, mV

$E^{0'}$ – formal redox potential, V

$E(t)$ – alternating voltage, V

f – frequency, Hz

f_0 – fundamental frequency of a resonator, here 10 MHz

f_{eq} – equilibrium frequency of a resonator in the extreme of the function, Hz

f_{max} – maximum frequency reached after saturation of all MIP binding sites, Hz

Δf_{mass} – resonance frequency change corresponding to the change in mass of a resonator, Hz

Δf_{vis} – resonance frequency change corresponding to the change in viscosity and density of a liquid adjacent to the electrode surface of a resonator, Hz

ΔG – change of Gibbs free energy, kJ mol^{-1}

ΔH – change of enthalpy, kJ mol^{-1}

I_D – drain current, A

I_p – peak current, A

I_{pa} – anodic peak current, A

I_{pc} – cathodic peak current, A

I_0 – current amplitude, A

$I(t)$ – alternating current, A

j – imaginary number ($j^2 = -1$)

J – current density, A m^{-2}

J_0 – exchange current density, A m^{-2}

k' – free-space wave number

k_a – association rate constant, M^{-1} s^{-1}

k_d – dissociation rate constant, s^{-1}

K_i – association constant for binding sites of set i on a macromolecule, M^{-1}

k_{et} – electron transfer rate constant, s^{-1}

k_{exp} – experimental reaction rate constant, s^{-1}

K_s – complex stability constant, M^{-1}

k^2_{QCR} – electromechanical coupling factor of a quartz crystal resonator, $7,74 \times 10^{-3}$ A^2 s m^{-2}

L – ligand

[L] – molar concentration of a free ligand, M

[L]$_{eq}$ –equilibrium molar concentration of a free ligand, M

[L$_B$] – molar concentration of a bound ligand

[L$_B$]$_{eq}$ – equilibrium concentration of a bound ligand

[L$_{B,i}$] – molar concentration of a ligand bound to a macromolecule with binding sites of set i

M – macromolecular compound

[M] – molar concentration of a macromolecular compound, M

N_i – number of binding sites of set i of a macromolecule

n_s – refractive index

n – number of electrons transferred in the elementary redox process

Q – total heat, J

q – individual heat, J

R – reflectance angle (surface plasmon resonance signal), m°

R_{max} – maximum change of the SPR signal at saturation of all binding sites, m°

R_{eq} – equilibrium SPR signal in the extreme of function, m°

R_D – dynamic resistance, Ω

R_{ct} – charge transfer resistance, Ω

$R_{ct,i}$ – initial charge transfer resistance, i.e., before sample injection, Ω

$R_{ct,f}$ – final charge transfer resistance, i.e., after sample injection, Ω

R_{po} – resistance of a pore phase, Ω

R_s – solution resistance, Ω

R_{sa} – relative surface area

ΔS – entropy change, J mol^{-1} K^{-1}

ΔT – temperature difference between cells (ITC), K

t – time, s

t_p – pulse duration (DPV), ms

T – frequency-independent proportionality factor

T_m – melting temperature, K

V – reaction volume, mL

V_G – gate voltage, V

V_D – drain voltage, V

$W_{1/2}$ – peak width at half height

W – Warburg impedance, Ω

x_{ef} – hybridization efficiency

Z – impedance, Ω

Z_{im} – imaginary component of impedance, Ω

Z_{real} – real component of impedance, Ω

Z_{CPE} – impedance of constant phase element, Ω

α_a - charge transfer coefficient of an anodic process

β – propagation constant

ε – electric permittivity

ε_m – metal electric permittivity

ε_0 – electric permittivity of free space, F m^{-1}

η_L – dynamic viscosity, cP

μ_q – shear modulus of quartz, 2.947×10^{11} g s^{-2} cm^{-1}

ρ_q – quartz density, 2.648 g cm^{-3}

ρ_L – liquid density, g cm^{-3}

v – potential scan rate, mV s^{-1}

ϕ – exponential factor

φ – phase angle, degree

σ – real number

ω – angular frequency, rad s^{-1}

Abstract

The present PhD thesis describes devising, fabricating, and characterizing of chemical sensors for selective determination of short AT- or GC-rich oligonucleotides. In these chemosensors, a specially developed new class of nucleobase-containing polymers served as probes, providing sensors recognition capability. For preparation of these polymers, a 'molecular imprinting in polymer strategy' with sequence-programmable templates was used. First, dedicated stable electroactive bis(2,2'-bithien-5-yl) functional monomers, each bearing nucleobase (A - adenine, T - thymine, C - cytosine, or G - guanine) functionality, were allowed aligning, in the right order, around a selected template, thus forming a pre-polymerization complex via Watson-Crick nucleobase pairing. Stability of the pre-polymerization complexes of AT-rich template with T and A functional monomers as well as GC-rich template with C and G functional monomers were estimated with the density functional theory (DFT) at the B3LYP level and verified with isothermal titration calorimetry (ITC) experiments. Then, these complexes were potentiodynamically electropolymerized yielding films of the molecularly imprinted polymers (MIPs) deposited on surfaces of conducting transducers. After the polymerization, templates were extracted from MIPs. That way, molecular cavities were vacated, thus exposing the ordered nucleobases on the 2,2'-bithien-5-yl polymeric backbones of the probes designed to hybridize the complementary AT- or GC-rich oligonucleotides. Therefore, the extracted MIP films selectively recognized oligonucleotides with respect to one or two nucleobase mismatches. The templates complete extraction from the MIP film was confirmed by the measurements of X-ray photoelectron spectroscopy (XPS), differential pulse voltammetry (DPV), electrochemical impedance spectroscopy (EIS), and polarization-modulation infrared reflection absorption spectroscopy (PM-IRRAS). Morphology of deposited MIP films was unraveled and characterized with AFM. The MIP films were then successfully applied for selective determination of short oligonucleotides under both flow-injection analysis (FIA) and stagnant-solution conditions using piezoelectric microgravimetry (PM), capacitive impedimetry (CI), or surface plasmon resonance (SPR) spectroscopy. Based on these measurements, analytical parameters of the chemosensors, such as sensitivity, selectivity, and the limit of detection (LOD) were estimated. Kinetic analysis of the analytes interaction with the MIPs provided the values of the stability constant as high as that characteristic for longer-chain DNA-PNA duplexes. Moreover, hybridization efficiency of the GC probe as well as its discriminative capability in Dulbecco's Modified Eagle's Medium was determined.

Abstract (PL)

Niniejsza rozprawa doktorska przedstawia badania przeprowadzone w celu skonstruowania, wytworzenia i scharakteryzowania czujników chemicznych do selektywnego oznaczania krótkich oligonukleotydów bogatych w adeninę (A) i tyminę (T) lub guaninę (G) i cytozynę (C). W czujnikach tych rolę sond pełniły specjalnie opracowane i zsyntetyzowane polimery podstawione zasadami nukleinowymi, które rozpoznawały i wiązały określone anality nukleotydowe. Do wytworzenia tych sond zastosowano technikę wdrukowania molekularnego z szablonami „programującymi" sekwencję zasad nukleinowych syntetyzowanych polimerów. Ustawiały one, w określonej kolejności, monomery funkcyjne, którymi były pochodne bis(2,2'-bitien-5-ylowe) podstawione jedną z czterech zasad nukleinowych. Oddziaływania wodorowe Watsona-Cricka pomiędzy cząsteczkami szablonów i określonych monomerów prowadziły do powstania kompleksów pre-polimeryzacyjnych w roztworach. Trwałość tych kompleksów oszacowano za pomocą modelowania kwantowo-chemicznego stosując metodę funkcjonału gęstości (DFT) w przybliżeniu B3LYP i eksperymentalnie potwierdzono za pomocą izotermicznego miareczkowania kalorymetrycznego (ITC). Następnie kompleksy te spolimeryzowano elektrochemicznie w warunkach potencjodynamicznych w wyniku czego otrzymano polimery molekularnie wdrukowanie (MIP) osadzone w postaci cienkich warstw na powierzchni przewodzących przetworników. Następnie z polimerów tych usunięto szablony. W ten sposób, w opróżnionych z cząsteczek szablonu wnękach molekularnych odsłonięte zostały zasady nukleinowe bis(2,2'-bisbitien-5-ylowego) łańcucha polimerowego, hybrydyzujące z komplementarnymi zasadami nukleinowymi analitów. Usunięcie szablonów z MIP-ów potwierdzono za pomocą spektroskopii fotoelektronów w zakresie promieniowania X (XPS), woltamperometrii pulsowej różnicowej (DPV), elektrochemicznej spektroskopii impedancyjnej (EIS) lub spektroskopii odbiciowo-absorpcyjnej o modulowanej polaryzacji w podczerwieni (PM-IRRAS). Morfologię osadzonych warstw zbadano za pomocą mikroskopii sił atomowych (AFM). Następnie warstwy MIPów zastosowano do selektywnego oznaczania krótkich oligonukleotydów zarówno w warunkach analizy przepływowo-wstrzykowej (FIA) jak i stacjonarnych za pomocą mikrograwimetrii piezoelektrycznej (PM), impedimetrii pojemnościowej (CI) i spektroskopii plazmonów powierzchniowych (SPR). Na podstawie tych pomiarów wyznaczono parametry analityczne chemoczujników, takie jak czułość, selektywność, liniowy dynamiczny zakres stężeniowy i granicę wykrywalności (LOD). Z pomiarów kinetycznych wyznaczono stałe trwałości kompleksów MIPów z analitami. Wartości tych stałych odpowiadały wartościom charakterystycznym dla par DNA-PNA o dłuższych łańcuchach. Ponadto wyznaczono wydajność hybrydyzacji sondy GC oraz określono jej zdolność rozpoznawania analitu w pożywce Eagle'a w modyfikacji Dulbecco.

Research goal

Several procedures have already been elaborated for qualitative and quantitative DNA determination. Among others, electrochemical methods have a great potential because of low cost, simplicity, and ease of miniaturization. However, the DNA sensor technology still lacks of devises for the point-of-care applications. Toward this goal, highly sensitive, selective, and rapid DNA determination with simplified protocols and, particularly, with as limited as possible sample preparation, is of paramount importance.

Therefore, the aim of the presented research is to develop fast, cost-effective, and label-free systems for DNA sensing based on new electropolymerized DNA analogue probes. For straightforward and rapid DNA quantification, these recognizing probes are herein integrated with different transducers to perform as chemical sensors. Due to recognition at a molecular level, molecular imprinting in polymers provides a powerful tool to unravel the structure-biofunctionality correlation and can be used to synthesize DNA analogues, and thus chemosensors of the next generation. The application of these devises aims at identification of genetically relevant GC- and AT-rich oligonucleotides including single nucleotide polymorphism and trinucleotide repeat expansion diseases.

Contents

Chapter 1

Literature review

This chapter contains characteristics of non-naturally occurring nucleic acid analogues and mimics, and describes their use in detection of single nucleotide polymorphisms (SNPs). Moreover, it is dedicated to oligonucleotide chemosensing including molecularly imprinted polymers (MIPs) and their hybrids with DNA aptamers.

1.1 Nucleic acid analogues and mimics

This section provides information on synthetic nucleic acid analogues (NAAs) and mimics, which are modifications of naturally occurring DNA or RNA that possess their functionality.

1.1.1 Peptide nucleic acids (PNAs)

Peptide nucleic acids, PNAs, (Scheme 1.1-1d) are DNA (Scheme 1.1-1a) analogues developed by Nielsen et al. in 1980s.[1] Since then, PNAs have found application in different fields of science ranging from pure chemistry, over molecular biology, drug discovery and genetic diagnosis, nanotechnology, and molecular recognition of nucleic acids.[2] Toward the latter, PNAs of a wide variety of chemical properties have been synthesized and characterized.

The original PNAs are noncyclic pseudo-peptide nucleic acid structural mimics with the *N* atom terminus at the left and the *C* atom terminus at the right position. They have an achiral polyamide backbone built out of *N*-(2-aminoethyl)glycine units. The purine or pyrimidine nucleobases are attached to each unit with a methylene carbonyl linker. PNA subunits are made of the standard purine (A - adenine and G - guanine) and pyrimidine (C - cytosine and T - thymine) nucleobases. PNAs have inherently flexible structure, mainly constrained by the two amide groups. These analogues bind to complementary single-stranded RNA (ssRNA) or single-stranded DNA (ssDNA) in a parallel or antiparallel orientation obeying the Watson-Crick nucleobase pairing rule.[3] Because the PNA oligomers are not charged, they are more stable than natural oligonucleotide homoduplexes even at a relatively high temperature. They reveal excellent hybridization properties and, hence, stability of the PNA-(nucleic acid) duplexes[3] at a low ionic strength,[4] at which the DNA or RNA secondary structure is

1

maintained. Because of these advantageous properties, isolation and detection of nucleic acids in genetic diagnostics is feasible.[1] Moreover, these DNA analogues are highly resistant to proteases and nucleases as well as other biological degradative agents.[5-7]

PNAs, as uncharged nucleic acids analogues (NAAs), are much less water soluble than DNAs. They have sequence-dependent tendency to aggregate. That is, the PNA water solubility depends upon the length of its molecule chain and the purine-to-pyrimidine molar ratio.[8] Moreover, the PNA has to be pre-organized in order to assume conformation suitable for complexation with nucleobase bearing functional monomers.[9-10] Furthermore, PNA sequence programmability can be utilized for fabrication of a new generation electropolymerized DNA analogue and its direct immobilization on the transducer surface.[9-10]

Stability of the DNA duplexes in aqueous solutions, in terms of the Gibbs free energy change accompanying hybridization, is primarily due to nucleobase-pair hydrophobic π-π stacking interactions rather than to nucleobase-pair hydrogen bonding. In aprotic non-polar solvent solutions, however, the hydrogen bonds are stronger while the stacking interactions are weaker, thus making PNA duplexes more stable.

PNAs reveal several properties of the antisense reagent. Because they strongly bind to complementary messenger RNA (mRNA) and are highly stable, they can effectively inhibit translation of the target mRNA. Their advantage over other antisense agents consists in their stability inside the cells, which reaches at least 48 h. This relatively high stability makes them promising as candidates for the antisense and antigen applications.[11-12]

Furthermore, PNAs can form stable triplex structures or strand-invaded, or strand-displacement complexes with DNAs. These complexes constrain a structural hindrance for transcriptional processes by blocking RNA polymerase. The PNA targeted against the DNA promoter region can form a stable DNA-PNA duplex that blocks the access of the corresponding polymerase to DNA.

In anticancer therapy, PNA offers a promising approach for silencing oncogenic microRNAs (miRNAs). This miRNA nucleic fragments are frequency overexpressed in human cancer, e.g., miR-210 acts to orchestrate the adaptation of tumor cells.[13]

1.1.2 Locked nucleic acids (LNAs)

Locked nucleic acids (LNAs) are conformationally restricted ON analogs first described by Singh et al. in 1998.[14] These nucleic acids are RNA structural mimics fitting into an A-type duplex geometry.[3] In their structure, these bicyclic nucleic acids have ribonucleoside moieties linked between the 2'-oxygen and 4'-carbon atoms with methylene units (Scheme 1.1-1b).

Because LNAs display unprecedented hybridization affinity toward complementary ssDNA and ssRNA, they are versatile tools for specific high-affinity recognition of these nucleic acids. The LNA-DNA and LNA-RNA duplexes are the two possible LNA hybrids. These hybrids characteristics is similar to that of native nucleic acid duplexes in Watson-Crick base pairing, nucleobases in the antiorientation, nucleobase stacking, and a right-handed helical orientation.[3]

The high-affinity LNA can be designed as LNA-DNA and LNA-RNA chimeras or a fully modified LNA. Because of strong base pairing of LNA, which leads to LNA-LNA duplexing, these analogues should be deprived of extensive self-complementary segments.

LNAs are one of the most useful modified oligonucleotide backbones because stability of their duplexes with nucleic acids can be modified by incorporation of a single-stranded LNA. Therefore, LNA-incorporated nucleic acid probes and primers were widely designed. This duplex stabilization is due to either its pre-organization or improved π-π stacking.[15] Moreover, ONs bearing LNAs duplexes with complementary ssDNA and ssRNA are not only exceptionally thermally stable but also highly mismatch discriminative. For the single-nucleotide polymorphism (SNP) genotyping studies, short LNA probes can be used because of their high binding affinity of LNA oligomers.

High affinity and efficient mismatch discrimination as well as multiplexing make LNAs useful for diagnostics. Many diseases are associated with SNP in the genetic code. LNAs found application in efficient and simple SNP assays, which effectively recognize the mismatch.[17-18] These assays employ probes complementary to the wild-type or mutated genomic nucleic acid sequences and are subjected to PCR amplification.
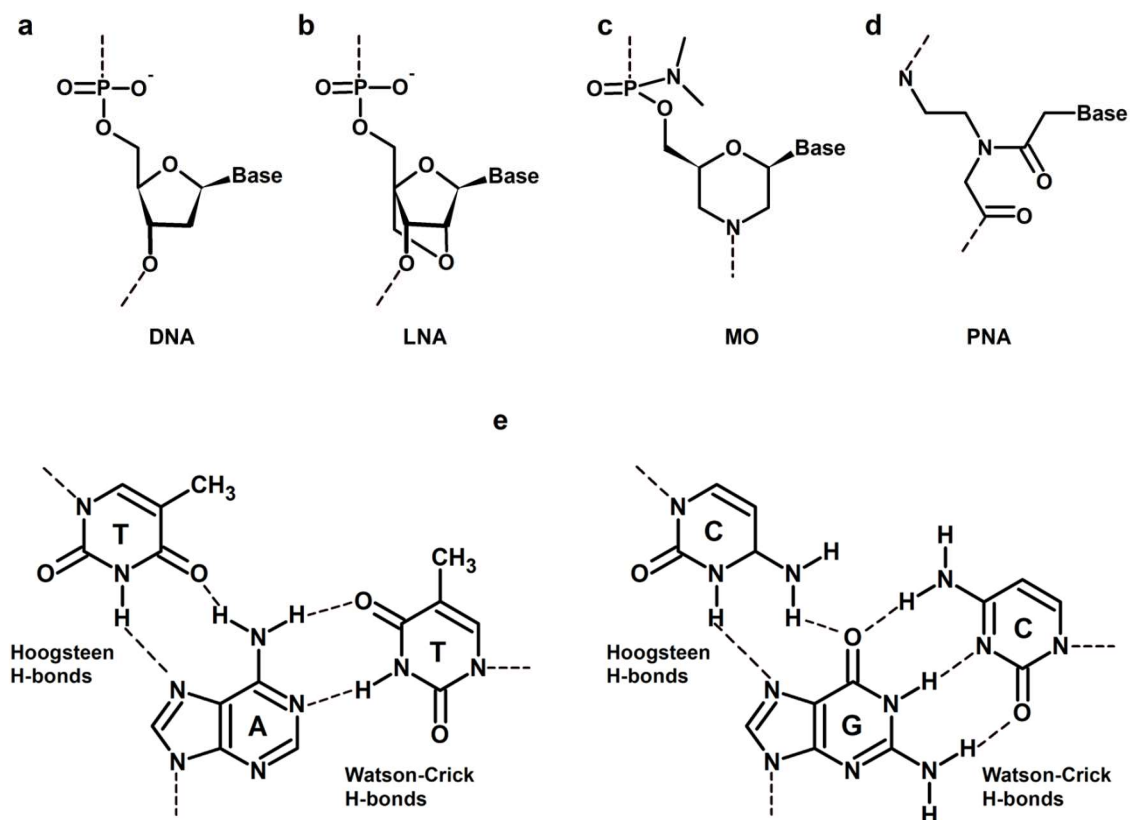
Scheme 1.1-1. Structural formulas of (a) deoxyribonucleic acid (DNA), (b) locked nucleic acid (LNA), (c) morpholino oligonucleotide (MO), and (d) peptide nucleic acid (PNA). (e) Hoogsteen nucleobase pairing occurring in triplex formation.[16]

Because of their chemical and biophysical properties, LNAs are promising as antisense agents. LNAs pronounced therapeutic effects result from their high stability in serum, low in vivo toxicity, and high uptake by mammalian cells.[17] Various modes of action of the LNAs in antisense studies rely on activating RNase (which degrades mRNA), steric blocking of the template RNA, or inhibiting of pre-mRNA splicing.

1.1.3 Morpholino oligonucleotides (MOs)

Morpholino oligonucleotides (MOs), another group of DNA analogues, were devised by Stirchak and Summertone in 1985.[19] MOs are antisense oligomers, which block access of other molecules to nucleobase pairing RNAs of small (~25 nucleobase) specific sequences. They are active in a cell-free protein synthesis and cultured animal cells. MOs have DNA nucleobases attached to a backbone of methylenemorpholine rings linked through phosphorodiamidate groups (Scheme 1.1-1c). They were devised to eliminate cost problems associated with preparation of other DNA analogues. Synthesis

4

of MOs is cost-effective for the reason that it starts with much less expensive ribonucleosides, to which an amine group is introduced via a relatively simple ribose-to-morpholino transformation. In case of weak nucleobases π-π stacking in aqueous solutions, water solubility of these stacks is low because of difficulty in inserting the hydrophobic faces of the nucleobases into aqueous environment. The nonionic phosphorodiamidate-linked MOs are highly soluble in water, even more than DNA.[20] Moreover, the MO backbone is resistant to strong bases. However, it degrades in strong acids, e.g., trifluoroacetic acid. MOs are distributed throughout the cytosol and the nucleus. Therefore, they have access to their target RNAs during their long residence in cytosol.

To achieve high selectivity, MOs should have a minimum inactivating length (MIL) sufficiently long to avoid attacking on non-target RNAs. The MIL factor makes MOs capable of inhibiting the target at concentrations reached in the cytosol-nuclear part of cells. There are two crucial requirements of the MOs design that ensure their high efficiency. First, the MIL should be sufficiently long, thus not inactivating non-targeted species. Second, the length of the oligomer chain should be sufficiently longer than its MIL.[21]

MOs binding affinity for genetically important nucleic acids of complementary sequences is rather insensitive to the solution ionic strength. Duplexes of these analogues with ssRNA are more stable than the corresponding DNA-RNA duplexes.[3]

In antisense therapy, MOs are applied for correcting splicing errors of mRNAs in cultured cells and for extracorporal treating of cells from thalassemic patients.[22] The most demanding application of MOs is in developmental biology. This field was revolutionized by MOs analogues because of providing unique reliable tools for blocking the expression of selected genes through embryogenesis in model organisms.[23]

1.1.4 Synthetic nucleobase-containing polymers

A vast recognizing potential of nucleobases inevitably led to their harness to polymer chemistry and materials science. So far, different nucleobase-containing polymers have been designed and synthesized according to different polymerization mechanisms.

An early synthetic research on the DNA or RNA mimicking focused on the attachment of a nucleobase to natural polymers, such as cellulose.[24-25] Radical polymerization of monomers bearing a nucleobase moiety with the *N*-vinyl derivatives

of purines and pyrimidines as early representatives[26-27] allowed preparing synthetic NAAs. Subsequently, significant advances were made in the development of various synthesis skill sets, especially the controlled living radical polymerization (CLRP).[26-27] More recent developments involve controlled polymerization of these monomers as well the self-assembly and template polymerization.

An early 21st century concept of templated polymerization of nucleobase containing monomers that resulted in a preformed oligomer by formation of hydrogen bonds appeared elegant in controlling the sequence of monomer units along a polymer chain.[9-10] First, the polymerization of silyl protected 5'-acryloylnucleosides resulted in corresponding nucleobase containing homopolymers.[28] Next, those homopolymers were used as templates for polymerization of complementary nucleobase monomers. The uracil-based homopolymer suited that purpose better than its A counterpart because of self-association of the latter.[28] Only in the presence of the former homopolymer, the 5'-acryloyladenosine monomer polymerized preferentially along the complementary template even in the presence of the non-complementary 5'-acryloyluridine interference. The formation of the nucleobase containing homopolymer templates, and then the template-directed polymerization of complementary monomers, was performed according to a typical free-radical mechanism.[28]

One of the earliest examples of CLRP studies of monomers containing nucleobases included the atom transfer radical polymerization (ATRP) of protected 5'-(meth)acryloylnucleosides.[28] More conventional monomers, e.g., methyl methacrylate and styrene, were polymerized with the use of nucleobase functionalized ATRP initiators. These initiators provided a high polymerization control, thus allowing for generating well-defined polynucleoside macromolecules. Later, ATRP was utilized to synthesize well-defined poly(ethylene glycol) (PEG) nucleobases, vis. (PEG)-polyA and (PEG)-polyT, containing block co-polymers from PEG-based macroinitiators.[29] The T and A monomers, a catalyst, a ligand, and PEG-based macroinitiators were mixed together, and then subjected to the ATRP procedure (Scheme 1.1-2). Then, the reaction was quenched with 1-phenyl-1-(trimethylsiloxy)ethylene. To demonstrate properties of side-chain nucleobases, two complementary block copolymers were interacted with each other, thus resulting in assembled macromolecular compounds of increased water solubility.

Similarly, poly[1-(4-vinylbenzyl)thymine] was synthesized through ATRP. Its recognition abilities were demonstrated by adding pre-synthesized

6

9-hexadecyladenine.[30] Because of the hydrogen bonds formed between T and A substituents, biocomplementary supramolecular complexes were formed in the DMSO solution.[31] In the bulk state, these complexes self-assembled into well-ordered lamellar structures. This example of nucleobase-containing molecules belongs to the so-called "plug and play" polymers. Their efficiency of recognition of the added guest molecules can readily be adjusted by balancing between intra- and intermolecular interactions. The choice of the side-chain functionalities of different nucleobase derivatives incorporated in the polymer is crucial in recognition and uptake of added complementary molecules.[32] Efficient recognition, e.g., stoichiometric alignment of molecules along templates, is essential for templating applications of nucleobase containing polymers. For that, intramolecular interactions between polymer strands must be sufficiently weak for unwinding of polymer chains to associate added guest molecules.

As popular as ATRP, the reversible addition-fragmentation chain transfer (RAFT) method was used to synthesize methacryloyl monomers with A and T substituents to yield homopolymers and copolymers with a high control over their molecular mass (Scheme 1.1-3).[30] The architecture and morphology of the polymer was affected by the solvent nature. For instance, chloroform promoted formation of hydrogen bonds between A and T monomers with the preference of alternating copolymers while DMF suppressed formation of these bonds, thus resulting in statistically distributed copolymers.

Scheme 1.1-2. Synthesis of the (PEG)-polynucleobase copolymer by ATRP and simplified structures of assembled copolymers.[29,33] bpy - 2,2'-bipyridine, DMSO - dimethylsulfoxide, TMS - tetramethylsilane.

Similarly, more nucleobase-containing materials were prepared via RAFT dispersion polymerization, and then their self-assembly behavior was investigated.[34] These studies strongly demonstrated that nucleobase interactions played a fundamental role in controlling the polymer shape and size. A selective macroscopic system was self-assembled by involving polymer gels modified with either complementary DNA oligonucleotides or nucleobase-containing polymers.[35] These gels were prepared via conventional radical terpolymerization of acrylamide or styrene used as main-chain units as well as *N,N*-methylenebisacrylamide or *p*-divinylbenzene as cross-linking

8

units. The ON-modified hydrogels can macroscopically distinguish different complementary ON strands. Although conventional radical polymerization provides a simple method for polymer synthesis, it has some disadvantages consisting in an insufficient control of the polymer length, polydispersity, and macromolecular structure.
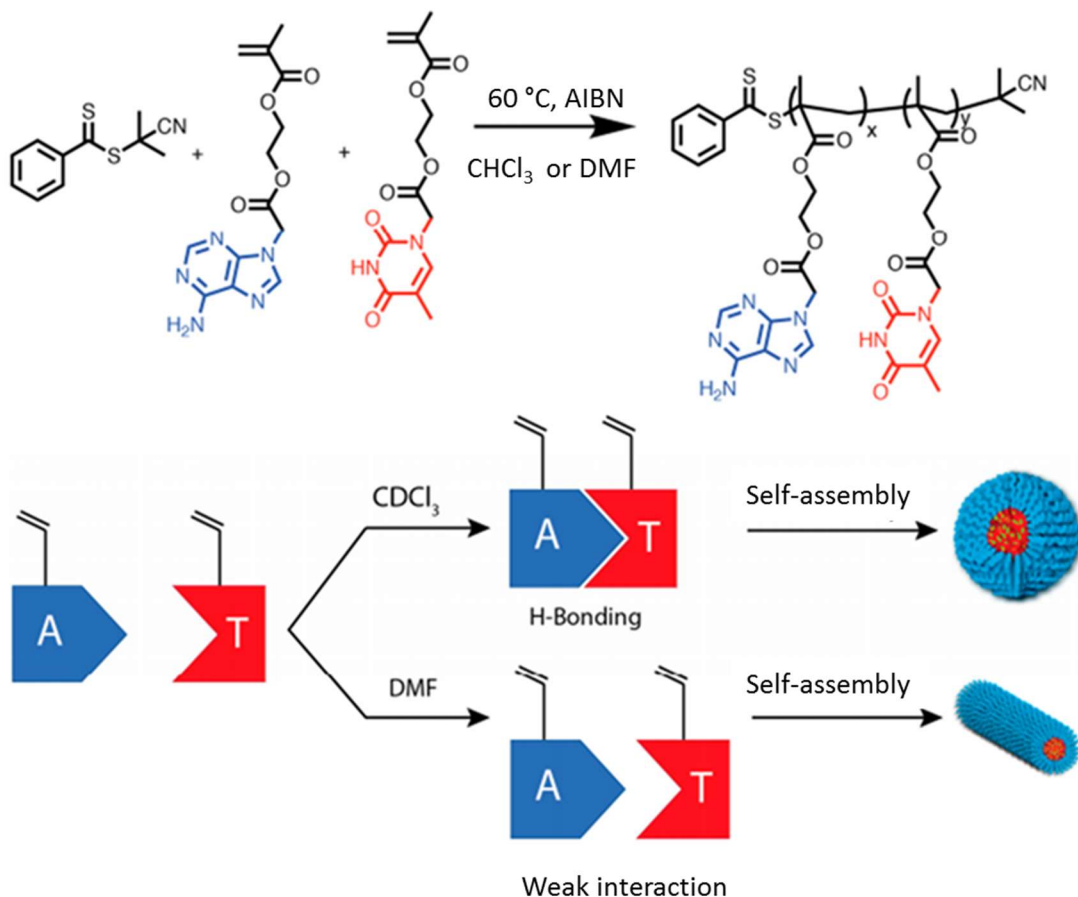
Scheme 1.1-3. The adenine and thymine block copolymers synthesis and self-assembly using RAFT.[30,33] AIBN – azobisisobutyronitrile, DMF – dimethylformamide, A – adenine, T – thymine.

Another method of preparation of linear polymers, branched polymers, dendrimers, and polymer networks involves polymerization based on the concept of "click chemistry".[36] Combination of this concept with nucleobase-containing polymers is promising. An interesting example of the "click chemistry" reaction was the synthesis of sequence-controlled polymers, which were single-nucleobase homopolymers of strictly defined repeating nucleobase sequences.[37] Here, a thiol-protected acrylamide monomer was coupled to a functionalized thiol-allylamine monomer in a thiol-Michael addition (Scheme 1.1-4). Next, the thiol group was deprotected and polymerized with allylamine groups by initiation of the thiol-ene reaction. This "click" by "click"

reaction demonstrated possibility of synthesis of sequence-controlled oligomers or polymers without using any solid support.

Ring-opening metathesis polymerization (ROMP) has found application in preparation of nucleobase-containing polymers.[38-39]

The ROMP strategy was used for constructing T-containing block copolymers with a narrow molecular mass distribution.[40] After aligning the A-containing monomers along the T template via hydrogen bonding, these monomers were polymerized, thus resulting in a templated conjugated polymer (Scheme 1.1-5). The length of the daughter strand was equivalent to that of the template strand. That is, the daughter strand copied the length and distribution of information of the template strand.

One of the ROMP examples involved preparation of polymeric nucleic acids with single-stranded PNAs incorporated as polymer brushes.[41] This combination of PNAs and ROMP provided an efficient strategy for preparation of amphiphilic brush copolymers by grafting through polymerization of a relatively large side chain. This chain is promising for various useful applications including DNA purification, gene delivery, and programmable materials preparation.

One of the applications of the nucleobase-containing materials involves hydrogels serving as matrices for cell cultures. This application found a widespread use in tissue engineering, biomolecule delivery, and regenerative medicine.[42] Noticeably, nucleobase-interaction based hydrogels were used as scaffolds for growth factor delivery and cell encapsulation, which evidenced their high biocompatibility and potential use in further biomedical applications.[43]

Another application of NAAs includes DNA delivery. For this application, these analogues should reveal high DNA uptake, fast DNA release, and the presence of nuclear targeting.[44] For DNA delivery, a system of triblock copolymer with clickable nucleic acids was synthesized, and then translated into polymer nanoparticles (NPs).[45] These nucleobase-containing NPs efficiently encapsulate complementary DNA, which is promising for their potential application in specific gene silencing.

Moreover, complementary nucleobase-containing polymers can be used in preparation of materials that exhibit advantageous mechanical properties and self-healing behavior. For instance, the materials of multi-uracil functionalized polyhedral oligomeric silsequioxane and the A end-capped three-arm polycaprolactone oligomer are highly capable of cross-linking via complementary interactions and self-healing autonomously at room temperature without external stimulations.[46]
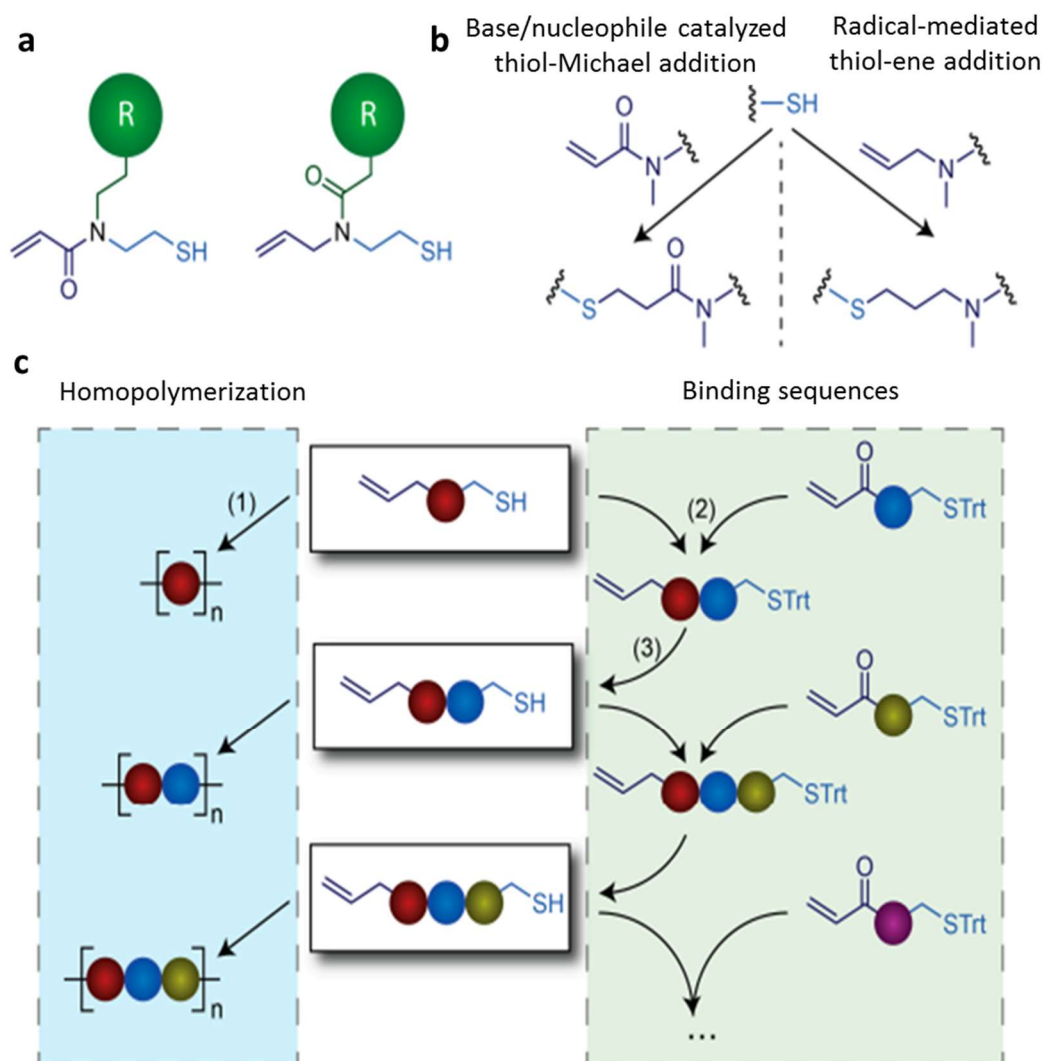
Scheme 1.1-4. (a) The general structure of monomers ready for "click" polymerization. (b) Two types of thiol "click" reactions. (c) The strategy for preparation of sequence-controlled functional oligomers and polymers.[37] Trt – trityl, i.e., triphenylmethyl.

Another example involves self-healing pH-sensitive biodegradable C- and G-modified hyaluronic acid hydrogels.[47] These cross-linked under physiological conditions hydrogels were prepared by engaging hydrogen bonds formed between C and G moieties with themselves or with each other. Mechanical properties of hydrogels prepared using C-G hydrogen bonds were more advantageous than those utilizing C-C or G-G hydrogen bonds. Those C-G bound hydrogels are promising for constructing polypeptide and protein drug delivery systems, soft tissue processing, preparing cell scaffold materials, and implementing in regenerative medicine.

Nucleobase-templated polymerization
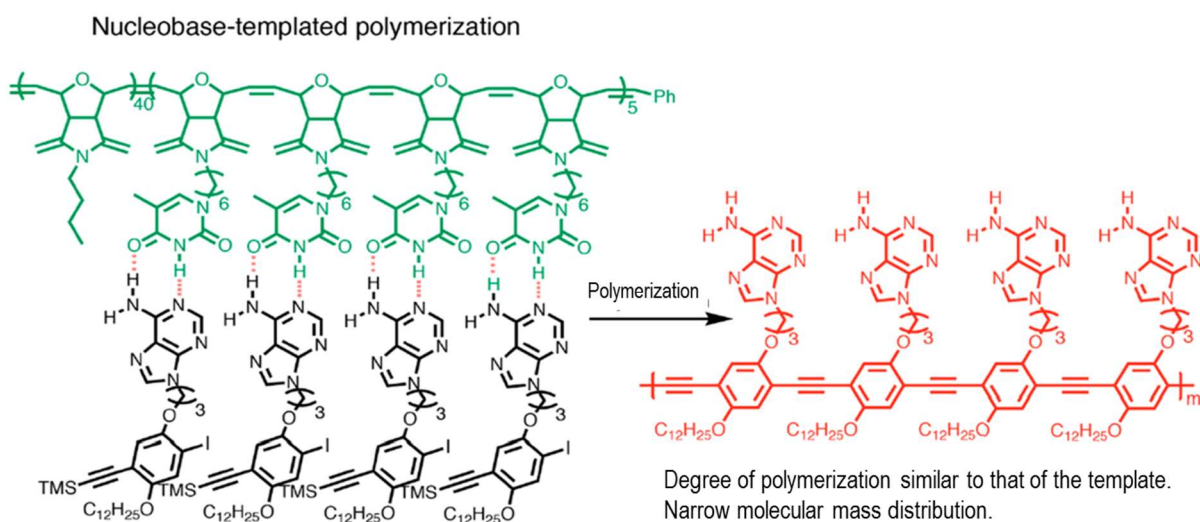
Scheme 1.1-5. Thymine templated polymerization of adenine-containing monomers.[40]

1.2 Oligonucleotide chemosensors

This section provides basic information on oligonucleotides with adenine-thymine or guanine-cytosine rich sequences and methods of their determination. Moreover, there is a brief description of chemosensors for SNP and oligonucleotide chemosensing based on molecularly imprinted polymers.

1.2.1 Oligonucleotides sensing with adenine-thymine (A-T) and guanine-cytosine (G-C) repeats

Repeated AT-rich sequences are commonly encountered in the DNA sites for transcription initiation in eukaryotic genes. These motifs are binding places for the regulatory factors. The TATAAA hexanucleotide is a part of a special DNA region referred to as the core promoter (Scheme 1.2-1). This region, with the transcription start site and immediately flanking nucleotide sequences,[48] is critical for proper regulation of the gene-selective transcription in eukaryotes.
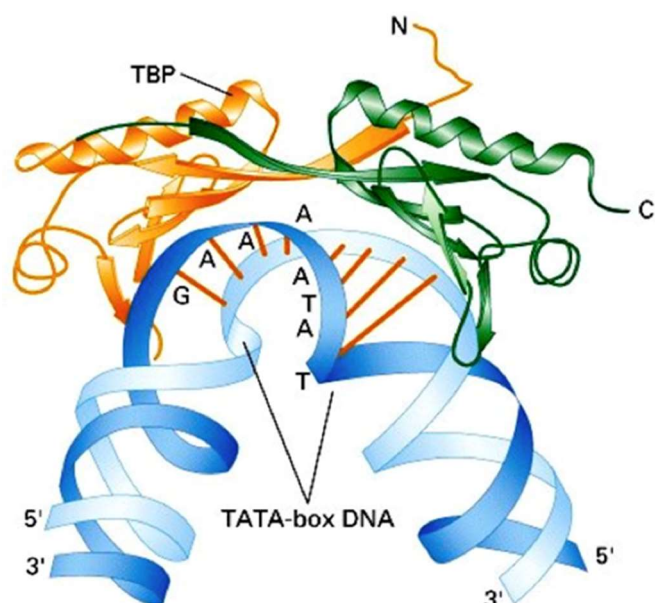
Scheme 1.2-1. The TATA box as a binding site for the TATA binding protein, TBP.[49]

Nearly 24% of human genes contain the TATA-like moiety.[48,50] One part of the basal transcription factor is the TATA binding 180-(amino acid) protein (TBP),[51] which binds to the TATA box during transcription (Scheme 1.2-1). This protein forms a complex with its carboxyl-terminal domain or core part with high affinity, the complex stability constant being, $K_s = 10^9$ M^{-1}.[52-53] Protein binding induces a conformational change in DNA manifested by its chain partial unwinding and bending by 80 to 90°.[54-55] Only the minor DNA groove is engaged in interactions with TBP, which includes hydrogen bonds as well as the van der Waals and stacking interactions. The TBP serves as a link for assembling basal pre-initiation complex and, together with the TBP-associated factors, forms a multi-protein complex. The RNA polymerase recognizes this complex, thus initiating the transcription.[52-53,56]

Genetically relevant GC-rich ODNs may be involved in many important biological processes including genome recombination, cancer cell immortality, and regulation of gene expression.[57] In mammalian genome, 50% of all genes are controlled by the GC-rich import regulatory domains comprising promoters, enhancers, and control elements. Particularly, most housekeeping genes, tumor-suppressor genes, and tissue-specific genes contain high amounts of GC sequences in their promoter region.[58] Moreover, GC-rich segments of DNA can be found in the bloodstream as a cell-free DNA. Their GC-enrichment is caused by some diseases. Therefore, they serve as indicators of the

13

physiological state of the organism as well as cancer biomarkers. Furthermore, not only mammals have DNA of GC-rich segments. Some pathogens, e.g., *Pseudomonas aeruginosa*, have high specific GC content in their genome. Therefore, our present strategy was also oriented towards selective detection of these pathogens.[9]

So far, GC-rich segments of ssDNA were mainly determined by fluorescence spectroscopic and electrochemical techniques. In the post-PCR detection, a branch-migration based probe of nucleic acid (labeled with a dye and a quencher) was used.[59] After hybridization with an ssDNA analyte, an average fluorescence signal increased as a result of different distance between the dye and the quencher.

Another sensing approach includes silver nanoclusters (AgNCs) used as probes for highly selective detection of $(CGG)_x$.[60] AgNC fluorophores were in situ grown on $(CGG)_x$. Therefore, no complicated synthesis procedure was needed for probe preparation before the detection. However, the limit of detection (LOD) was merely ~40 nM.

For electrochemical detection, a bifunctional probe bearing both a recognition and electroactive moiety was synthesized, and then used.[61] Determination of CGG repeats with this probe depended upon hybridization of the CGG analyte strand with the immobilized on the electrode complementary probe strand, performed at a high (65 °C) and low (3 to 5 °C) temperature. However, the biosensor response was generated not until after 30-min exposure of the electrode coated with the immobilized ssDNA hybridized analyte to the bifunctional probe, which first recognized CGG trinucleotide repeats, and then was oxidized.

Another electrochemical sensor was fabricated by immobilizing the nucleic acid recognition molecule of a naphthyridine carbamate dimer on the gold electrode surface.[62] After sensor immersing in the trinucleotide repeat solution for 2 h, electrochemical impedance spectroscopy (EIS) measurement was performed using the $Fe(CN)_6^{4-}/Fe(CN)_6^{3-}$ couple as the redox marker. That way, XGG repeats (X = C, T) were selectively detected based on the differences in their charge transfer resistance (ΔR_{ct}). The dependence of ΔR_{ct} on log(concentration of CGG repeats) for the sensor was linear in the range of 1 nM to 1 μM.

1.2.2 DNA analogues for detection of single nucleotide polymorphisms (SNPs)

Single nucleotide variations in DNA and RNA sequences can cause genetic and infectious diseases. Moreover, they are important for drug-resistant detection of

pathogens. Notably, there is an increasing interest in personalized diagnostics, particularly in the underlying genetic causes of diseases. Genetically relevant oligonucleotides may be involved in many important biological processes including genome recombination, cancer cell immortality, and regulation of gene expression.[57] This interest invokes higher demand for detecting and identifying the RNA and DNA specific sequences. Distribution of DNA sequences considerably varies between individuals. Most of the variations in the human genome results from SNPs.[63] Each SNP represents a difference in a single DNA building block, i.e., a nucleotide. For example, an SNP may replace the C nucleotide with the T nucleotide in a certain region of DNA. SNPs naturally occur throughout a person's DNA. Some of these genetic differences are very important in the study of human health. Therefore, understanding the SNP is essential for healthcare monitoring. SNPs are potent molecular genetic markers and valuable indicators for biomedical research, drug development, clinical diagnosis, disease therapy, evolutionary studies, and forensic science.[64] Therefore, there is a need of reliable tools for simple, fast, inexpensive, and sensitive monitoring of SNP genetic variations.[65]

Generally, SNP diagnostics simultaneously develops in two main directions. These include high-throughput methods and portable easy-to-handle assays.[65-66] High-throughput sequencing and PCR are current methods of choice for research on cancer and infectious diseases in developed countries.[65] However, more readily available techniques for rapid point-of-care diagnosis in the absence of sequencing and PCR are necessary. Moreover, all high-throughput techniques developed to date apply enzymes in order to achieve the required high sensitivity and selectivity of detection.[67] Enzymes increase the risk of errors during the determination and affect stoichiometry of the targeted mutation with respect to a wild-type analogue. Thus, all methods of nucleic acids detection and quantification would benefit from alternative enzyme-free strategies.[67] With regard to these objectives, a solid support or solution system using an optical or electrochemical transduction technique is most desired.[67] Mostly, DNA determination relies on the probe ability to recognize nucleic acids of specific sequences by forming duplexes. Accordingly, a wide variety of hybridizing probes have been devised for SNP genotyping. Conformationally constrained probes, such as molecular beacons (MBs), are among them.[68] MBs are oligodeoxyribonucleotides (ODNs) hairpins with a fluorophore and a quencher, each conjugated to the opposite end of the ON. MBs binding to complementary nucleic acids results in their elongation, thus in

15

increasing their fluorescence. MBs distinguish mismatches over a wide temperature range.[69] MBs can recognize a single substitution in the central position of fifteen-mer ODNs.[69] Moreover, a conformational constraint approach can be combined in a binary DNA probe.[68] This approach demonstrates high selectivity of DNA recognition. For instance, single nucleotide substitution was reliably discriminated at any position of a twenty-nucleotide ON analyte at room temperature.[68] The probe was able to detect the true ON analyte in the presence of a 200-fold excess of a single nucleobase mismatched ON.

Not only DNA oligonucleotides but also their analogues were constructed, and then integrated with different transduction platforms for detection of ONs of mismatched sequences.[70] The first example involved an electrochemical DNA sensor with LNA as the probe for detection of the promyelocytic leukemia/retinoic acid receptor alpha fusion gene in acute promyelocytic leukemia.[71] However, a more cost-effective and facile sensing strategy relying on dual-probe detection was developed when oligonucleotide probes modified with 2′- fluororibonucleic acid (2′-F RNA) monomers were introduced into the biosensor.[71] In a DNA-analogue based chemosensor, a 'sandwich' sensing mode was used, which involved a pair of LNA probes, a capture probe immobilized on the electrode surface through the Au-S bond, and the reporter probe biotinylated for interaction with streptavidin-(horseradish peroxidase).[71] In the presence of the target DNA, the capture probe and the reporter probe caught the target DNA to form a 'sandwich' sensing construct. A streptavidin-(horseradish peroxidase) construct, connected to the biotin label via streptavidin-biotin affinity binding, offered an enzymatically amplified electrochemical signal. The DNA target with its complementary DNA fragment was detected with the impressive LOD of 84 fM and the linear dynamic concentration range of 0.5 to 15 pM. This sensor was sufficiently selective to distinguish ONs of the complementary sequence from those of different mismatch sequences.

In another study, a fourteen-nucleobase anthraquinone-labeled pyrrolidinyl PNA probe was immobilized on a chitosan-modified disposable screen-printed carbon electrode via C terminal lysine residue using glutaraldehyde as the cross-linking monomer.[72] This electrochemical sensor quantitatively detected human papillomavirus (HPV) type 16 DNA, an important biomarker for cervical cancer. Moreover, this PNA bound to the target DNA more effectively and selectively than the DNA probe did. The calibration curve exhibited a linear dynamic concentration range of 20 nM to 12.0 μM.

The LOD was 4 nM and the limit of quantization (LOQ) was 14 nM.[72] Therefore, this chemosensor detected DNA from PCR samples. Moreover, the devised chemosensor required a sample volume smaller than that used for detection with DNA-probe based biosensors. Electrochemical chemosensing can be applied for direct detection of HPV in clinical samples.

With the PNA-functionalized reduced graphene oxide (RGO) field-effect transistor (FET) chemosensor, DNA was detected with high selectivity and a very low LOD of 100 fM.[73] One-nucleobase mismatched DNA hybridization with the PNA probe was not much effective, thus resulting in a low detection signal. It was possible to regenerate this chemosensor ten times without appreciable loss of its activity.

The strategies used for quantification of circulating tumor DNA (ctDNA) are difficult to realize because they include the need of labeling, the complexity of operation, and the inability of simultaneous dual detection of the DNA genetic mutation and methylation.[70] Therefore, a new strategy of recognition of ctDNA was developed involving the use of a PNA probe analogue combined with localized surface plasmon resonance (LSPR) spectroscopy and the coupling plasmon mode of gold nanoparticles (AuNPs).[70] This thermally-controlled plasmonics based refractometric chemosensor detected both mutation at two hot-spots and methylation of ctDNA. Based on the thermal sensitivity of the PNA for mismatch binding, the designed PNA probes perfectly matched mutant forms with one mismatch for normal circulating DNA (ncDNA). Immunogold colloids caused a 107% increase in the LSPR peak shift, which improved the LOD from 200 to 50 fM ctDNA.[70]

1.2.3 Molecularly imprinted polymers (MIPs)

Molecularly imprinted polymers (MIPs) have encountered a pronounced interest in chemosensing over past few decades because of their advantageous properties (Table 1.2-1), compared to those of antibodies in terms of stability, simplicity of synthesis and ease in integration with transducers.[74] Potential applications of MIPs involve compounds separation, selective chemical synthesis, artificial enzymatic reactions, bio- and chemosensing, drug delivery, neutralization of toxic macromolecular biocompounds in body, and targeted gene therapy.[74]

Molecular imprinting in polymers is a process where the target molecule or its close analogue acts as a template around which functional monomers accompanied by cross-

linking monomers are arranged by self-assembling, and then copolymerized to form a cast-like shell.[75]   Preparation of MIPs involves at least three steps (Scheme 1.2-2). First, functional monomers in solution form a pre-polymerization complex with a template through covalent, non-covalent, or semi-covalent interactions.[76] Then, after polymerization, the template is removed from the MIP net, which exposes recognizing sites in molecularly imprinted cavities thus generated. These cavities, held in place by the cross-linked MIP structure, are complementary to the template molecules with their size, shape as well as position and orientation of the recognition sites. Therefore, an MIP binds, and thus recognizes the analyte selectively.

Table 1.2-1. Comparison of selected features of natural and MIP recognition units.[74]

Feature	Natural recognition element	MIP
Binding affinity	High affinity/specificity	Varies (especially for macromolecular templates)
Generality	One receptor per analyte	MIPs can be developed virtually for any template
Robustness	Limited stability (each unit has its own operational requirements)	Stable under variety of conditions (pH, temperature, ionic strength, solvents)
Cost	Expensive synthesis but cost effective	Inexpensive
Storage	Days at room temperature	Long-term storage without loss in performance
Synthesis/preparation	Time-consuming	Facile
Sensor integration	Low compatibility with a transducer surface	Fully compatible with a transducer surface
Infrastructure required	Expensive analytical instruments/skilled labor	Label-free detection
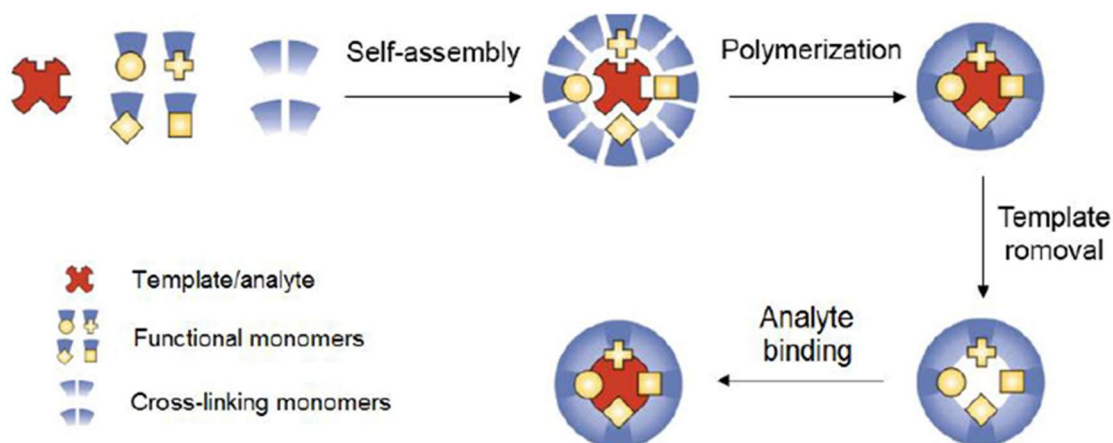
Scheme 1.2-2. Preparation of a molecularly imprinted polymer (MIP).

Molecular imprinting of small-molecule compounds is now quite well developed. However, a little progress has been made in devising MIPs for selective recognition of several important macromolecular biocompounds. The main reason of it is the macromolecule size, structural complexity, and conformational instability. Moreover, the polymerization conditions are mainly non-physiological. Therefore, these conditions affect the template structure and conformation, often being different than those natural. Another major obstacle is the solvent, which should not interfere with the monomer-template interaction but still allow for complete dissolution of all of the mixture components.

To date, several different DNA sensors have been devised[77] but the number of those using MIP films as recognition units is growing only slowly.[78-79] Different imprinting methods were developed for recognition and determination of nucleic acid targets ranging from small nucleobases[80-82] to long chain ssDNA[83] as well as dsDNA.[84] However, the possibility of preparation of an MIP engaging the programmable ODN template for controlling sequence of the oligomer prepared via electropolymerization of nucleobase-substituted functional monomers, including molecular imprinting of non-labeled ONs using Watson-Crick nucleobase pairing,[85] has not been explored yet.

Most of the strategies involved syntheses of MIP films in aqueous solutions. First example of DNA imprinting involved free-radical polymerization, in the HEPES buffer, of 2-vinyl-4,6-diamino-1,3,5-triazine (VDAT) with the acrylamide functional monomer and the methylenebisacrylamide cross-linking monomer in the presence of the DNA template. This synthesis resulted in an MIP thin film capable of recognizing synthetic

dsDNA (34 nucleobase pairs) of the sequence identical to that of the verotoxin gene.[84] (Verotoxin gene)-templated MIP film formation was based on the A-T nucleobase pairing of the dsDNA template and VDAT. Selectivity of this MIP film was investigated with respect to the fluorescent-labeled non-target dsDNA where the A-T nucleobase pairs were replaced by the G-C pairs. The fluorescence intensity of the MIP film after binding the verotoxin dsDNA was twice that after interference binding.[84]

Other methods of preparation of the DNA-imprinted MIP films involved electrochemical polymerization. With the 5'-TGAGCCGCTTGAGGTTG-3' ODN, used as the template and 1,2-phenylenediamine as the functional monomer, an amperometric MIP chemosensor for this ODN determination was fabricated by electropolymerization leading to MIP film deposition on an indium-tin oxide (ITO) glass electrode substrate.[83] The linear dynamic concentration range of the resulting chemosensor covered an impressively broad concentration range of 0.01 to 300 fM 5'-TGAGCCGCTTGAGGTTG-3'.

In another study, dsDNA was determined using a DNA-imprinted polypyrrole film deposited on a graphite electrode under potentiodynamic conditions with potential pulse sequences. The >N-H (imine) group of the pyrrole moiety formed a hydrogen bond with the >C=O (carbonyl) group of the DNA nucleobase. This DNA-templated MIP film was sensitive to the ON of the target sequence, in contrast to the non-imprinted polypyrrole film.[86]

In organic solvent solutions, molecular imprinting is more effective than in aqueous solutions, particularly if a non-covalent binding is involved.[87] To date, most MIP syntheses involving non-covalent template binding were performed using organic solvents in order to avoid water competition in hydrogen bonding operative in the pre-polymerization complex formation. For that purpose, the organic-solvent-soluble derivatives of all five nucleobases were used as templates.[88] Among them, MIPs prepared using genuine nucleobases are most desired because the ultimate objective of this imprinting is recognition of native components of nucleic acids. Unfortunately, most components of nucleic acids of biological origin are insoluble in organic solvents. Therefore, functional monomers soluble in aqueous solutions were designed to meet this solubility requirement.[83-84,86]

Surprisingly, the possibility of preparation of an MIP engaging specific Watson-Crick like nucleobase pairing between a single-stranded ODN template and a functional monomer has so far not been explored. Presumably, that was because the negative

Gibbs free energy change accompanying this pairing, i.e., stability of a pre-polymerization complex, is quite low in polar solvents. One way of this energy change increasing is to replace polar solvents with solvents of low polarity. So far, only a few supramolecular systems mimicking natural nucleobase pairing of A-T and C-G[89] in DNA as well as those of adenine-uracil (A-U)[80] in RNA have already been devised. However, these examples involve artificial small-molecule receptors. None of them has engaged the DNA-like complementary purine-pyrimidine nucleobase pairing in molecular imprinting. The following example fills this gap.[10]

A new strategy of simple, inexpensive, rapid, and label-free SNP detection using robust chemosensors with piezomicrogravimetric (PM), SPR spectroscopic, or capacitive impedimetric (CI) signal transduction was reported.[10] With these chemosensors, a genetically relevant TATAAA oligonucleotide was selectively determined under FIA conditions within 2 min. For this chemosensor, an invulnerable to non-specific interaction MIP with electrochemically synthesized probes of hexameric 2,2'-bithien-5-yl DNA analogues discriminating single-purine mismatch at room temperature was used. The artificial hexamer strongly hybridized TATAAA with the complex stability constant, $K_s^{\text{TTTATA-TATAAA}} \approx 10^6$ M^{-1}, as high as that characteristic for longer-chain DNA-PNA hybrids. The CI chemosensor revealed the 5-nM LOD, quite appreciable as for the hexadeoxyribonucleotide.[10] The molecular imprinting increased the chemosensor sensitivity to the TATAAA analyte over four times compared to that of the non-imprinted polymer. Moreover, the MIP chemosensing performance was not affected by interfering components of real samples. Furthermore, in molecular cavities of another MIP prepared according to the same procedure, octameric 2,2'-bithienyl-5-yl DNA analogue probe[9] was integrated with either the EIS or SPR-FIA signal transducer to fabricate chemical sensors for determination of the 5'-GCGGCGGC-3' analyte.

1.3 (DNA aptamer)-MIP hybrids

An approach of a great promise in macromolecular imprinting involves integration of an MIP matrix with biomolecules exhibiting high affinity for a particular target, thus giving rise to a so-called hybrid-MIP system.[90] Macromolecular biocompounds, such as lipopolysaccharides and lectins (carbohydrate-binding protein, e.g., concanavalin A), were determined using the polymyxin cyclic peptide and mannose, respectively.[90-91] Formation of these hybrid systems is substantiated by affinity and selectivity

improvement above that encountered in case of the biocompounds alone via this templating.

Among hybrid-MIP systems, there are nucleobase-containing polymers. Presumably, the most significant of them are those synthesized by introducing nuclease-resistant and versatile aptamers as macromonomers in MIPs.[79] Aptamers are short and stable ONs capable of binding, with high affinity and selectivity, different targets ranging from low- to high molecular-weight compounds, such as proteins.[79] DNA aptamers are obtained through combinatorial selections. They can be evolved to bind different target analytes. These features make them attractive alternatives to antibodies in sensing and diagnosing, even though they are quite sensitive to both enzymatic and chemical degradation. The reason of inserting them in an MIP matrix is that they improve MIP binding affinity. Then, the aptamer acts as the recognition unit.

Recently, full-length aptamers were introduced into molecularly imprinted hydrogels for detection of thrombin protein[92] and different viruses.[92] However, the performed for this purpose modification of the aptamer resulted in an unfavorably flexible DNA strand. A quite different approach involved chemical modification of the aptamer, thus providing a chance to synthesize the polymerizable biorecognition unit.[93]

Protein-specific aptamers were incorporated in MIPs to fabricate volume-changing hydrogels. A strategy of preparation of these hydrogels involves protein imprinting with polymerizable bioreceptors. Then, copolymerizing with hydrogel monomers leads to devising a material responsive to a target protein.[92] For instance, one of these hydrogels revealed an amplified response to the target thrombin.[92] For preparation of this hydrogel, two aptamers were chemically modified (linked) with polymerizable methacrylamide moieties. Then, the stoichiometric pre-polymerization complex of the thrombin template with aptamers (Scheme 1.2-3a, and 1.2-3b) was formed.[92] In this complex, molecules of biocompounds bearing positively charged moieties were non-specifically adsorbed on non-complexed aptamer molecules bearing negatively charged nucleotides. Polymerization of methacrylamide moieties of this complex resulted in a hydrogel (Scheme 1.2-3c). Subsequent removal and then reinsertion of the thrombin template led to swelling and shrinking, respectively, of the hydrogel. This removal reversibly disrupted cross-link bindings. Moreover, for monitoring the progress of disease or treatment, oligonucleotide analogues and mimics can be used for localized and controlled release of protein drugs. For example, multiple protein drugs were released in a programmable way from aptamer-functionalized hydrogels via nucleic

22

acid hybridization.[94] The most favorable (DNA aptamer)-MIP hybrid was designed for devising an electrochemical sensor for prostate specific antigen (PSA).[90] In this example, a pre-polymerization complex of a thiolated DNA aptamer with the PSA template was immobilized on a gold electrode surface. By this immobilization, the order and homogeneity of the resulting hybrid system was favored. The molecular imprinting step was accomplished by electropolymerizing dopamine onto the aptamer-PSA modified electrode. Multiple layers of polydopamine acted as a supportive and protective scaffold for the aptamer. Moreover, they contributed to PSA binding by partial entrapping the protein molecule in the surface-confined imprinted cavity. This cooperativity of the aptamer and dopamine in analyte binding amplified the sensor response. The performance of this aptamer-MIP sensor was evaluated with EIS. It appeared that this sensor was highly sensitive to PSA with a broad linear dynamic concentration range of 100 pg ml^{-1} to 100 ng ml^{-1} PSA and the LOD of 1 pg ml^{-1}. Advantageously, this LOD was three-fold lower than that of the aptamer alone sensor for PSA. Furthermore, this sensor demonstrated low cross-reactivity with a homologous protein and low response to human serum albumin (HSA), thus suggesting possible resilience to the non-specific binding of serum proteins.

In the above examples, full-length aptamers were used. Next idea was to use aptamer fragments as macromonomers to improve MIPs performance, and then gradually shorten this fragment to allow for a lower cost and higher stability.[79] For high adenosine template accessibility, MIP hydrogel NPs were prepared in this study. First, the DNA aptamer was split into two halves, then fluorescently labeled, and then copolymerized to result in an MIP. With fluorescence quenching, template complexation, and then template imprinting was confirmed. Further studies were carried out using isothermal titration calorimetry (ITC). The (DNA aptamer)-MIP hybrid doubled the binding affinity to adenosine compared to that of the mixture of the free aptamer fragments whereas each aptamer fragment alone was unable of binding this analyte. Next, one of the aptamer fragments was shortened even more making the DNA length as short as to contain only six nucleotides. Nevertheless, tight binding was still retained. In that way, a method for preparing MIP hybrid materials by combining biopolymer fragments with savings in cost of their syntheses using monomers was provided, thus resulting in new functional materials featuring increased binding affinity.

Scheme 1.2-3. (a) and (b) Chemically modified aptamers used in (c) the protocol of preparation of a superaptamer thrombin-responsive hydrogel.[92]

http://rcin.org.pl

Chapter 2

Experimental

This section includes description of all chemicals, instrumentation, techniques, and procedures used for conducting experiments presented in the thesis.

2.1 Chemicals

All oligodeoxyribonucleotides were purchased from Oligo.pl (Institute of Biochemistry and Biophysics PAS, Warsaw, Poland).

All peptide nucleic acids (PNAs) were synthesized using standard manual *tert-butyloxocarbonyl* (BOC) based chemistry, according to the literature procedure,[95] in the Chemistry Department of the University of Milan, Milan, Italy.

Table 2.1-1. Oligodeoxyribonucleotides (ODNs).

1.

5'-TATAAA-3'
Template/Analyte

2.

5'-TATA**G**A-3'
Mismatched ODN

3.

5'-TATAA**G-3'**
Mismatched ODN

4.

5'-GCGGCGGC-3'
Analyte ODN

5.

5'-GCG**AT**GGC-3'
Mismatched ODN

Table 2.1-2. Peptide nucleic acids (PNAs).

6.

H₂N(CO) TATAAA-NH₂
Template PNA

7.

H₂N(CO) GCGGCGGC NH₂
Template PNA

8.

H₂N(CO)GCT**G**CT**G**C NH₂

Mismatched PNA

9.
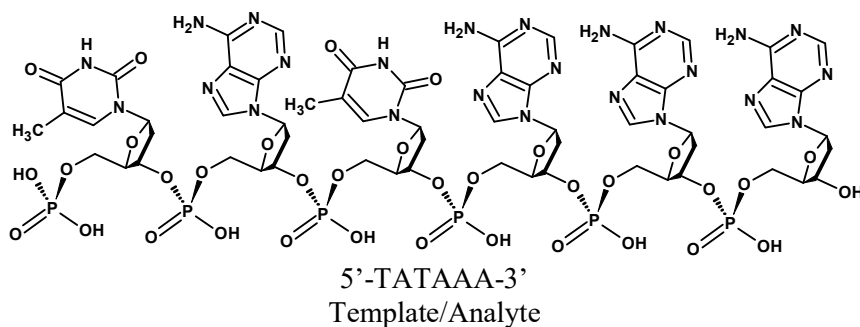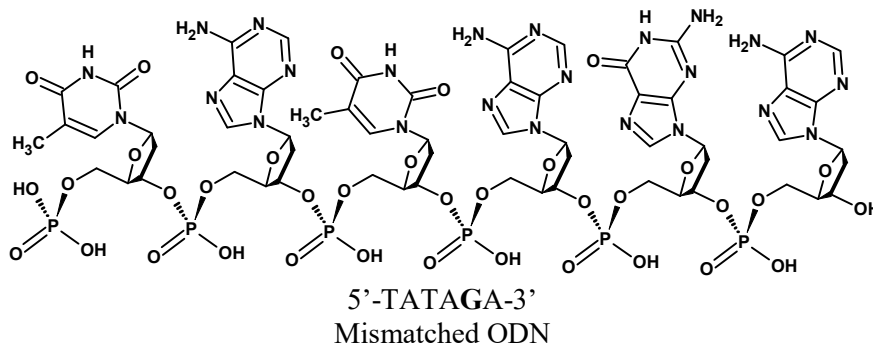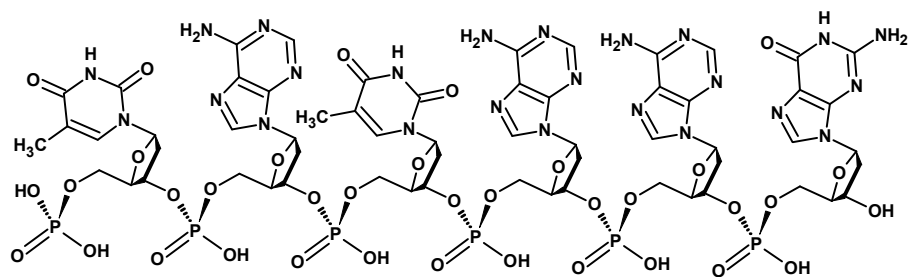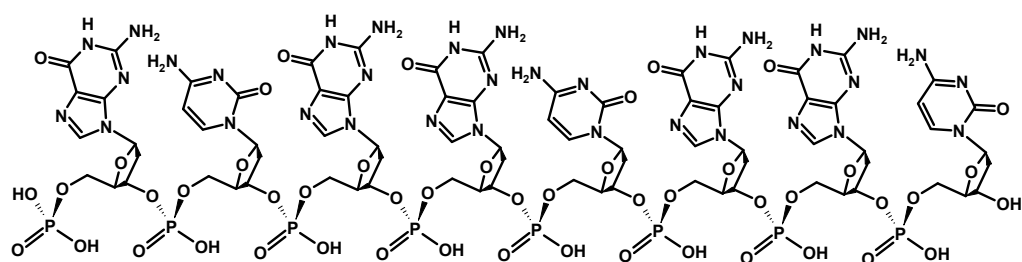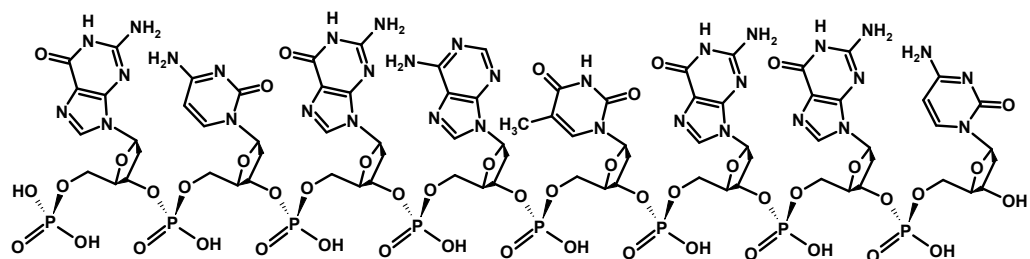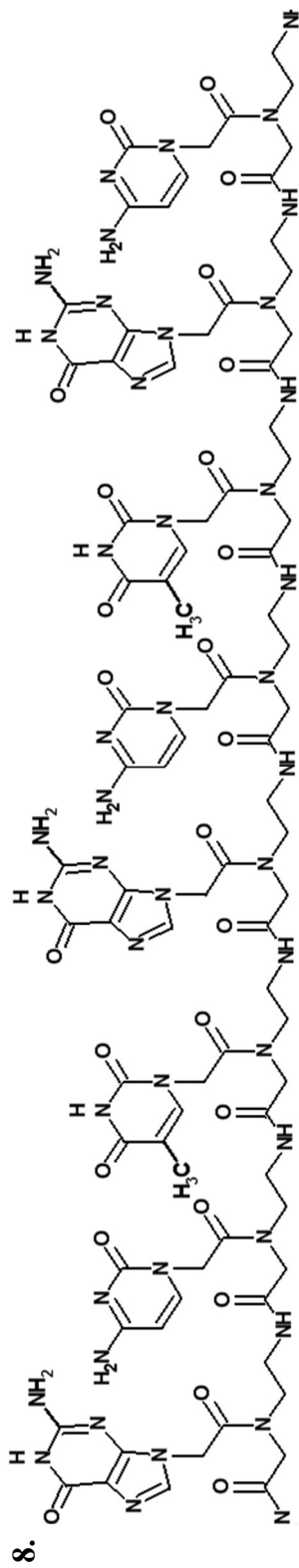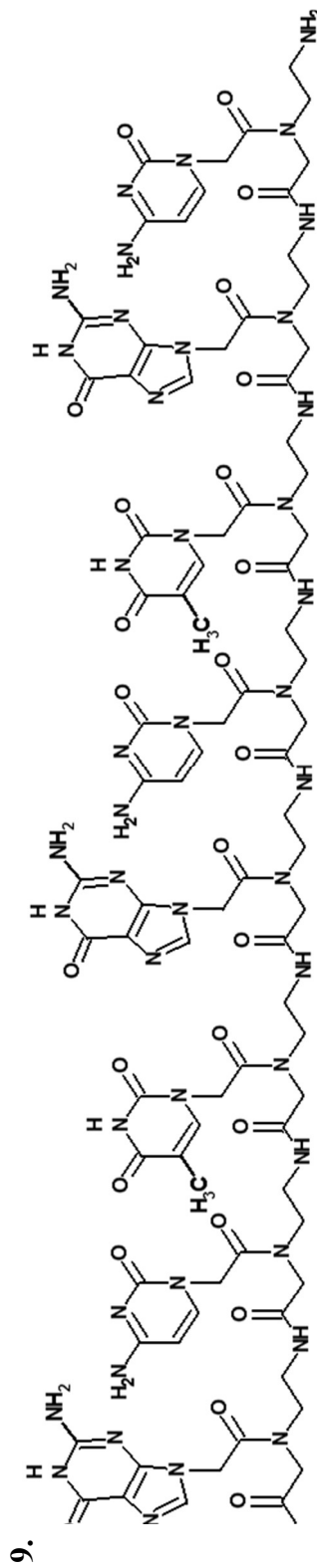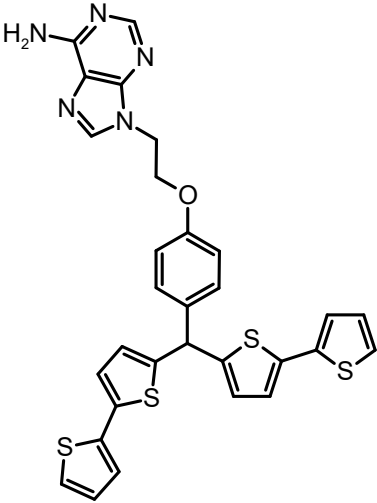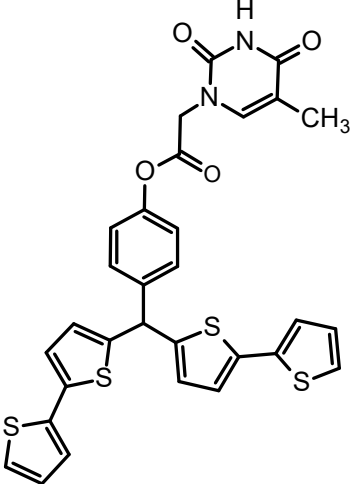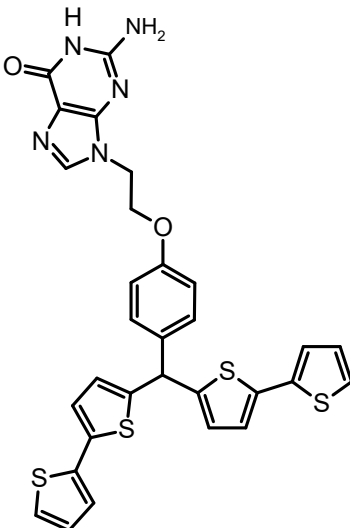
H₂N(CO)GCG**A**T**C**GC NH₂

Mismatched PNA

Table 2.1-3. Monomers.

No.	Name and function	Structural formula	Source
10.	4-(Bis(2,2'-bithien-5-yl)methylphenyl-2-adenine ethyl ether The functional monomer for the 5'-TATAAA-3' chemosensor		Synthesized at the University of North Texas, Denton TX, USA
11.	4-(Bis-2,2'-bithien-5-yl)methylphenyl thymine-1-acetate The functional monomer for the 5'-TATAAA-3' chemosensor		Synthesized at the University of North Texas, Denton TX, USA
12.	4-Bis(2,2'-bithien-5-yl)methylphenyl-2-guanine ethyl ether The functional monomer for the 5'-GCGGCGGC-3' chemosensor		Synthesized at the University of North Texas, Denton TX, USA

29

13. 2-(Cytosin-1-yl)ethyl 4-bis(2,2'-bithien-5-yl)methylbenzoate The functional monomer for the 5'-GCGGCGGC-3' chemosensor		Synthesized at the University of North Texas, Denton TX, USA
14. 2,4,5,2',4',5'-*Hexa*(thiophene-2-yl)-3,3'-bithiophene The cross-linking monomer		Synthesized at the University of Insubria, Insubria, Italy
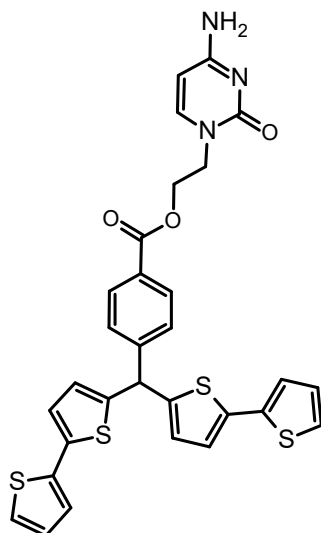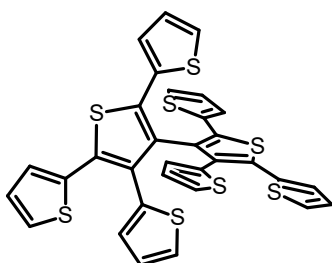
Other chemicals used are listed below. They were used, as received.

- Acetonitrile (sure seal), CH_3CN – Sigma Aldrich

- Dimethyl sulfoxide (≥ 99 %), DMSO – Sigma-Aldrich

- Disodium phosphate (analytical grade), Na_2HPO_4 – POCH

- Dulbecco's Modified Eagle's Medium (DMEM) – Ludwik Hirszfeld Institute of Immunology and Experimental Therapy, Polish Academy of Sciences, Wrocław

- Isopropanol (analytical grade) – CHEMPUR

- L-Serine, L-lysine, L-glutamic acid, L-asparagine, L-threonine, L-valine, L-phenylalanine, and L-leucine amino acids – Sigma-Aldrich

- Methanol (analytical grade), CH_3OH – STANLAB

- Monopotassium phosphate (analytical grade), KH_2PO_4 – POCH

- Potassium chloride (analytical grade), KCl – POCH

- Potassium nitrate (analytical grade), KNO_3 – CHEMPUR

- Potassium hexacyanoferrate(III), $K_3Fe(CN)_6$ – Sigma-Aldrich

- Potassium hexacyanoferrate(II), $K_4Fe(CN)_6$ – CHEMPUR

- Sodium chloride (analytical grade), NaCl – POCH

- Sodium fluoride (analytical grade), NaF – Fluka

- Sodium hydroxide (analytical grade), NaOH – POCH

- Tetra-*n*-butylammonium perchlorate (electrochemical grade), (TBA)ClO$_4$ – Merck

- Triethylamine ($\geq$ 99%), – Sigma-Aldrich

- Trifluoroacetic acid ($\geq$ 98%), – Fluka

- Toluene (sure seal) – Sigma Aldrich

2.2 Instrumentation and procedures

This section provides description of instrumentation and procedures used in the research presented.

2.2.1 General procedure of preparation of polymers molecularly imprinted with oligonucleotides

General procedure of preparing polymers molecularly imprinted with ONs consisted of five consecutive steps. The first one included designing and synthesizing functional monomers. Inspired by the Watson-Crick DNA double helix structure,[85,96] the 4-bis(2,2'-bithien-5-yl)methylphenyl monomer was derivatized with one out of four nucleobases, namely, A, G, T, or C, to result in four functional monomers, each bearing different nucleobase.

Before synthesizing these functional monomers, computational calculations for the pre-polymerization complexes of these monomers with templates were performed in the second step. From these calculations, negative changes of Gibbs free energy, ΔG, of formation of complexes of these monomers with ONs were obtained and structures of the complexes were optimized.

In the third step, functional monomers and the selected template, together with the cross-linking monomer, were dissolved in the mixture of solvents in order to form a pre-polymerization complex. Moreover, this step involved experimental verification of complex formation, which was accomplished with ITC.[97] The ITC experiment confirmed the assumed (based on the complementary nucleobase pairing rule) stoichiometry of the complexes as well as provided values of the complex stability constant, K_s. and other thermodynamic parameters.

After that, complexes were immobilized in the fourth step, as polymer films, on the surfaces of different electrodes by potentiodynamic polymerization. The potentiodynamic technique allowed for controlling roughness and thickness of the deposited films. After electropolymerization, these films were rinsed with abundant solvent, used to prepare a solution for electropolymerization, to remove unbound pre-polymerization complex components and the supporting electrolyte salt.

Finally, the templates were extracted from these films under different conditions depending on the template nature. In this extraction, cavities imprinted in the MIPs

were emptied, thus making them available for reversible analyte binding and in this way recognizing.

Non-imprinted polymer (NIP) preparation involved electropolymerization of the selected functional and cross-linking monomers under the same conditions as those used for preparation of the corresponding MIP film, however, in the template absence.

2.2.2 Computational modeling and quantum-chemistry calculations

All computational calculations were performed using Gaussian 09 software[98] (Gaussian, Inc., CT, USA) installed on the workstation with four Intel dual-core processors. The density functional theory (DFT), a computational quantum-chemical modeling method at the B3LYP/3-21G level was employed to calculate Gibbs free energy changes accompanying formation of complexes of templates with functional monomers and to optimize structures of these complexes. For that, first, 3-D structures of the pre-polymerization complexes were drawn using GaussView software. Then, DFT calculations on these input files were run using Gaussian 09 software. Structures of a template molecule, functional monomer molecules, and their complexes were optimized separately. From calculations, the ΔG values characterizing formation of pre-polymerization complexes were obtained.

2.2.3 Isothermal titration calorimetry (ITC) and differential scanning calorimetry (DSC) instrumentation

The ITC experiments were performed at constant atmospheric pressure and constant temperature of 295 K on a NanoITC calorimeter (TA Instruments) controlled by software of the same manufacturer. Both analytes and titrants were dissolved in DMSO to prepare solutions of sufficiently high concentrations required for these titrations. Before titration, these solutions were deaerated under decreased pressure in the degassing station (TA Instruments). For proper baseline development, an 1800-s time delay was allowed. After this time, the titration was initiated with injections of 10-μL or 8-μL titrant solution samples with the increment time of 3 min, under magnetic stirring conditions kept constant at 250 rpm. In total, a 250 μL of each titrant solution was added to a 940-μL sample of the appropriate analyte solution placed in the ITC measuring cell.

Moreover, thermal properties of the complex of PNA $H_2N(CO)$TATAAA-NH_2 with 4-(bis(2,2'-bithien-5-yl)methylphenyl-2-adenine ethyl ether **10** and 4-(bis-2,2'-bithien-5-yl)methylphenyl thymine-1-acetate **11** were characterized by differential scanning calorimetry (DSC). For that, samples of the complex solution and the reference DMSO solvent, each 300 µL in volume, were loaded into their respective reservoirs of the NanoDSC calorimeter (TA Instruments). The studied sample was scanned against the reference sample over the temperature range of 22 to 70 °C at a rate of 1 °C min^{-1}. The data were acquired and processed using NanoAnalyze™ Software v3.2.0 (TA Instruments).

2.2.4 Pretreatment of electrodes

Before measurements, 1-mm diameter Pt disk electrodes were polished, consecutively, with the alumina slurry of the 1.0, 0.3, and 0.05-µm diameter, then rinsed with deionized water, and then sonicated in ethanol for ~5 min. For reusing, the electrode was dipped in a mixture of sulfuric acid and hydrogen peroxide (Piranha solution) for 5 min. (Caution. Piranha solution is dangerous when contacting skin or eye.) After deposition of a polymer film on the Pt electrode surface, the electrode was used for differential pulse voltammetry (DPV), EIS, and CI measurements.

The 14-mm diameter AT-cut plano-plano 10-MHz quartz crystal resonator (QCR) with 5-mm in diameter and 100-nm thick Au film vapor deposited over a 10-nm thick Ti underlayer was first cleaned with methanol, and then with isopropanol under 5-min sonication in each of these solvents. The Au film of QCR served as the working electrode for piezoelectric microgravimetry (PM) experiments performed using a quartz crystal microbalance (QCM).

Au-glass slides with a thin (100 nm) Au film layer sputtered over a thin (15 nm) Ti underlayer (Institute of Electronic Materials Technology, Warsaw, Poland) and commercial BK7 24-mm diameter Au-glass disk (Autolab-Metrohm) were cleaned by 5-min sonication in methanol, and then in isopropanol. Au-glass slides with deposited polymer films were then used for atomic force microscopy (AFM), polarization-modulation infrared reflection-absorption spectroscopy (PM-IRAAS), and X-ray photoelectron spectroscopy (XPS) characterization as well as for extended-gate field-effect transistor (EG-FET) sensing. A polymer coated Au-glass disk served as the sensing platform in the surface plasmon resonance (SPR) spectroscopy measurements.

2.2.5 Instrumentation for preparation of MIP and NIP films

Potentiodynamic polymerization was performed with an SP-300 Modular Research Grade Potentiostat/Galvanostat/FRA of Bio-Logic Science Instruments SAS, controlled by EC-lab software of the same manufacturer. Each MIP and NIP film was deposited on a Pt disk working electrode placed in a V-shaped three-electrode electrochemical glass mini cell (Scheme 2.2-1) together with an Ag|AgCl and a Pt wire serving as the reference and auxiliary electrode, respectively. The potential range of 0.50 to 1.25 V and a scan rate of 50 mV s^{-1} were used for preparation of MIP and NIP films.
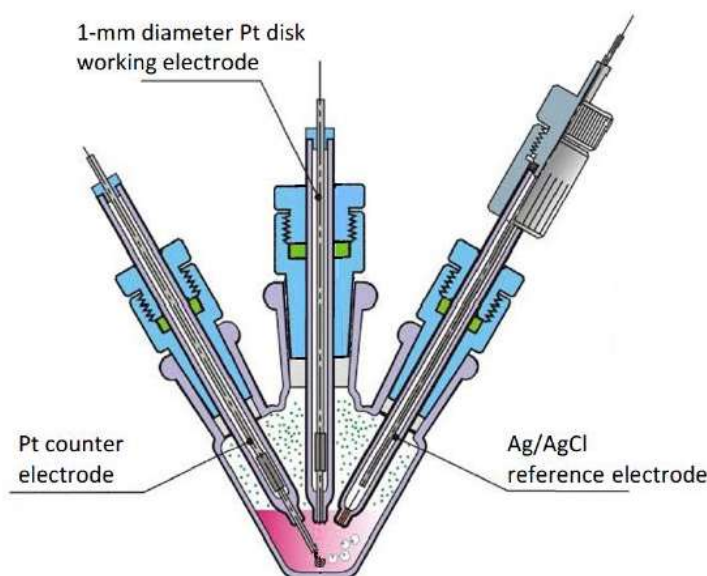
Scheme 2.2-1. The cross-sectional view of the three-electrode electrochemical mini cell.

Moreover, the polymer films were deposited on gold electrodes of QCRs by potentiodynamic electropolymerization performed with the EP-20 Potentiostat (IPC PAS, Warsaw). The PM signal was recorded on the EQCM 5710 electrochemical quartz crystal microbalance[99] (IPC PAS, Warsaw) coupled with the potentiostat. The PM data were acquired and processed with EQCM 5710-S2 software of the same manufacturer. For polymer potentiodynamic deposition, the EQCM 5710 holder (Scheme 2.2-2a) was mounted horizontally with the gold electrode of a quartz crystal resonator (Scheme 2.2-2b) facing upwards (Scheme 2.2-2c). A 5-mm coiled Pt wire serving as the counter electrode was placed in a close proximity of the gold electrode,

thus providing uniform electric field intensity. An Ag wire coated with the AgCl film was used as the pseudo-reference electrode. All electrodes were dipped in a 150-µL sample of a pre-polymerization complex solution.

For SPR measurements, the polymer film was first deposited on an Au-glass disk, used as the working electrode. Then, in this way coated disk was mounted in an SPR cuvette equipped with an Ag wire and an Ag|AgCl electrode serving as the counter and pseudo-reference electrodes, respectively. Potentiodynamic polymerization was performed with an AUTOLAB computerized electrochemistry system of Eco Chemie (Utrecht, The Netherlands), equipped with expansion cards of the PGSTAT12 potentiostat and the FRA2 frequency response analyzer, and controlled by GPES v.4.9 software of the same manufacturer.
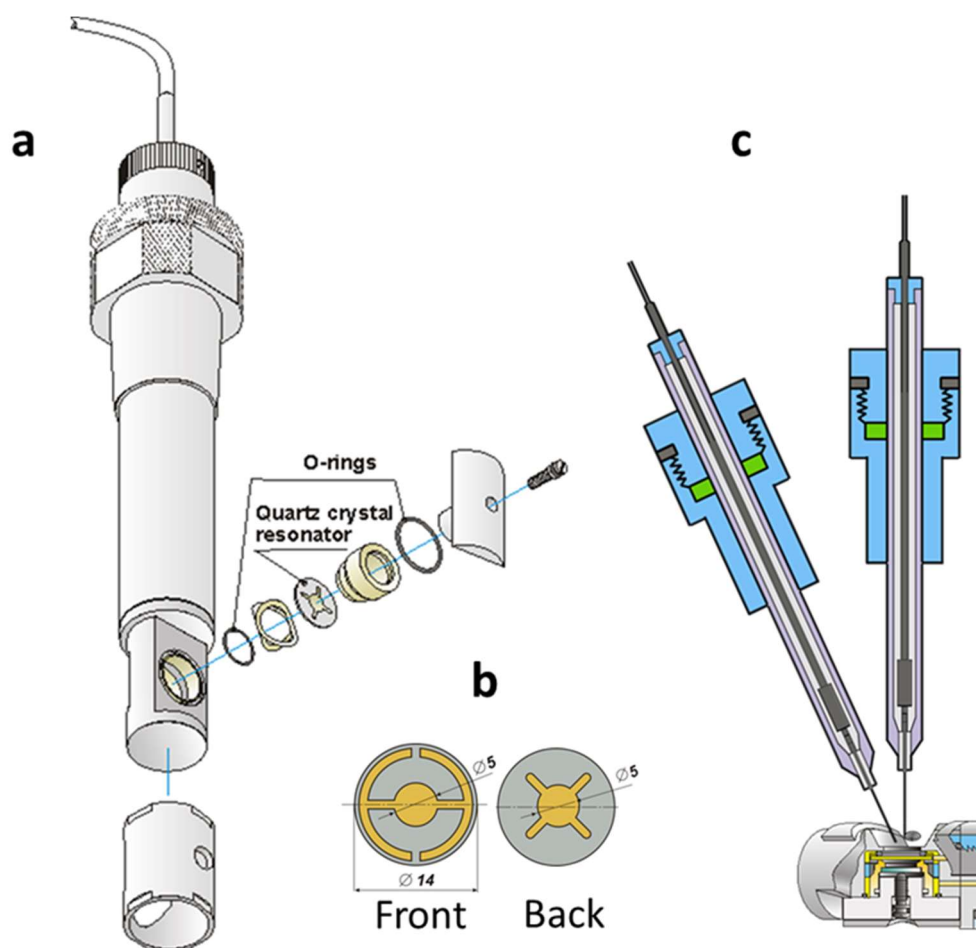
Scheme 2.2-2. (a) The expanded view of the quartz crystal holder of the EQCM 5710 microbalance, (b) the quartz crystal resonator, and (c) arrangement of the Ag pseudo-reference and Pt counter electrodes near the quartz crystal resonator mounted in the EQCM holder cavity.

2.2.6 Preparation of (5'-TATAAA-3')-templated MIP films

For formation of the pre-polymerization complex, the 5'-TATAAA-3' template (0.072 mg, 0.04 µmol) was dissolved in a solution of acetonitrile (0.75 mL), distilled water (0.10 mL), toluene (0.10 mL), and isopropanol (0.05 mL). Next, the A functional monomer **10** (0.06 mg, 0.1 µmol), the T functional monomer **11** (0.12 mg, 0.2 µmol), the cross-linking monomer **14** (0.13 mg, 0.2 µmol), and (TBA)ClO$_4$ (34 mg, 0.1 mmol) were added to the 5'-TATAAA-3' solution. After deposition of the (5'-TATAAA-3')-templated MIP film on the electrode, the 5'-TATAAA-3' template was extracted from the film with 0.1 M NaOH for 45 min at room temperature in order to vacate imprinted cavities in the MIP before recognizing the 5'-TATAAA-3' analyte. A control NIP film was prepared in the manner described in Section 2.2.1, above.

For preparation of the (PNA H$_2$N(CO)TATAAA-NH$_2$)-templated imprinted MIP film, the PNA H$_2$N(CO)TATAAA-NH$_2$ template (0.066 mg, 0.04 µmol) was dissolved in acetonitrile (1 mL). Next, A **10** and T **11** functional monomers, cross-linking monomer **14**, and (TBA)ClO$_4$, all in the amount same as that in the pre-polymerization complex solution of 5'-TATAAA-3', were added. Electropolymerization under the same conditions of the potential scan range and rate was performed for preparation of the (PNA H$_2$N(CO)TATAAA-NH$_2$)-templated MIP film. For PNA H$_2$N(CO)TATAAA-NH$_2$ template removal, the electrode with the deposited film was immersed in 20% trifluoroacetic acid for 45 min.

2.2.7 Preparation of the (PNA H$_2$N(CO)GCGGCGGC-NH$_2$)-templated MIP film

In order to prepare a pre-polymerization complex, the PNA H$_2$N(CO)GCGGCGGC-NH$_2$ template (0.445 mg, 0.02 µmol) was dissolved in a solution of acetonitrile (0.90 mL) and distilled water (0.10 mL). Next, the G functional monomer **12** (0.123 mg, 0.20 µmol), the C functional monomer **13** (0.236 mg, 0.39 µmol), the cross-linking monomer **14** (0.27 mg, 0.41 µmol), and (TBA)ClO$_4$, (34 mg, 0.1 mmol) were added to the PNA solution. The MIP was simultaneously prepared and deposited as a thin film on the electrode surface from the pre-polymerization complex solution by potentiodynamic electropolymerization. Sufficient thickness of the film on the Pt electrode was obtained within five potential cycles. After rinsing the film with abundant acetonitrile solvent, the electrode with the (PNA H$_2$N(CO)GCGGCGGC-NH$_2$)-templated MIP film was immersed in 0.1 M trimethylamine (pH = 12.0) at 60 °C for

1 h under magnetic stirring for PNA template extraction. For evaluation of imprinting efficiency, a control NIP film was prepared, as described in Section 2.2.1, above.

For SPR spectroscopic measurements, the MIP film was deposited on the Au-glass disk mounted in an SPR cuvette under the same potentiodynamic conditions. After deposition, the MIP film was wetted with 0.1 M trimethylamine for 3 h at room temperature in order to remove the PNA $H_2N(CO)GCGGCGGC-NH_2$ template. Longer extraction time at room temperature resulted in the same extent of template removal as that of 1-h removal at elevated temperature.

2.2.8 Instrumentation and procedures for spectroscopic and microscopic characterization of MIP films

Surface elemental composition of the MIP and NIP films was determined by XPS. Therefore, it was possible to verify the imprinting, and then to confirm the removal of the template from the MIP films. XPS experiments were performed with monochromatic Al Kα ($hv = 1486.4$ eV) radiation using the PHI 5000 Versa Probe-Scanning ESCA Microprobe instrument (ULVAC-PHI). The X-ray beam, focused to 100-μm diameter, was scanned over a (250×250) μm^2 surface area at operating power of 25 W (15 kV). The survey and core-level spectra were acquired using a hemispherical analyzer at pass energy of 117.4 eV with the 0.4 eV energy step and pass energy of 23.5 eV with the 0.1 eV energy step, respectively. XPS spectra were analyzed with CASA XPS software. Peaks were fitted using the mixed Gaussian-Lorentzian method and the background was subtracted using the Shirley method. Binding energy of the Au $4f_{7/2}$ peak ($BE = 84.0$ eV) was chosen as the internal BE reference.

PM-IRRAS spectra were recorded with the Vertex 80v spectrometer equipped with a PMA50 module and a nitrogen-cooled MCT (Hg-Cd-Te) detector. Angle of incidence of the p-polarized light beam was 83° to the normal to the Au-(polymer film) coated glass slide. This slide was mounted in a dedicated holder. Spectra were recorded with 2-cm^{-1} resolution. For each spectrum, 1024 scans were recorded. Positions of the bands in experimental spectra were determined with the procedure implemented in the Opus 6.5 software package. They were normalized with the use of the Min-Max and vector normalization to compensate for differences in polymer thickness and morphology. The

38

PM-IRRAS technique was used to compare composition of the MIP films before and after template extraction as well as to compare composition of the MIP and NIP films.

Topography of the polymer films was examined and their thickness determined using Multimode 8 microscope of Bruker equipped with a Nanoscope V controller operating in the PeakForce QNM mode. Samples were scanned using the Tapping mode™ with the spring constant of 42 N m^{-1} of the rotated tapping etched silicon probe (RTESP) provided by the same manufacturer. Some parts of the film were carefully removed in few different places from the electrode surface with a Teflon™ spatula, under an optical microscope, for determining average film thickness. From AFM images of these scratches, heights of the resulting steps were measured sufficiently far from partially detached polymer front by averaging the number of points on both sides of the step. The difference of the average values of points on the step and at its foot determined the height of the step. Finally, step heights measured for different scratches were averaged, thus resulting in an average value of film thickness.

2.2.9 Instrumentation and procedures for electrochemical MIP characterization

Template removal and then analyte recognition in the molecularly imprinted cavities of the MIP films were confirmed by DPV and EIS monitoring of the redox marker electroactivity. For that, an SP-300 Modular Research Grade Potentiostat/ Galvanostat/FRA of Bio-Logic Science Instruments SAS, controlled by EC-lab software of the same manufacturer was used. DPV and EIS measurements were performed in the V-shaped three-electrode glass electrochemical mini cell (Scheme 2.2-1) filled with 0.5 mL solution of 0.1 M $K_4Fe(CN)_6$ in 0.1 M KNO_3 for characterization of the MIP-TATAAA film or 0.1 M $[Fe(CN)_6]^{4-}$ and 0.1 M $[Fe(CN)_6]^{3-}$ in 0.1 M phosphate buffered saline, PBS (pH = 7.4) for characterization of the MIP-GCGGCGGC film. A Pt electrode coated with the polymer film, a Pt wire, and an Ag wire coated with the AgCl film served as the working, counter, and pseudo-reference electrode, respectively. For template extraction, the working electrode was dipped in an appropriate extraction solution, which was magnetically stirred. After extensive extraction, the electrode was transferred to an electrochemical cell filled with a blank supporting electrolyte solution. Before measurement of the redox marker electroactivity, the MIP film coated working electrode was polarized by potential scanning with a rate of 100 mV/min in the range of 0 to 0.50 V vs. Ag|AgCl pseudo-

reference electrode, cycled 20 times for establishing the steady state. DPV voltammograms were recorded after each step of extraction with a series of pulses superimposed on the potential linearly scanned in the range of 0 to 0.6 V. The potential step, pulse amplitude, and pulse width was 5 mV, 25 mV, and 50 ms, respectively. The EIS spectra were recorded in the 100 mHz to 200 kHz frequency range. The 10-mV amplitude of an alternating voltage was applied to the working electrode. Experimental data from the EIS measurements were fitted with parameters of equivalent circuits using ZView software of Scribner Associates, Inc.

For EIS determinations of ONs, different volumes of the 1 µM ON analyte were added to 1-mL sample solution of 0.1 M PBS, (pH = 7.4), 0.1 M $K_3Fe(CN)_6$, and 0.1 M $K_4Fe(CN)_6$. Then, the solution was stirred magnetically for 5 min, thus allowing the ON to interact with the template-extracted MIP and to reach complex formation-dissociation equilibrium. The EIS spectra were recorded after stabilization of the system by potential scanning. The same procedure was used for determination of ON mismatches. Calibration curves were constructed using fitting parameters of the equivalent circuit to the EIS data acquired.

The CI experiments were carried out under flow-injection analysis, FIA, conditions using experimental setup presented in Scheme 2.2-3, below.

The analyte interacted with the MIP film coated electrode in a specially designed radial-flow thin-layer electrochemical cell.[100] The 1-mm diameter Pt disk working electrode was axially mounted against the inlet capillary at the (capillary outlet)-to-electrode distance of 300 µm (Scheme 2.2-4). A coiled Pt wire and an Ag|AgCl electrode was used as the auxiliary and reference electrode, respectively. The 0.1 M NaF carrier solution was pumped through the electrochemical cell by KDS100 syringe pump of the KD Scientific, Inc. (Holliston MA, USA) supplier. The 200-µL samples of the analyte solutions of different concentration were injected to the carrier solution. The FIA experiments were performed at a carrier solution flow rate of 30 µL min^{-1}.
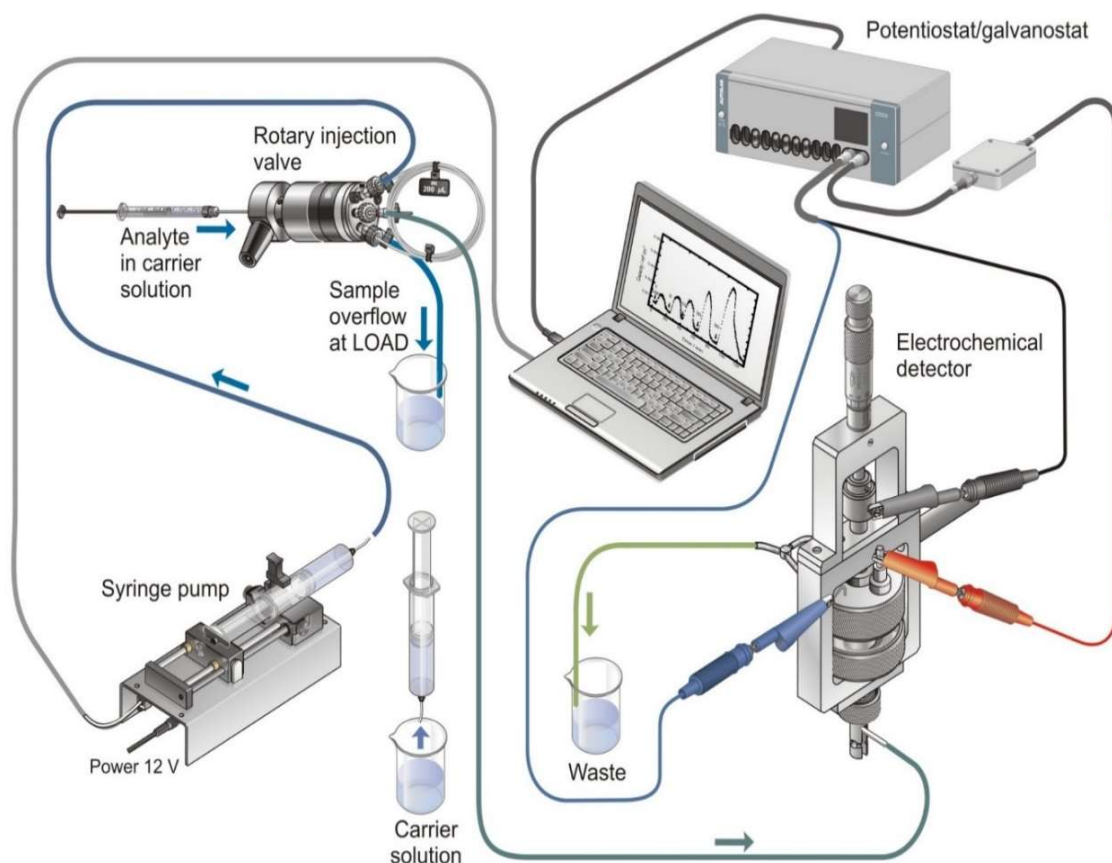
Scheme 2.2-3. The sketch of the experimental setup used for the capacitive impedimetry measurement, under flow-injection analysis conditions, on the MIP-extracted (or NIP) film coated 1-mm Pt disk electrode.

In CI determination, the electrical double-layer capacity, C_{dl}, was determined at the Pt-MIP interface by measuring the imaginary component of impedance, Z_{im}, at a sufficiently low and constant frequency, $f = 20$ Hz. The measurements were carried out at 0.50 V vs. Ag|AgCl pseudo-reference electrode with the sinusoidal voltage of the 10 mV amplitude applied in the absence of any redox marker. Under these conditions, only non-faradaic impedance was measured because the parameters characterized by the charge transfer, namely, the charge transfer resistance, R_{ct}, and the Warburg impedance, W, were infinitely large. Therefore, only Z_{im} was affected by the C_{dl} change. Because of using a relatively concentrated supporting electrolyte solution of non-adsorbing ions, vis., 0.1 M NaF, the capacity of the diffuse part of the double-layer did not contribute to the total capacitance, as the Helmholtz model predicts.
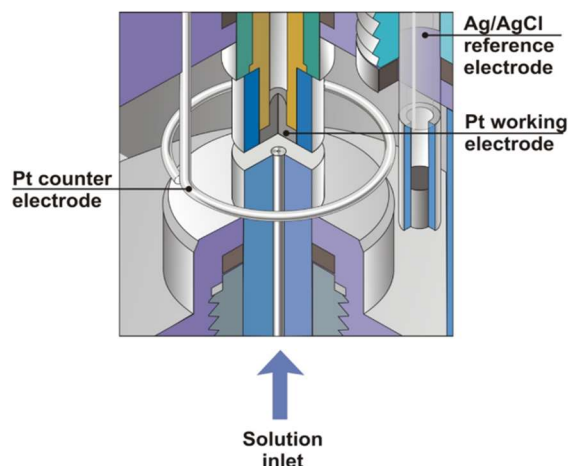
Scheme 2.2-4. The cross-sectional view of the design of the radial-flow thin-layer electrochemical cell.[100]

2.2.10 Instrumentation and procedure of MIP film characterization by piezoelectric microgravimetry (PM) at a quartz crystal microbalance (QCM)

Analytical, kinetic, and thermodynamic parameters of the MIP chemosensor were determined by PM carried out under FIA conditions. Before that, an ODN or PNA template was removed from the MIP film by pumping 0.1 mM NaOH or 20% CF$_3$COOH through vertically mounted laminar-flow thin-layer wall-jet cell of the EQCM 5610 holder[101] (Scheme 2.2-5) with the KDS100 syringe pump (KD Scientific, Inc.). In this way, the MIP film deposited on the gold electrode of a 10-MHz QCR was in contact with the extracting solution of a flow rate of 150 µL min^{-1} for 3 h. After that, the extracting solution was replaced by PBS (pH = 7.4), which was pumped at a low flow rate, namely, 30 µL min^{-1}. These conditions provided the laminar flow of the solution in the vicinity of the MIP film. The distance between the inlet capillary nozzle and the QCR surface was as small as 150 µm, thus providing conditions of thin-layer detection.[101] The 100-µL samples of the ODN or PNA analyte dissolved in PBS were injected to the carrier solution. The flow rate and injection volume were adjusted to reach well-defined PM signals composed of three parts corresponding to formation, equilibration, and dissociation of the MIP-analyte complex.
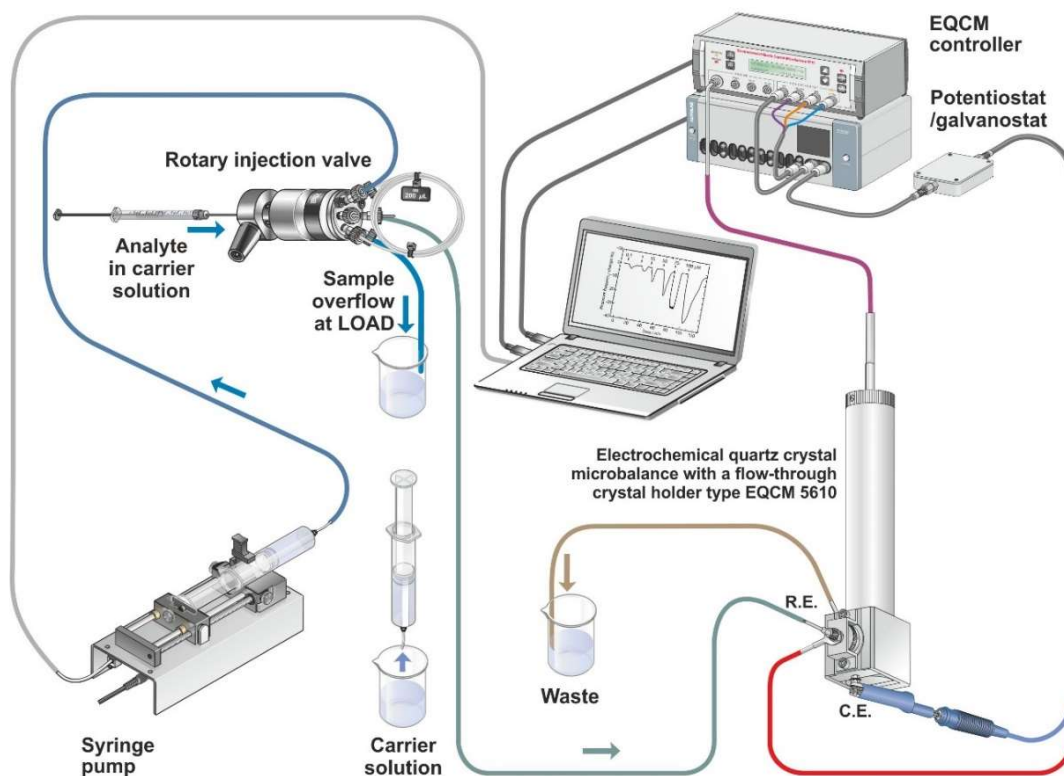
Scheme 2.2-5. The sketch of the setup used for piezoelectric microgravimetry measurements under flow-injection analysis conditions on the MIP-extracted (or NIP) film coated 10-MHz AT-cut quartz crystal resonator. This setup enabled simultaneous recording of the resonance frequency and dynamic resistance changes as well as current as a function of potential scanned.

2.2.11 Instrumentation and procedures for oligonucleotide determination by surface plasmon resonance (SPR) spectroscopy and extended gate-effect field-effect transistor (EG-FET) electric sensing

A dual-channel cuvette-based Autolab Esprit SPR instrument (Metrohm Autolab, Utrecht, The Netherlands), devised by Eco Chemie and controlled by ESPRIT v. 4.4 data acquisition software of the same manufacturer was applied for determination of ONs in solution. The dynamic range and angle resolution of the instrument was 4000 m° and < 0.02 m°, respectively. The measurements were recorded at fixed 670-nm wavelength. Before ON determination, an MIP film was deposited on a gold coated SPR disk. For that, a clean disk was placed in an SPR cuvette and a 150-μL sample of a pre-polymerization complex solution was dispensed by pipetting. After electropolymerization, the solution was washed away and the disk was first rinsed with isopropanol, and then with water.

Analytes were determined under either stagnant-solution or FIA conditions. In the former, the resonance minimum was recorded vs. angle of the laser beam reflected from the gold surface after dispensing 150-μL analyte samples of different concentrations in PBS (pH = 7.4) solution. After the SPR signal reached plateau, the solution was washed away. The PBS (pH = 7.4) solution was then pumped through the cuvette with a peristaltic SPR pump at a flow rate of 150 μL min^{-1}. After 5 min of polymer film regeneration, the next analyte sample was dispensed. During all experiments, the temperature was kept constant at 25(±1) °C.

For real-time determination of the ON analyte, the measurements were performed under FIA conditions. The PBS (pH = 7.4) carrier solution was pumped, at a flow rate of 33 μL min^{-1}, through an SPR cuvette equipped with a gold-coated glass disk with an MIP or NIP film deposited. After collecting data points in number sufficient for baseline constructing, the 50-μL samples of the ONs in PBS (pH = 7.4) solution were injected to the system with a syringe pump at a flow rate of 33 μL min^{-1}. The resonance angle changes were monitored instantly. This angle reached plateau after ~15 min. Then, dehybridization was accomplished by passing the PBS (pH = 7.4) carrier solution at the same flow rate.

The EG-FET sensing setup consisted of recognition and transduction units. The gold film electrodes of Au-glass slides coated with MIP or NIP films were used as extended recognition units. These electrodes were integrated with the transduction unit, i.e., the gate of a commercial MOSFET model CD4007UB. A Keithley 2636A (Keithley Instruments, Inc. OH, USA) dual-channel source meter was used for deriving the transistor characteristics. These characteristics were determined under stagnant-solution conditions using a conically tapered glass electrochemical mini cell (Scheme 2.2-1) filled with 1 mL of water. The gate coated with an MIP film was mounted parallel to the Pt-plate reference electrode. Distance between these electrodes was kept constant at ~10 mm (Scheme 2.3-14).

2.3 Techniques

The present section describes main characteristics of these aspects of experimental techniques, which were exploited in designing and preparing selective chemical sensors for oligonucleotides.

2.3.1 Isothermal titration calorimetry (ITC) and differential scanning calorimetry (DSC) techniques

Practically all physical, chemical, and biological processes are accompanied by heat effects. The amount of heat evolved or absorbed during these processes is quantitatively related to the extent of the process. Therefore, the technique consisting in heat measurement at constant temperature and pressure, namely ITC, found application in thermodynamic characteristics and determination of binding parameters of many systems. Because the heat signal is a nearly universal property of the complex formation or dissociation reactions, it is applicable to studies of most intermolecular interactions without a need for reporter labels. ITC is a non-destructive technique allowing for complete basic thermodynamic characterization of the system studied.

It is the only technique where the stability constant of the complex formed, K_s, as well as the change of binding enthalpy (ΔH), entropy (ΔS), and Gibbs free energy (ΔG) can directly and accurately be determined from a single experiment.[102] In this experiment, the heat released or absorbed is revealed as a peak corresponding to the power required to keep the sample and reference cells at identical temperatures (Scheme 2.3-1). The peak resulting from the injection is converted to heat output by integration, and then corrected for the cell volume and sample concentration. Therefore, ITC directly determines the individual heat, q, which is proportional to the enthalpy change associated with the studied process, ΔH,

$$q = V\,\Delta H\,\Delta[L_B] \qquad\qquad \text{(Equation 2.3-1)}$$

where V is the reaction volume and $[L_B]$ is the molar concentration of the ligand bound. The individual heat, q, is directly proportional to the increase of the amount of the bound ligand resulting from each injection. Therefore, its magnitude decreases as the fractional saturation of the system is titrated stepwise to reach completion. The total heat released, Q, is directly proportional to the total amount of the bound ligand, as

$$Q \; = \; V \, \Delta H \; \textstyle\sum \Delta[\mathrm{L_B}] = V \, \Delta H \; [\mathrm{L_B}] \qquad\qquad\qquad\text{(Equation 2.3-2)}$$
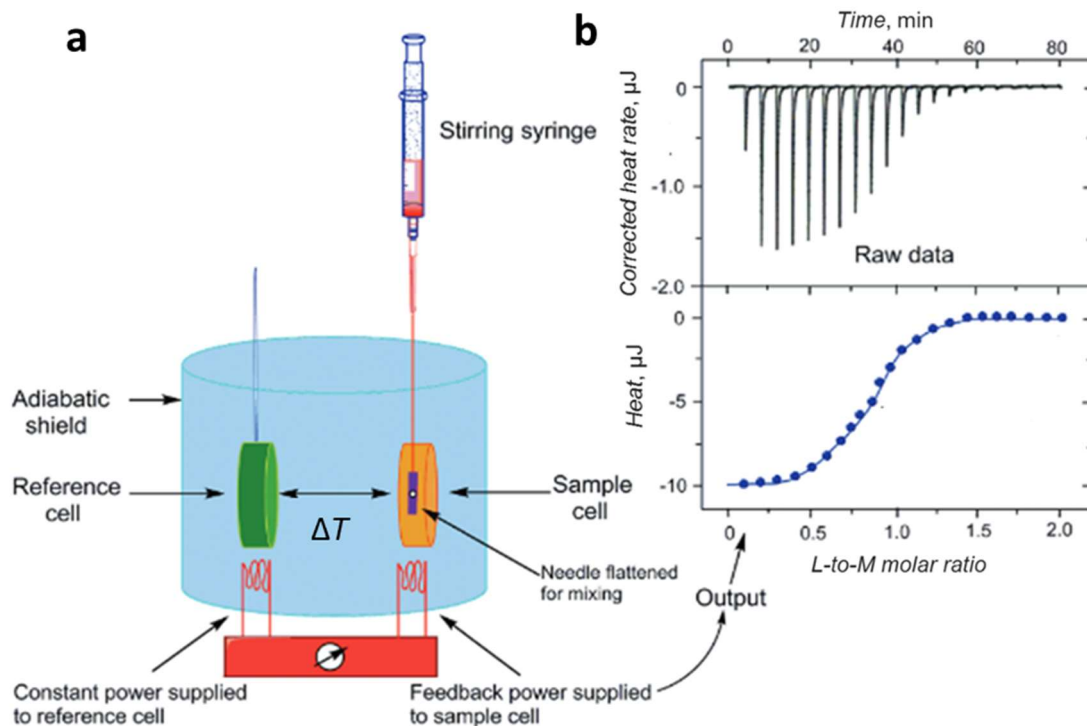
Scheme 2.3-1. (a) Schematic representation of a sample cell of isothermal titration calorimeter and (b) a titration thermogram representing heat released after each injection of the ligand, L, solution sample against time (top) and evaluation of the experimental heat data dependence on the ligand-to-macromolecule (L-to-M) ratio with the isotherm of the best fit (bottom).[103]

The successful determination of thermodynamic parameters relies on the subtraction of the dilution heat from the total heat released and the use of nonlinear least-square fit of an appropriate model that describes the interaction study. The simplest model applies to molecules with a single independent set of binding sites and with the only one complex stability constant. However, it is necessary to use alternative binding models in order to take into account complicated macromolecular interactions characterized by multiple binding sites and possible cooperativity between these sites. Accordingly, a macromolecule, M, has an arbitrary number of sets of interacting binding sites. For a system exhibiting multiple sets of independent binding sites, concentration of the ligand bound to each set is given by Equation 2.3-3

$$[\mathrm{L_{B},\mathit{i}}] \; = \; [\mathrm{M}] \, \frac{N_i K_i [\mathrm{L}]}{1 + K_i [\mathrm{L}]} \qquad\qquad\qquad\text{(Equation 2.3-3)}$$

where $[L_{B,i}]$ is the molar concentration of the ligand bound to binding sites of set i, $[M]$ is the molar concentration of the macromolecular compound available for the binding ligand, K_i is the complex stability constant for binding sites of set i on each macromolecule, N_i is the number of binding sites of set i of the macromolecule, and $[L]$ is the molar concentration of free ligand.

The total amount of heat released or absorbed as a result of ligand binding is given by the sum of the heats corresponding to each set, as

$$Q = V \sum_i \Delta H_i [L_{B,i}] = V[M] \sum_i \frac{N_i \Delta H_i K_i [L]}{1 + K_i[L]}$$

(Equation 2.3-4)

where ΔH is the enthalpy of binding to the binding sites of set i. The analysis of the ITC data is then performed by estimating the variable model parameters (N_i, K_i, and ΔH_i) by fitting either to the total heat, Q, or to the individual heat, q.

Similar in principle to ITC, differential scanning calorimetry is used to characterize thermally induced transition and decomposition processes. Because DSC is both very sensitive and non-perturbing, it has evolved as one of the most prominent technique for studying processes encountered in various compounds including proteins, nucleic acids, and carbohydrates/polysaccharides as well as determining melting points of polymers and biopolymers, glass transition temperature, specific heat capacity, and heat of phase transitions.[104] DSC characterizes the thermodynamic parameters controlling non-covalent interactions. Therefore, it is particularly suited for measuring thermal stability of nucleic acids or monitoring their conformational changes. By way of example, Scheme 2.3-2 shows the DSC thermograms for the PNA-DNA and DNA-DNA duplexes.[105] In these thermograms, there are peaks, which correspond to separation of the duplexes into single-stranded nucleic acid chains. This process is called "melting" and temperature, at which this transition occurs, is considered as melting temperature, T_m.

In a DSC experiment, the temperature of the identical sample and reference cells is increased linearly with time in the same pace while the temperature difference of both cells is kept at zero. The sample cell generally absorbs more heat than the reference cell, thus causing a slight temperature difference, $\Delta T = T_2 - T_1$, between these cells. A feedback loop monitoring temperature supplies a small amount of heat to the sample

cell, as to equalize the temperatures. This extra power, which is the instrumental signal of heat flow, is proportional to the differential heat capacity between the cells. A thermally induced transition or decomposition process accompanied by a heat effect generates a temperature difference, ΔT, between the cells. A thermal gradient is then compensated by supplying extra power and is manifested as a peak in the recorded thermogram. This compensation allows for a very precise temperature controlling, very accurate enthalpy and heat capacity measuring, and true isothermal performing.
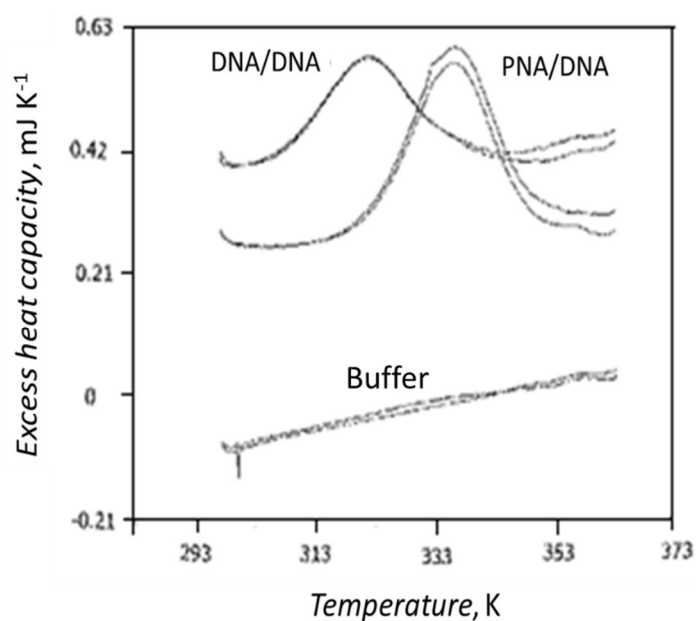
Scheme 2.3-2. The differential scanning calorimetry excess heat capacity versus temperature profiles for PNA-DNA and DNA-DNA duplexes as well as for 10 mM sodium phosphate buffer (pH = 7.0) solution, which was 100 mM in NaCl and 0.1 mM in EDTA.[105]

2.3.2 Cyclic voltammetry (CV)

Cyclic voltammetry is an electroanalytical technique most commonly used for studying heterogeneous oxidation and reduction mechanisms of both inorganic and organic compounds, their adsorption, and electrochemical reaction rates. In this technique, the current of the working electrode is recorded while its potential is linearly varried with time against a reference electrode at a scan rate of v from the initial, E_i, to the final, E_f value. At the end of its sweep, the direction of the potential scan is made opposite, usually stopping at the initial potential, thus resulting in a cyclic curve (Scheme 2.2-3a). This cycle can be repeated as many times as needed. The potential, at which its scan direction is turned back, is known as the switch potential.

The resultant trace of current plotted against potential applied is a cyclic voltammogram. In one CV cycle for a reversible electrode reaction (Scheme 2.2-3b), there are two peaks of similar shape in both the forward and backward sides of the cyclic voltammogram. These peaks are characterized by anodic, I_{pa}, and cathodic, I_{pc}, peak current as well as by their anodic, E_{pa}, and cathodic, E_{pc}, peak potential.
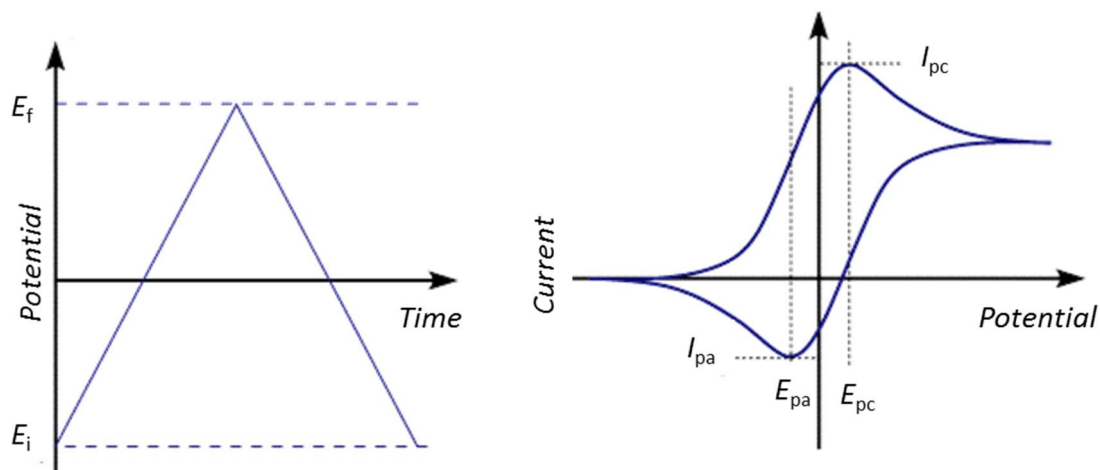
Scheme 2.3-3. (a) The cyclic voltammetry (CV) potential-time waveform. (b) Schematic cyclic voltammogram for a reversible redox couple, where E_{pa} and E_{pc} stand for the anodic and cathodic peak potential, respectively, while I_{pa} and I_{pc} for anodic and cathodic peak current, respectively.

The process is reversible when the rate of electron transfer across the electrode-(electrolyte solution) interface, k_{et}, is at each potential faster than the rate of analyte diffusion to and product diffusion from the electrode. Then, the diffusion rate limits the rate of the overall process. The potential obeys the Nernst equation as well as the anodic and cathodic peak separation is described by Equation 2.3-5.

$$\Delta E = E_{pa} - E_{pc} = 2.303 \frac{RT}{nF}$$
(Equation 2.3-5)

At 25 °C, this peak potential difference is 0.059 V/n, where n is the number of electrons transferred in the elementary electrode process.

Cathodic and anodic peaks are positioned on either side of the formal electrode potential, $E^{0'}$, of the analyte redox couple. The E_{pc} and E_{pa} potentials are independent of the scan rate, v, while I_p is proportional to $v^{1/2}$ (Equation 2.3-6 and Scheme 2.3-4a).

For a reversible redox couple, the peak current is described by the Randles-Ševčik dependence (Equation 2.3-6).[106]

$$I_{pa} = 2.72 \times 10^5 \, n^{2/3} \, D_{Red}^{1/2} A v^{1/2} \, c_{Red}$$ (Equation 2.3-6)

In this equation, A is the electrode surface area, D_{Red} is the diffusion coefficient of a reduced form of the redox species and c_{Red} is the bulk concentration of a reduced form of the redox species. Apparently, the peak current is directly proportional to the analyte concentration.
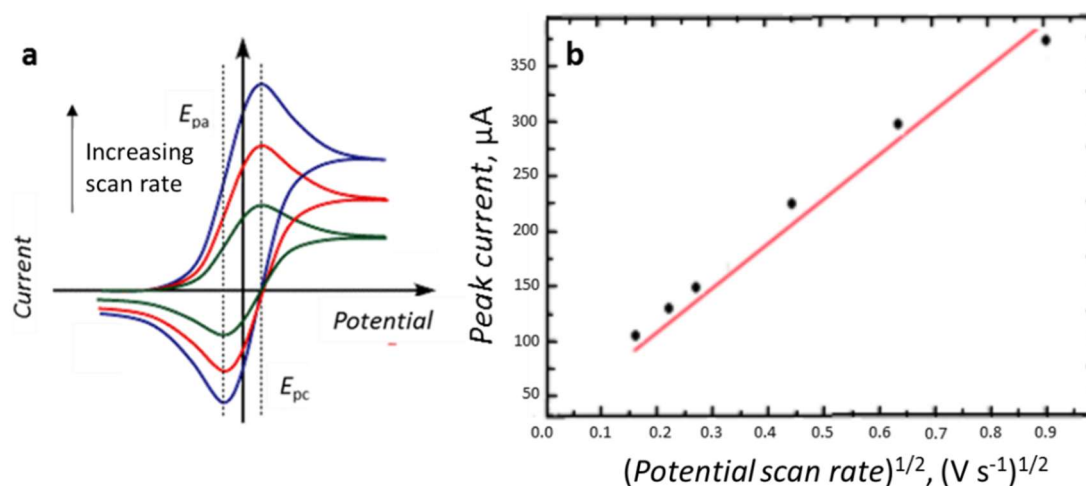
Scheme 2.3-4. (a) Cyclic voltammograms for different potential scan rates for a reversible redox process. (b) The Randles-Ševčik plot.

A plot of I_p against $v^{1/2}$ is often called the Randles-Ševčik plot (Scheme 2.3-4b). This plot is linear. From its slope, the analyte concentration can be determined if the diffusion coefficient is known. The Randles-Ševčik plot can be used to determine the D value if the concentration is known.

For a quasi-reversible process, the rate of the electrode process is close to the rate of diffusion. Then, the anodic and cathodic peak potential difference is higher than Equation 2.3-5 predicts. For an irreversible process, the anodic and cathodic peak separation is even higher or, in many cases, only one peak, i.e., either anodic or cathodic, is seen on the cyclic voltammogram. Primarily, the electrode process is irreversible, if its rate of charge transfer is lower than the rate of diffusion of the electroactive species to the electrode surface. Besides, a substrate may participate in a chemical reaction preceding the electrode process and a product of the electrode process can be the substrate of a following chemical reaction. Moreover, a substrate and/or a product can be adsorbed on the electrode surface or transferred to another phase. For

irreversible one-electron electro-oxidation, the peak of anodic current at 25 °C is described by Equation 2.3-7

$$I_{\text{pa}} = 2.99 \times 10^5 \alpha_a^{1/2} D_{\text{Red}}^{1/2} A \nu^{1/2} c_{\text{Red}} \qquad \text{(Equation 2.3-7)}$$

where α_a is the charge transfer coefficient of an anodic process.

2.3.3 Differential pulse voltammetry (DPV)

The analytical sensitivity of classical voltammetric techniques is usually quite high equaling $\sim 5 \times 10^{-5}$ mol dm^{-3}. At lower analyte concentrations, however, the charging currents, generated by electric double-layer effects or other non-faradaic processes, are comparable to faradaic currents, thus causing the accuracy to be unacceptably low. Therefore, pulse techniques were developed, among others, to improve the sensitivity of the measurements.

In DPV, a linear potential ramp is applied to the working electrode. Potential pulses of small constant amplitude in the range of 10 to 100 mV are superimposed on this ramp. The pulse duration, t_p, is selected from the range of 5 to 100 ms. The current is sampled twice per cycle. That is, first, the current is sampled just before the rise in potential, i.e., before the pulse application, and the second is sampled at the end of the potential pulse, i.e., just before the potential drops to the baseline. Because of this way of current measurement, capacity current is largely eliminated. The difference of the current sampled per cycle, ΔI, is nearly zero unless the analyte is reduced or oxidized at the working electrode. The magnitude of ΔI increases rapidly, if the potential is close to $E^{0'}$. Therefore, the differential pulse voltammogram plotted as the current difference against the potential scanned is peak shaped. For the reversible electrode process, the peak potential is given by Equation 2.3-8.

$$E_p = E^{0'} + \frac{RT}{nF}\ln\left(\frac{D_{\text{Red}}}{D_{\text{Ox}}}\right)^{\frac{1}{2}} - \frac{\Delta E_p}{2} \qquad \text{(Equation 2.3-8)}$$

where ΔE_p is the pulse amplitude. Potential of peak maximum, E_p, is close to $E^{0'}$ if $D_{\text{Red}} = D_{\text{Ox}}$ and ΔE_p is small.

The peak current, I_p, is proportional to the analyte concentration and pulse amplitude according to the Osteryoung-Parry equation[107]

$$I_p = \frac{nFA}{4RT} \left(\frac{D_{Red}}{\pi t_p}\right)^{1/2} c_{Red} \Delta E_p \qquad \text{(Equation 2.3-9)}$$

where t_p is the pulse duration.

The peak shape characterized with its width at half height, $W_{1/2}$, is an important parameter in quantitative DPV analysis of electrode processes. The $W_{1/2}$ value is dependent on the number of electrons transferred in the electrode process. For the reversible process, $W_{1/2} = 3.52$ RT/nF. At 25 °C, for processes with $n = 1$, 2, and 3, this peak width is, ~90, ~45, and ~30 mV, respectively. Besides, the higher the pulse amplitude, the wider the peak is. An increase of the peak width with the increase of a redox species concentration at a constant pulse amplitude evidences hindered diffusion of this species to the electrode surface.
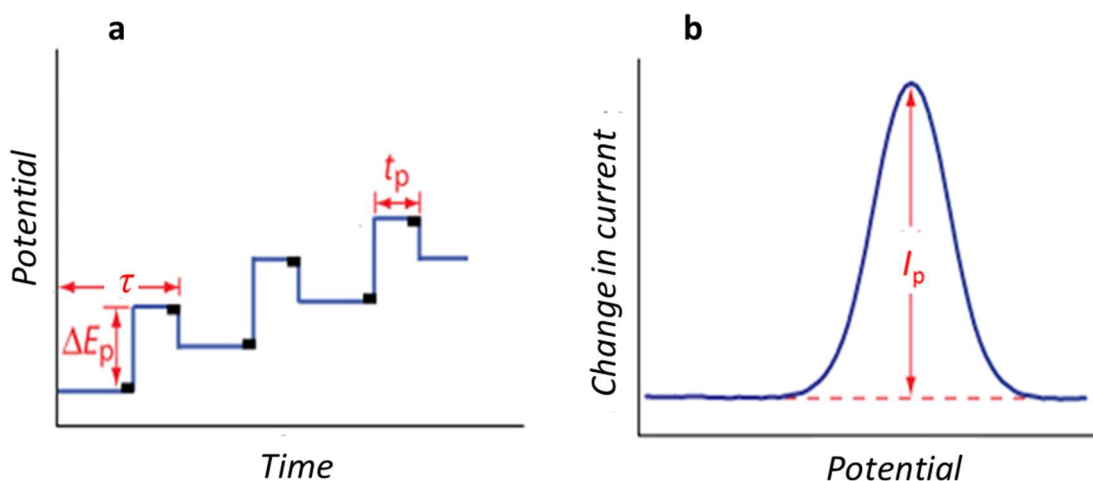
Scheme 2.3-5. (a) The time dependence of potential applied to the working electrode during the differential pulse voltammetry (DPV) measurement. (b) Peak-shaped differential pulse voltammogram. ΔE_p – potential pulse amplitude, t_p – potential pulse duration, τ – potential step duration.

With the DPV technique, many redox analytes can be determined in a single measurement because the peak for a given analyte is quite well separated from peaks of other analytes. Due to high sensitivity afforded by measurement of the difference of currents sampled, DPV allows determining analytes at concentrations as low as 10^{-8} M.
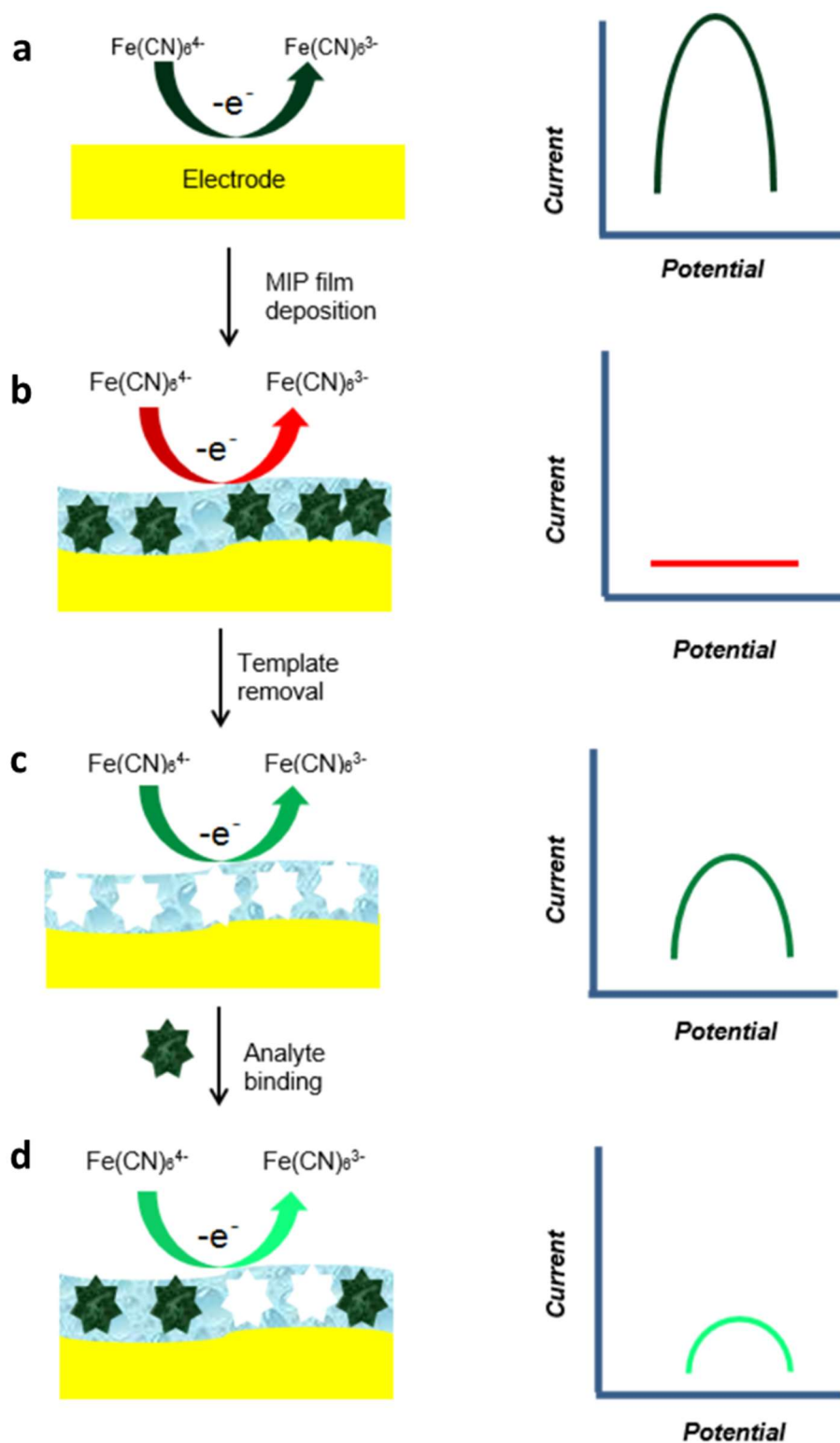
Scheme 2.3-6. The DPV manifested "gate effect". (a) Electrochemical oxidation of the $Fe(CN)_6^{4-}/Fe(CN)_6^{3-}$ redox marker on the uncoated electrode and the resulting well-defined DPV peak. (b) Hindering of the $Fe(CN)_6^{4-}/Fe(CN)_6^{3-}$ electrode process after MIP coating and the corresponding DPV response. (c) Enabled diffusion of the marker through the MIP film after template extraction resulting in a DPV peak. (d) Partially blocked diffusive permeability of the marker through the MIP film occupied by the analyte and the corresponding DPV peak of lower intensity.[108]

In MIP studies, the DPV techniques can be used for indirect evidencing of template imprinting, and then extracting from the MIP molecular cavities as well as for analyte determination by exploiting the so-called "gate effect" (Scheme 2.3-6).[108] The "gate effect" consists in the change in redox marker solute diffusive permeability through the MIP film resulting from interactions of recognizing sites of MIP imprinted cavities with the binding sites of the analyte. This effect is often used for signal transduction. Faradaic current of the redox marker at the MIP film coated electrode is sensitive to the presence of the analyte because analyte binding by the analyte-selective polymer changes the accessibility of the marker to the electrode.

2.3.4 Electrochemical impedance spectroscopy (EIS)

An ideal resistor obeys Ohm's law at all current and voltage levels and its resistance is independent of frequency. Then, the alternating voltage applied is in phase with the alternating current flowing through a resistor (Scheme 2.3-7a). However, most of real applications contain more complex electric circuit elements revealing a more complex behavior. These elements are characterized by impedance as a frequency dependent resistance to current flow. For measuring impedance, an alternating voltage of a fixed frequency and small amplitude, typically 10 mV, is applied to the working electrode. This voltage is described[109] by Equation 2.3-10

$$E(t) = E_0 \sin(\omega t) \hspace{4cm} \text{(Equation 2.3-10)}$$

where E_0 is the voltage amplitude, $\omega = 2\pi f$ is the angular frequency of the alternating voltage of frequency f applied, and t is time. Next, a signal of the current, shifted in phase by the phase angle, φ, (Scheme 2.3-7b), is described by Equation 2.3-11

$$I(t) = I_0 \sin(\omega t + \varphi) \hspace{3.5cm} \text{(Equation 2.3-11)}$$

where I_0 is the current amplitude, recorded while impedance is computed.
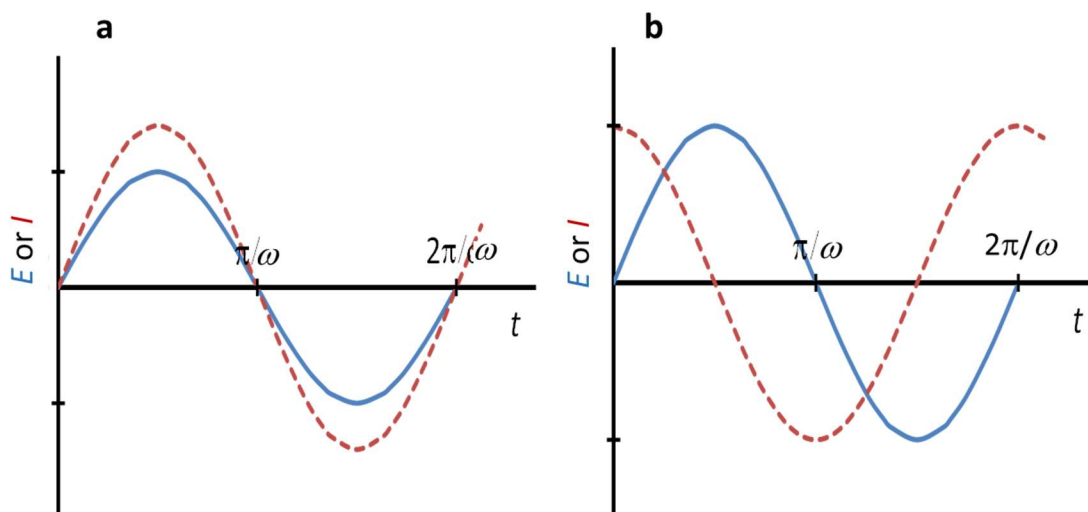
Scheme 2.3-7. Current changes incurred by sinusoidal voltage applied to an ideal (a) resistor and (b) capacitor.[110]

Subsequently, the measurement is repeated for a wide range of frequencies, and then the electrochemical impedance spectrum is constructed.

An expression analogous to Ohm's Law allows calculating the impedance of the system, Z, as

$$Z = \frac{E(t)}{I(t)} = \frac{E_0 \sin(\omega t)}{I_0 \sin(\omega t + \varphi)} = Z_0 \frac{\sin(\omega t)}{\sin(\omega t + \varphi)} \,. \qquad \text{(Equation 2.3-12)}$$

With the Eulers relationship,

$$\exp(j\sigma) = \cos\sigma + j\sin\sigma \qquad \text{(Equation 2.3-13)}$$

where σ is real number and j is imaginary unit, it is possible to express the impedance as a complex function. The potential is then described, as

$$E(t) = E_0 \exp(j\omega t) \qquad \text{(Equation 2.3-14)}$$

and the current response, as

$$I(t) = I_0 \exp(j\omega t - \sigma) \qquad \text{(Equation 2.3-15)}$$

55

The impedance is then represented as a complex number,

$$Z(\omega) = \frac{E}{I} = Z_0 \exp(j\sigma) = Z_0(\cos\sigma + j\sin\sigma) = Z_{real} - jZ_{im} \qquad \text{(Equation 2.3-16)}$$

where Z_{real} and Z_{im} is the real and imaginary component of impedance, respectively.

Impedance at a certain ω value in the coordinate system of $-Z_{im}$ against Z_{real} is called the Nyquist plot (Scheme 2.3-8a). Moreover, the EIS data may be presented as the Bode plot of log $|Z|$ versus log ω (Scheme 2.3-8b).

An electrochemical cell can be modeled as a network of passive electrical circuit elements, called an equivalent circuit, characterized by the same amplitude and phase angle as the real cell under a given potential excitation. Each element in the equivalent circuit should correspond to some defined activity in the electrochemical cell involving double-layer capacitance, C_{dl}, charge transfer resistance, R_{ct}, and electrolyte solution resistance, R_s.
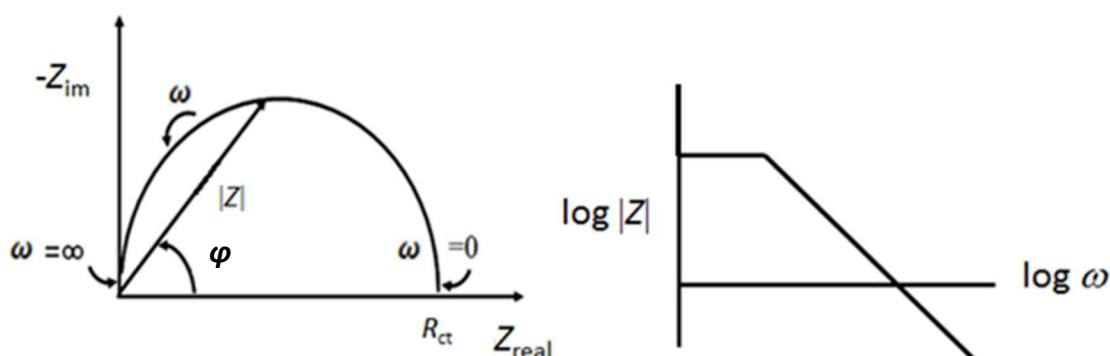
Scheme 2.3-8. Electrochemical impedance spectroscopy (EIS) data represented by (a) the Nyquist plot and (b) the Bode plot.[111] Z – impedance, Z_{real} and Z_{im} – real and imaginary, respectively, impedance components, ω – angular frequency, R_{ct} – charge transfer resistance, – phase angle.

Solution resistance is often calculated from EIS spectra. A modern three-electrode potentiostat compensates for the solution resistance between the counter and reference electrodes. However, any solution resistance between the reference electrode and the working electrode must be considered when modeling a cell. The resistance of an ionic solution depends on the ion concentration, type of ions, temperature, and the geometry of the area in which current is carried.

Another parameter measurable by EIS is an electrical double-layer capacitance, C. An electric double layer is formed in the interface between an electrode and its surrounding electrolyte solution. It originates from interactions of solution ions or dipoles with the electrode surface that result in charge separation between the two phases. This arrangement forms a capacitor. The ideal capacitor impedance, Z_C, is given by Equation 2.3-17.

$$Z_C = \frac{1}{j\omega C} = \frac{1}{j2\pi f C}$$ (Equation 2.3-17)

The rate of an electrochemical reaction depends on the reaction type, the temperature, the concentration of the reaction substrates and the potential. Hence, the movement of the electrons is restricted. This restriction is called charge transfer resistance, R_{ct}. This resistance is related to the exchange current density, J_0, by Equation 2.3-18.

$$R_{ct} = \frac{n\,F}{R\,T}\frac{1}{J_0}$$ (Equation 2.3-18)

For modeling an electrochemical system containing the working electrode coated with a porous polymer film, a modified Randles-Ershler equivalent circuit is often used (Scheme 2.3-9). In this circuit, the R_s element represents the solution resistance. The double-layer capacity, C_{dl}, is often replaced by the constant phase element, CPE, because polymer films rarely behave as an ideal capacitor characterized by zero real component.[112] Then, the CPE impedance, Z_{CPE}, is described by Equation 2.3-19

$$Z_{CPE} = \frac{1}{(i\,\omega)^\phi\,T}$$ (Equation 2.3-19)

where T is the frequency-independent proportionality factor. Its physical meaning is related to the diffusion coefficient. Symbol ϕ is an exponent, which can take values, $0 \leq \phi \leq 1$. For $\phi = 1$, the system behaves as an ideal capacitor where the Z_{CPE} equals to C^{-1} while for $\phi = 0$, Z_{CPE} equals to pure resistance.
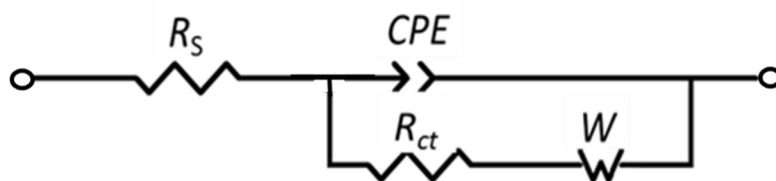
Scheme 2.3-9. A modified Randles-Ershler equivalent electric circuit of an electrochemical redox system used to fit experimental impedance data. R_S – solution resistance, R_{ct} – charge transfer resistance, W – Warburg impedance.

The Warburg impedance, W, introduced to the modified Randles-Ershler equivalent circuit (Scheme 2.3-9) represents a resistance to mass transfer, i.e., the diffusion control. The Warburg impedance typically exhibits a 45° phase shift. Contribution of this impedance to the total impedance is described by Equation 2.3-20

$$W = \frac{B \tanh(i\,T\,\omega)}{(i\,T\,\omega)^{\phi}} \qquad \text{(Equation 2.3-20)}$$

where B is the fitted parameter.

An equivalent circuit parameter, which corresponds to the system with the electrode coated with a polymer film, is R_{ct}. The value of this resistance depends on any surface changes that result in electrode blocking, e.g., by deposition of a less conducting film.

If only non-faradaic current flows, which is the case in the absence of a redox species, the imaginary component of impedance of the electrical double layer is inversely proportional to its capacitance, C_{dl}. If only the compact part of the double layer is considered, which is the case of solution with sufficiently high ionic strength where the Helmholtz model of the double layer holds, Equation 2.1-21 is used for C_{dl} determination

$$Z_{im} = \frac{1}{\omega\,A\,C_{dl}} \qquad \text{(Equation 2.3-21)}$$

where A stands for the electrode surface area.

The determined C_{dl} changes proportionally to the changes of capacitance of the compact part of the double layer, thus solely depending on the change of solution electric permittivity, ε, and the double-layer thickness, d_{dl}, according to Equation 2.3-22

58

$$C_{\mathrm{dl}} = \frac{\varepsilon\,\varepsilon_0}{d_{\mathrm{dl}}} \qquad\qquad\qquad \text{(Equation 2.3-22)}$$

where ε_0 is permittivity of free space.

The equivalent circuit of the polymer film coated electrode in a supporting electrolyte solution is composed of a solution resistor in series with an electrical double-layer capacitor (Scheme 2.3-10).
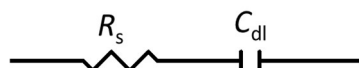
Scheme 2.3-10. The equivalent circuit of a cell with a non-faradaic electrochemical process for the polymer-coated electrode immersed in a supporting electrolyte solution.

2.3.5 Piezoelectric microgravimetry (PM) at a quartz crystal microbalance (QCM)

Piezoelectric microgravimetry is an acoustic shear mode bulk wave technique used for measuring small changes of mass of a thin film deposited on surface of the electrode of the AT-cut QCR. For that, it utilizes a converse piezoelectric effect. In this effect, piezoelectric crystal mechanically oscillates at resonance frequency proportional to its thickness,[113] if alternating voltage is applied to both its sides. If the QCR is loaded with mass, oscillation frequency is decreased. From this decrease, the mass change can be calculated according to the Sauerbrey relation, Equation 2.3-23,

$$\Delta f_{\mathrm{mass}} = -\frac{2\,f_0^2\,\Delta m}{A_{\mathrm{acoust}}\,(\mu_{\mathrm{q}}\,\rho_{\mathrm{q}})^{1/2}} \qquad\qquad \text{(Equation 2.3-23)}$$

where f_0 is the fundamental resonance frequency of the resonator, A_{acoust} is the acoustically active area of the resonator, μ_{q} is the shear modulus of quartz, and ρ_{q} is the quartz density.

The Sauerbrey equation is applicable when several assumptions are fulfilled. An important one refers to the rigidity of the deposited film, which should not exhibit visco-elastic properties ($\Delta f_{\mathrm{vis}} \approx 0$). If the resonator is contacted with a liquid, then the total resonance frequency change includes visco-elastic changes of the surrounding, i.e., dynamic viscosity, η_{L}, and density, ρ_{L}, of the liquid. Then, the resonance frequency change is described by Equation 2.3-24.[113]

$$\Delta f_{\text{mass}} = -\left[\frac{2 f_0^2}{(\mu_q \rho_q)^{1/2}}\right]\left[\frac{\Delta m}{A_{\text{acoust}}} + \left(\frac{\mu_L \rho_L}{4 \pi f_0}\right)^{1/2}\right] \qquad \text{(Equation 2.3-24)}$$

This formalism has been extended to resonators coated with viscous films. In this case, contribution of the frequency change corresponding to the change of viscosity of the film is

$$\Delta f = -f_0^{3/2}\left(\frac{\mu_q \rho_q}{\pi \mu_q \rho_q}\right)^{1/2} \qquad \text{(Equation 2.3-25)}$$

This change can indirectly be measured by the dynamic resistance, R_D,

$$R_D = \frac{A_{\text{acoust}}}{k_{\text{QCR}}^2}(2 \pi f_0 \mu_L \rho_L)^{1/2} \qquad \text{(Equation 2.3-26)}$$

where $k_{\text{QCR}}^2 = 7.74 \times 10^{-3} A^2 \text{ s m}^{-2}$ is the electromechanical coupling factor of QCR. From Equations 2.3-26 and 2.3-26, a relation between the frequency change and R_D can be derived, as

$$\Delta f = \frac{k_{\text{QCR}}^2 R_D f_0}{\pi A_{\text{acoust}} \left(2 \mu_q \rho_q\right)^{1/2}} \qquad \text{(Equation 2.3-27)}$$

Therefore, the mass change can be calculated from the simultaneously recorded resonance frequency and dynamic resistance change.

The complexation of a macromolecular compound, M, by a ligand, L, in the MIP molecular cavity can be studied by PM performed under FIA conditions.[114] In the following reaction

$$\text{M} + \text{L} \underset{k_d}{\overset{k_a}{\rightleftarrows}} \text{ML} \qquad \text{(Equation 2.3-28)}$$

k_a is the second-order association rate constant for binding of an analyte molecule in the unoccupied MIP cavity, which results in the formation of the complex, ML. This complex dissociation rate is described by the first-order rate constant, k_d. The

equilibrium constant of the reaction, i.e., the complex stability constant, K_s is given by the ratio of the association and dissociation rate constants, $K_s = k_a/k_d$.

The rate of complex formation can be determined[114] from changes of the resonance frequency with time, df/dt, and the concentration of the injected macromolecular compound, c_M^X,

$$\frac{dc_{ML}}{dt} = -\frac{df}{dt} = k_a\, c_M^X (f_{max} - f) - k_d\, f \qquad \text{(Equation 2.3-29)}$$

where f_{max} represents the maximum frequency reached after saturation with M molecules of all recognizing sites of the MIP cavities.

After integration, and then introduction of the equilibrium frequency, f_{eq}, in the extreme of the function and the rate constant of the reaction, k_{exp}, the dependence of the resonance frequency, f, on time, t, can be fitted to the kinetic Equation 2.3-20.

$$f = \frac{k_a\, c_M^X\, f_{max}}{k_a\, c_M^X + k_d} \{1 - \exp[-(k_a\, c_M^X + k_d)t]\} = f_{eq}[1 - \exp(-k_{exp}\, t)] \quad \text{(Equation 2.3-30)}$$

In this way, the ML association curves can directly be applied for calculation of parameters using non-linear regression. The plot of k_{exp} against the c_M^X provides values of the association and dissociation rate constants. From its slope and intercept with the ordinate, k_a and k_d respectively, can be determined, according to Equation 2.3-31.

$$k_{exp} = k_a\, c_M^X + k_d \qquad \text{(Equation 2.3-31)}$$

2.3.6 Surface plasmon resonance (SPR) spectroscopy

Surface plasmons are coherently delocalized electron oscillations generated at the interface of two media with electric permittivity values of opposite signs, e.g., a metal and a dielectric. Their motion wave is associated with an electromagnetic wave, the field vectors of which they reach their maxima at the interface and decay evanescently into both media. This surface plasma wave (SPW) is a transverse magnetic polarized wave, which means that magnetic vector is perpendicular to the direction of propagation of the surface plasmon wave and parallel to the plane of interface. The propagation

constant, β, of SPW propagating at the interface between a semi-infinite dielectric and a metal is given by Equation 2.3-32

$$\beta = k' \sqrt{\frac{\varepsilon_m\, n_s^2}{\varepsilon_m + n_s^2}}$$ (Equation 2.3-32)

where k' denotes the free-space wavenumber, ε_m is the electric permittivity of the metal, and n_s is the refractive index of the dielectric. As it follows from Equation 2.3-32, the SPW may be supported by the metal, provided that $\varepsilon_m > -n_s^2$. At optical wavelengths, this condition is fulfilled, among others, by the most commonly used gold and silver.[115]

The surface plasmon resonance (SPR) is a phenomenon, which is observed as a drop of intensity of polarized light reflected from the metal surface under certain conditions. These include angle of incidence and wavelength of the light beam as well as the measurement setup. Photons of p-polarized light can then interact with the free electrons of the metal layer, thus inducing wave-like oscillations of free electrons and, therefore, decreasing the reflected light intensity. This phenomenon occurs if the angular frequency and phase velocity of the incident light beam are comparable to those of the surface plasmons.[116] As it follows from Equation 2.3-32, the β propagation constant of SPW is always different than that of optical wave propagation constant in the dielectric. Therefore, the SPW at a planar metal-dielectric interface can be excited only by the enhanced incident optical wave. The photons momentum change is commonly achieved using attenuated total reflection (ATR) in prism couplers and optical waveguides, and diffraction at the surface of diffraction gratings (Scheme 2.3-11).

In the ATR coupler, the incident light is passed through a dielectric medium prism, which is usually glass or quartz. This medium, of refractive index exceeding 1, decreases the phase velocity of photons. Then, the incident light matches that of the surface plasmons and resonance occurs. Direct contact of surface plasmons with the environment in the ATR setup with the Kretschmann configuration makes it applicable for sensing (Scheme 2.3-11a).[117]

The drop in the intensity of the reflected light at a certain wavelength (Scheme 2.3-11b) results from resonance transfer of energy into the SPW. Owing to the strong electromagnetic field density in the dielectric, the propagation constant of the SPW, and consequently the SPR condition, is very sensitive to any changes in the

optical properties of the dielectric adjacent to the metal surface. Therefore, any variations in the structure of the polymer film deposited on the metal surface can be measured.

Real-time SPR measurement provides kinetic data of the analyte-(MIP cavity) interaction. The SPR study allows determining complex association and dissociation rate constant, k_a and k_d,[118] respectively, similarly to those obtained by piezoelectric microgravimetry.
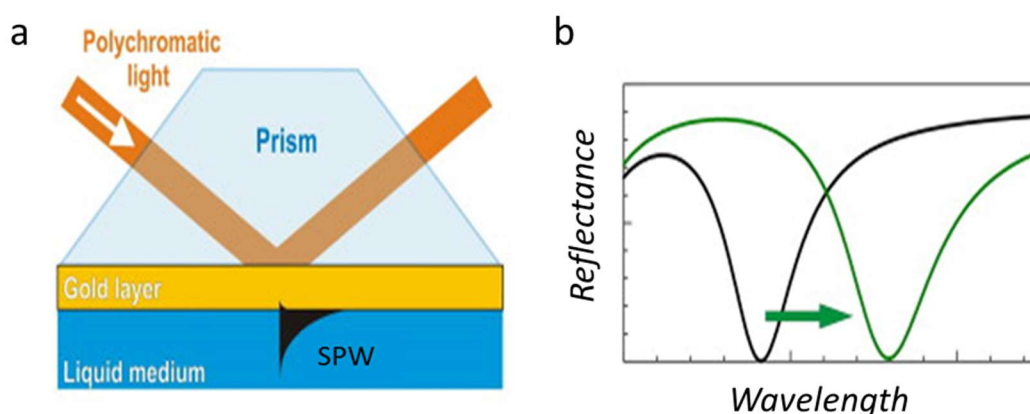
Scheme 2.3-11. (a) Excitation of the surface plasma wave (SPW) by polychromatic light in the Kretschmann configuration of the attenuated total reflection (ATR) method. (b) Exemplary spectrum of reflected light with characteristic SPR signal drops for two different values of the refractive index at the gold layer.[117]

The concentration change with time of the bound ligand can be expressed as

$$\frac{d[\text{L}_\text{B}]}{dt} = k_a \, c_\text{M} \, [\text{L}] - k_d \, [\text{L}_\text{B}] \qquad \text{(Equation 2.3-33)}$$

where c_M is the concentration of the analyte in the proximity of the sensor surface, $[\text{L}]$ and $[\text{L}_\text{B}]$ is the molar concentration of free and bound ligand, respectively, and t is time. The SPR response, R, is directly proportional to the complex concentration, $[\text{ML}]$. Moreover, the free ligand concentration can be expressed as $(R_{max} - R)$ if the maximum SPR signal, R_{max}, is known. Then, Equation 2.3-33 can be rewritten, as

$$\frac{d[\text{ML}]}{dt} = k_a \, c_\text{M} \, (R_{max} - R) - k_d \, R \qquad \text{(Equation 2.3-34)}$$

After integration, Equation 2.3-34 takes the form

63

$$R = R_{\text{eq}} \left[1 - e^{-(k_{\text{a}} \, c_{\text{M}} + k_{\text{d}}) \, t} \right] \qquad \text{(Equation 2.3-35)}$$

where R_{eq} is an equilibrium SPR signal in the function extreme. Next, a theoretical curve is fitted to the experimental signal change with time, and then k_{a} and k_{d} rate constants as well as K_{s} are determined from fitting parameters of this curve.

From R_{eq}, it is possible to calculate the equilibrium surface concentration of the bound macromolecular compound for each injection. This concentration is equal to the equilibrium concentration of the bound ligand, $[L_B]_{\text{eq}}$. Then, the equilibrium concentration of free ligand, $[L]_{\text{eq}}$, can be calculated using Equation 2.3-36,

$$k_{\text{a}} \, c_{\text{M}} \, [L]_{\text{eq}} = k_{\text{d}} \, [L_B]_{\text{eq}} \qquad \text{(Equation 2.3-36)}$$

and the total ligand concentration, c_{L_0}, in the MIP can be calculated according to Equation 2.3-37.

$$c_{L_0} = [L]_{\text{eq}} + [L_B]_{\text{eq}} \qquad \text{(Equation 2.3-37)}$$

The ML complex formation is characterized by the complex formation (hybridization) efficiency, x_{ef}, determined from the ratio of the concentration of the bound ligand in equilibrium, $[L_B]_{\text{eq}}$, to the total ligand concentration, c_{L_0}, as described by Equation 2.3-38.

$$x_{\text{ef}} = \frac{[L_B]_{\text{eq}}}{c_{L_0}} \qquad \text{(Equation 2.3-38)}$$

2.3.7 Atomic force microscopy (AFM)

Atomic force microscopy (AFM) is a powerful microscopy technique for imaging samples at atomic resolution with height information of angstrom-scale resolution. An AFM uses a vertically vibrating flexible cantilever with a very sharp tip to scan over a sample surface. For scanning, an AFM scanner, made of a piezoelectric material, expands and contracts proportionally to the applied voltage in the x, y, and z directions.[119] The studied sample, mounted on a piezoelectric scanner, moves against

scanning surface with accuracy of 0.01 nm. As the tip approaches the surface, the close-range force between the surface and the tip causes cantilever deflection. This deflection can be measured by shining a laser beam on top of the cantilever. Slight changes in the direction of the reflected beam, resulting from any cantilever deflection, are then converted into an electric signal with a photodetector. Controlling the distance between the tip and sample surface from the electric signals allows for imaging the sample and determining its topography (Scheme 2.3-12.).
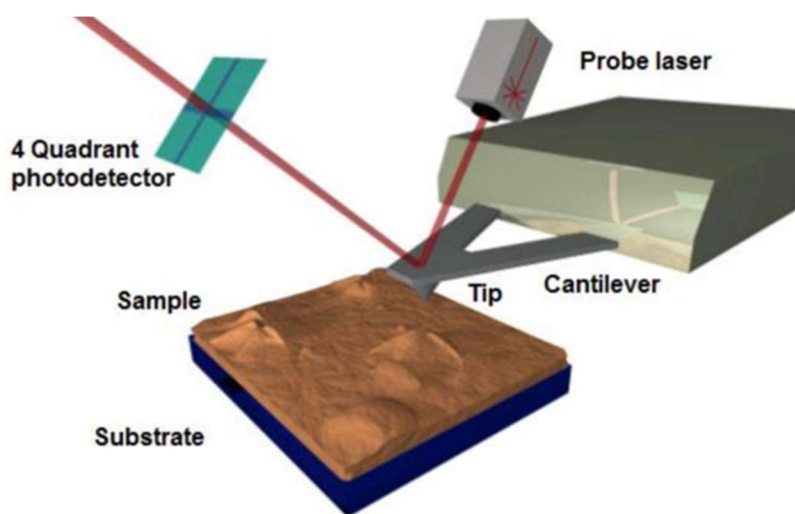
Scheme 2.3-12. A sketch of the atomic force microscopy (AFM) setup for determining sample topography.[120]

Properties of the sample surface decide on selection of the scanning mode. Common AFM modes include the contact, semi-contact, and non-contact mode. There are two methods of imaging in the contact mode, namely the constant force mode and the constant height mode. In the former, the force between the tip and the sample is continuously adjusted to maintain a specified deflection. When the tip scans in the constant height mode, the sample must be relatively flat for the feedback loop to keep control during scanning. This option is particularly suitable for small, high-speed atomic resolution scans. In a semi-contact mode or tapping mode, the tip periodically touches the surface of the sample because the cantilever oscillates near its resonance frequency. This oscillation is damped by tip interaction with the sample. To keep the oscillation amplitude constant, the instrument adjusts the tip position. In a non-contact AFM mode, the tip oscillates near the sample surface at a frequency slightly higher than the resonance frequency of the cantilever. Changes in the amplitude, phase, and

65

frequency of the oscillation are measured in order to construct the topography of the sample surface.

Moreover, AFM provides means for determination of thickness of films, which coat conducting substrates. For that, a part of the film is removed from the surface using e.g., a Teflon^{TM} spatula. Then, height of a step formed, that is film thickness, is determined (see, Section 2.2.8, above).

2.3.8 Polarization-modulation infrared reflection-absorption spectroscopy (PM-IRRAS)

Polarization-modulation infrared reflection-absorption spectroscopy (PM-IRRAS) is a highly sensitive surface specific technique used for characterization of orientation of molecules in thin films including monolayers deposited on refractive substrates. The advantage of PM-IRRAS over the conventional IRRAS is that modulated reflectivity is not affected by the isotropic adsorption of gas or bulk water. Consequently, the interfering effect caused by the water vapor and carbon oxide can be eliminated.

The PM-IRRAS allows measuring surface-specific FT-IR spectra of materials because of differences in p- and s-polarized light reflection from interfaces. An IR beam is resolved into p- and s-polarized components, in which the electric vector oscillation is parallel and perpendicular to the plane of incidence, respectively. In case the p- or s- component is incident on a metal surface, a stationary wave results from the interference between incident and reflected beams. The electric field amplitude of the stationary wave from p-polarized beam sharply increases at a high angle of incidence. On the other hand, the amplitude of s-polarized light beam is insignificant at all angles. Therefore, a signal from species present on a metal surface can be obtained with the grazing incidence of p-polarized light.

2.3.9 X-ray photoelectron spectroscopy (XPS)

X-ray photoelectron spectroscopy (XPS) is a widely used surface analysis technique providing chemical qualitative and quantitative information about the surface of a broad range of materials. The sample surface is scanned by the micro focused x-ray beam, which allows acquiring of spatial distribution information. Typically, an XPS experiment is accomplished by exciting a sample surface with mono-energetic Al Kα X-rays causing emission of photoelectrons from the sample surface (Scheme 2.3-13).

Energy of these photoelectrons is measured by an electron energy analyzer. Then, from the characteristics of a photoelectron peak, i.e., its binding energy, *BE*, and intensity, the elemental identity, chemical state, and relative quantity of a detected element can be determined. The XPS detects only those electrons, which, after escaping from the sample into the vacuum of the instrument, reached the detector. Thus, the signal from analytes present on the surface is much stronger than those from analytes residing deeper in the sample.

The average depth of XPS analysis is ~5 nm. To obtain subsurface information of the sample, ion beam is used for etching layers of the sample, i.e., for depth profiling. For that, first, a spectrum, or set of spectra is recorded from the sample surface. Then, an ion beam, which is scanned over a square or rectangular area of the sample, etches sample surface. After the etch cycle, the ion beam is blanked and another set of spectra is recorded. This sequence of etching and spectrum recording is repeated after reaching the required depth.
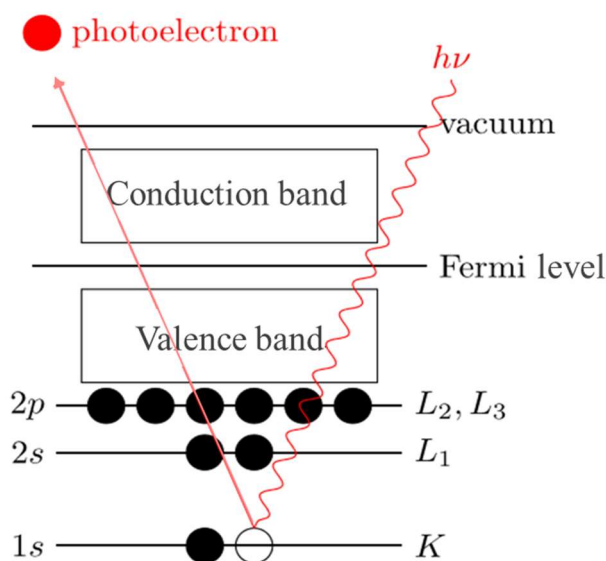

Scheme 2.3-13. The principle of photoelectron emission.

2.3.10 Extended-gate field-effect transistor (EG-FET) sensing

The field-effect transistor (FET) is a transistor, which uses an electric field to regulate the electrical properties of the device. It consists of an active channel through which charge carriers, i.e., electrons or holes, flow from the source (S) to the drain (D). The third terminal is the gate (G), which modulates the channel conductivity.

The MIP or NIP film coated gold electrodes of Au-glass slides (see Section 2.2.4, above) can be considered as simple extensions of the classical FET gates (Scheme 2.3-14). Therefore, any change in potential at the Au-glass slide, occurring on the gate itself, leads to the change of the source-drain current. In order to open or close the gate, certain voltage should be applied across the Au-glass/polymer/solution interfaces. To achieve that, the additional electrode, immersed in the test solution, is polarized by using a source meter. At a constant applied gate voltage, V_G, the drain voltage, V_D, is varied and the resulting drain current, I_D, is measured. If the analyte interacts with the MIP film, the effective gate voltage is changed, which leads to the current change. This current is proportional to the amount of the analyte bound in the MIP film, thus being used as the analytical signal.
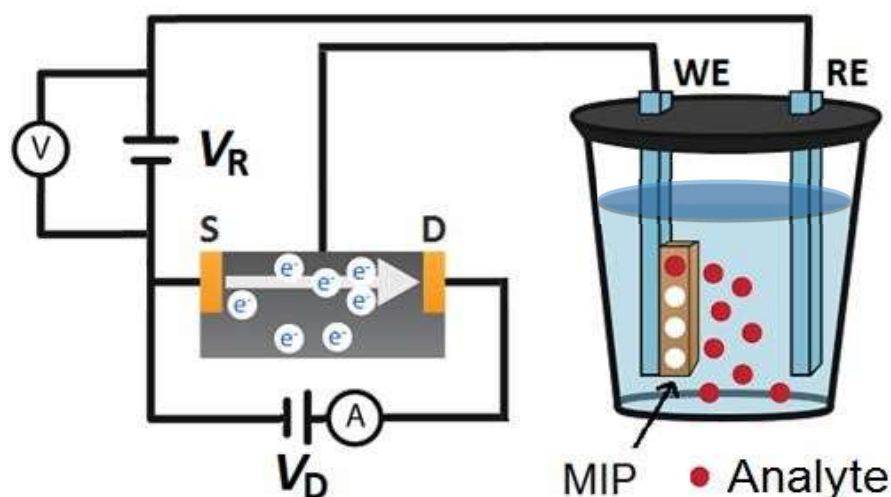
Scheme 2.3-14. Experimental setup for FET measurements with Au-glass slide coated with MIP film as the gate and a Pt plate as the reference electrode. **S** and **D** are drain and source components of the FET structure.

Chapter 3

Results and discussion

This section describes calculations and experiments that were designed and performed for preparing MIP chemical sensors selective to 5'-TATAAA-3' and 5'-GCGGCGGC-3' oligonucleotides.

## 3.1 Chemical sensor for selective 5'-TATAAA-3' determination

The present section focuses on devising, characterizing, and fabricating an MIP chemosensor for selective 5'-TATAAA-3' determination.

3.1.1 Quantum chemical modeling of the pre-polymerization complex of TATA with functional monomers 10 and 11

Formation of stable A-T nucleobase pairs of functional monomers with the 5'-TATAAA-3' template in the pre-polymerization complex solution was predicted by computational modeling.

However, an accurate ab initio optimization of the 568-atom complex of one 5'-TATAAA-3' template molecule with two A **10** and four T **11** functional monomer molecules appeared to be prohibitively time consuming in the case of the present study, even with the resolution-of-identity (RI) approximation[121] adopted. Therefore, the complexation of a shorter fragment of the template, namely TATA, with functional monomers A **10** and T **11** was molecularly modeled at the B3LYP approximation level with the 3-21G basis set (Scheme 3.1-1a). The negative Gibbs energy gain as high as ΔG = -256.6 kJ/mol was calculated using the DFT method augmented with the D3 empirical dispersion correction.[122-125] Although this value, calculated per one hydrogen bond, was higher than that for typical nucleobase pairing interactions, these calculation results still seem to be qualitatively correct and should not change significantly even at a higher level of the theory. This relatively high negative ΔG value clearly indicated an energetic preference of formation of a complex of TATA with the A and T moieties of the functional monomers **10** and **11** respectively, each paired with the complementary T and A moiety, respectively, of the TATA (Scheme 3.1-1b). Apparently,

the 5'-TATAAA-3' recognition by functional monomers mimicked that of nucleic acids in living organisms.

a

b
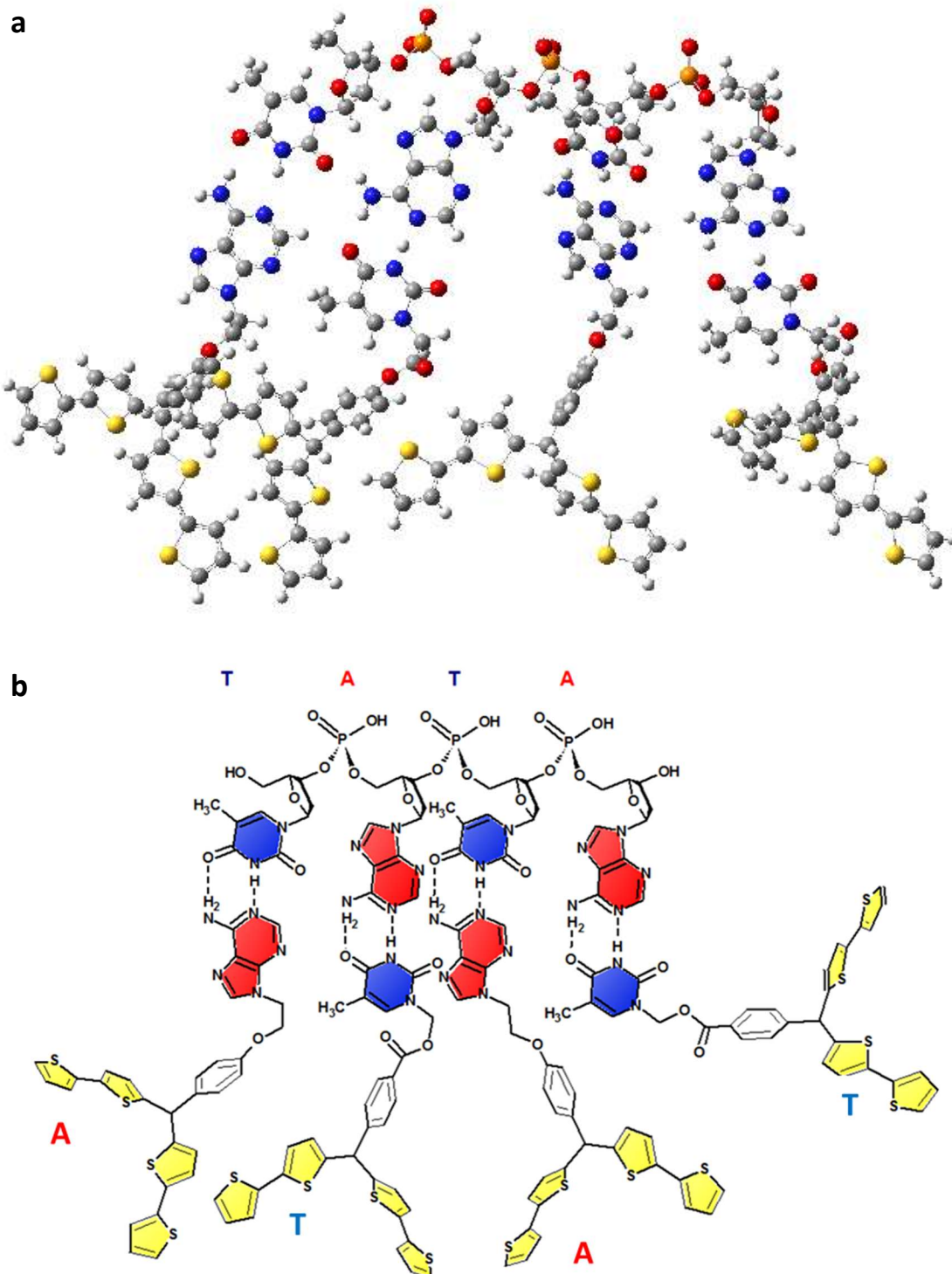
Scheme 3.1-1. (a) The B3LYP/3-21(*) optimized structure of the complex of the TATA molecule with two A **10** and two T **11** molecules of functional monomers, and (b) the structural formula of this complex.

3.1.2 Experimental confirmation of adenine-thymine nucleobase pairing in the pre-polymerization complex

For experimental confirmation of the A-T nucleobase pairing between the recognizing moieties of functional monomers **10** and **11** (Table 2.1-3) and the binding nucleobase moieties of the template, in solution, ITC experiments were performed (Figure 3.1-1). However, solubility of the **10** and **11** functional monomers as well as 5'-TATAAA-3' **1** (Table 2.1-1) or corresponding PNA $H_2N(CO)TATAAA-NH_2$ **6** (Table 2.1-2) in the solution for electropolymerization was insufficient to reach the concentrations required for the titration. Therefore, DMSO was used instead because solubility of both the titrant and the analyte in this solvent was sufficiently high. Moreover, stability of PNA, in contrast to stability of DNA, is almost unaffected after dissolution in an organic solvent.[126] Nevertheless, PNA has to be pre-organized to assume binding conformation before complexation for successful use of the imprinting strategy, i.e., to ensure high affinity and selectivity of binding the functional monomers and the PNA template. In their non-hybridized (single-stranded) forms, DNA and RNA can adopt helical structures through nucleobase stacking (although highly flexible). In contrast, PNA does not exhibit well-defined conformational folding in solution.[127] This is because PNA is a neutral DNA analogue where the negatively charged phosphodiester backbone of DNA is replaced by that of an achiral 2-amino-ethyl-glycine (AEG).[1] Moreover, PNA oligomers form very stable duplexes with complementary target nucleic acids via Watson-Crick nucleobase pairing. This pairing between PNA $H_2N(CO)TATAAA-NH_2$ **6** and A **10** or T **11** nucleobase-substituted 2,2'-bithien-5-yl functional monomers was confirmed experimentally.

For that, PNA $H_2N(CO)TATAAA-NH_2$ **6** and the A functional monomer **10** were dissolved in DMSO to reach the concentration of 125 μM and 2.5 mM, respectively. Injection of the 8-μL sample of 2.5 mM titrant resulted in heat release, ΔH, whose amount changed with formation of the complex. The total ΔH was obtained by subtracting the dilution heat of titrant **10** from the total heat corresponding to injections of the solution of this titrant to the solution of PNA. An independent model was chosen and a theoretical isotherm was fitted to the ITC data acquired (Figure 3.1-1) yielding the change of binding enthalpy ($\Delta H = -19.0$ kJ), the complex stability constant ($K_s = 1.65 \times 10^5$ M^{-1}), and the expected complex stoichiometry (**10** : PNA = 2 : 1).
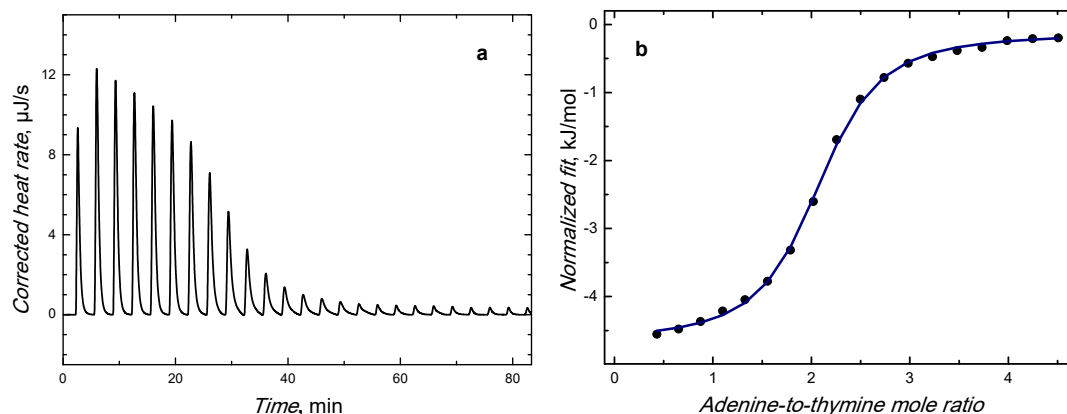
Figure 3.1-1. (a) The curve of isothermal titration calorimetry for the 2.5 µM adenine functional monomer **1** with 8-µL samples of 125 µM PNA H$_2$N(CO)TATAAA-NH$_2$ added at 3-min time intervals. (b) The least-square fit of the curve of an independent model to the data points acquired.

From these values, the Gibbs free energy change (ΔG = -29.5 kJ/mol) and the entropy change (ΔS = 35.7 J mol^{-1} K^{-1}) accompanying complex formation were calculated. Apparently, the complex of one PNA H$_2$N(CO)TATAAA-NH$_2$ **6** molecule with two A **10** functional monomer molecules was stable.

Stability of the complex of PNA H$_2$N(CO)TATAAA-NH$_2$ with two functional monomers **10** and **11** was confirmed by the DSC measurement. In the resulting thermogram (Figure 3.1-2), there was a peak at 63.9 °C indicating complex dissociation at this temperature.
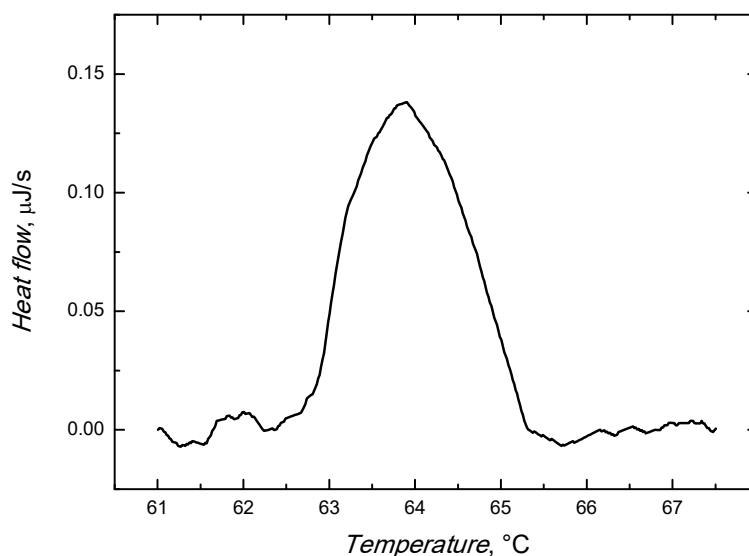
Figure 3.1-2. The differential scanning calorimetry curve for the complex of PNA H$_2$N(CO)TATAAA-NH$_2$ with **1** and **2**. The melting temperature was 63.9 °C.

72

Therefore, the pre-polymerization complex of PNA $H_2N(CO)TATAAA-NH_2$ with complementarily aligned 2,2'-bithien-5-yl functional monomers **10** and **11** was very stable. In analogy to the melting property of double-stranded DNA, the temperature of 63.9 °C can be considered as the melting temperature, T_m, of the pre-polymerization complex corresponding to dissociation of the double helix into single strands, i.e., one of PNA $H_2N(CO)TATAAA-NH_2$ and the other of functional monomers. Apparently, functional monomers enforced conformational stability of the PNA $H_2N(CO)TATAAA-NH_2$ and provided the size and hydrogen bonding complementarity for effective formation of the stable complex. Besides, this T_m is higher than that of the corresponding 5'-TATAAA-3' (Table 3.1-1). Apparently, the **10** and **11** functional monomers, used as artificial nucleotides, carry sequence information of the ODN at the molecular level. Therefore, A **10** and T **11** nucleobase-substituted 2,2'-bithien-5-yl functional monomers can be used as non-biological nucleotide counterparts.

Table 3.1-1. Melting temperature, T_m, values of different oligonucleotides (ODNs).

Probe	Target	Melting temperature, T_m, °C
2,2'-Bithien-5-yl ODN analogue	5'-TATAAA-3'	63.9
LNA ATGGTG[128]	probe-complementary ODN	43.0
LNA TAATTTTA[128]	probe-complementary ODN	10.0
PNA GCATTTGCAT[129]	probe-complementary ODN	39.6
PNA GCATGAGCAT[129]	probe-complementary ODN	38.8 - 66.5

3.1.3 Preparation of the (5'-TATAAA-3')-templated and (PNA $H_2N(CO)TATAAA-NH_2$)-templated MIP films by programmed transfer of sequence information

Polymers molecularly imprinted with ONs, described in the present thesis, can be considered as examples of nucleobase-containing polymers described in Section 1.1.4, above, as DNA analogues. Sequence information of these analogues is programmed by

the use of a template, along which monomers arrange in the predetermined order through hydrogen bonding, and then polymerizing.

Because of hydrogen bonding, MIP formation in aprotic organic solvent solutions is more effective than in aqueous solutions.[87] This is because molecules of such a solvent do not compete with proton acceptors for protons. To date, most of MIP syntheses involving non-covalent template binding were performed using aprotic organic solvent solutions. This was accomplished in order to avoid water competition for hydrogen bonding, which is operative in formation of the pre-polymerization complex. Contribution of this bonding is higher the lower is electric permittivity of the solvent used. Therefore, derivatives of all five nucleobases soluble in an organic solvent were used as templates.[88] Among them, MIPs prepared using genuine nucleobases are most desired because the ultimate objective of this imprinting is recognition components of nucleic acids of biological origin. Unfortunately, most of these native components of biological origin are insoluble in organic solvents. Therefore, functional monomers soluble in aprotic solvents and capable of recognizing nucleobases of ONs via Watson-Crick pairing were herein designed and synthesized.

For preparation of the (5'-TATAAA-3')-templated MIP and simultaneous deposition of its film on the gold electrode of QCR (Figure 3.1-3a, 3.1-3b, and 3.1-3c) or of the SPR disk (Figure 3.1-3d and 3.1-3e), the pre-polymerization complex of the 5'-TATAAA-3' template with **10** and **11** functional monomers was potentiodynamically electropolymerized in the presence of the cross-linking monomer **13**.

The anodic peak appearing at ~1.0 V vs. Ag|AgCl in the first current-potential curve in Figure 3.1-3a corresponded to electro-oxidation of the bis(2,2'-bithien-5-yl)methane moieties of the functional and cross-linking monomers. In subsequent cycles, current decreased indicating deposition of a relatively resistive polymer film, which hindered the charge transfer needed for further electro-oxidation of the monomers. The simultaneously recorded decrease of the resonance frequency change (Figure 3.1-3b) manifested the increase of mass of the polymer deposited. These changes were lower in each consecutive cycle indicating that less and less polymer mass was deposited. Moreover, the dynamic resistance change (Figure 3.1-3c) slightly increased (~24 Ω) after the electropolymerization pointing to the only minor increase of viscosity and/or density of the growing MIP film. This dynamic resistance change corresponded to the only negligible (17 Hz) resonance frequency change.[130] Therefore, the film mass was determined (~2 μg) by using the Sauerbrey relation

74

(Equation 2.3-23) with the visco-elasticity effects being neglected.[130-132] In the same manner, a control non-imprinted polymer (NIP)[133] film was prepared, however, in the absence of the 5'-TATAAA-3' template in the solution for electropolymerization.

During deposition of the (5'-TATAAA-3')-templated MIP film on the gold electrode of the SPR disk by potentiodynamic electropolymerization, each potential cycle (Figure 3.1-3d) was accompanied by a positive shift of the incidence angle (Figure 3.1-3e). This shift resulted from polymer deposition because this deposition changed optical properties of the dielectric adjacent to the metal layer supporting SPW.
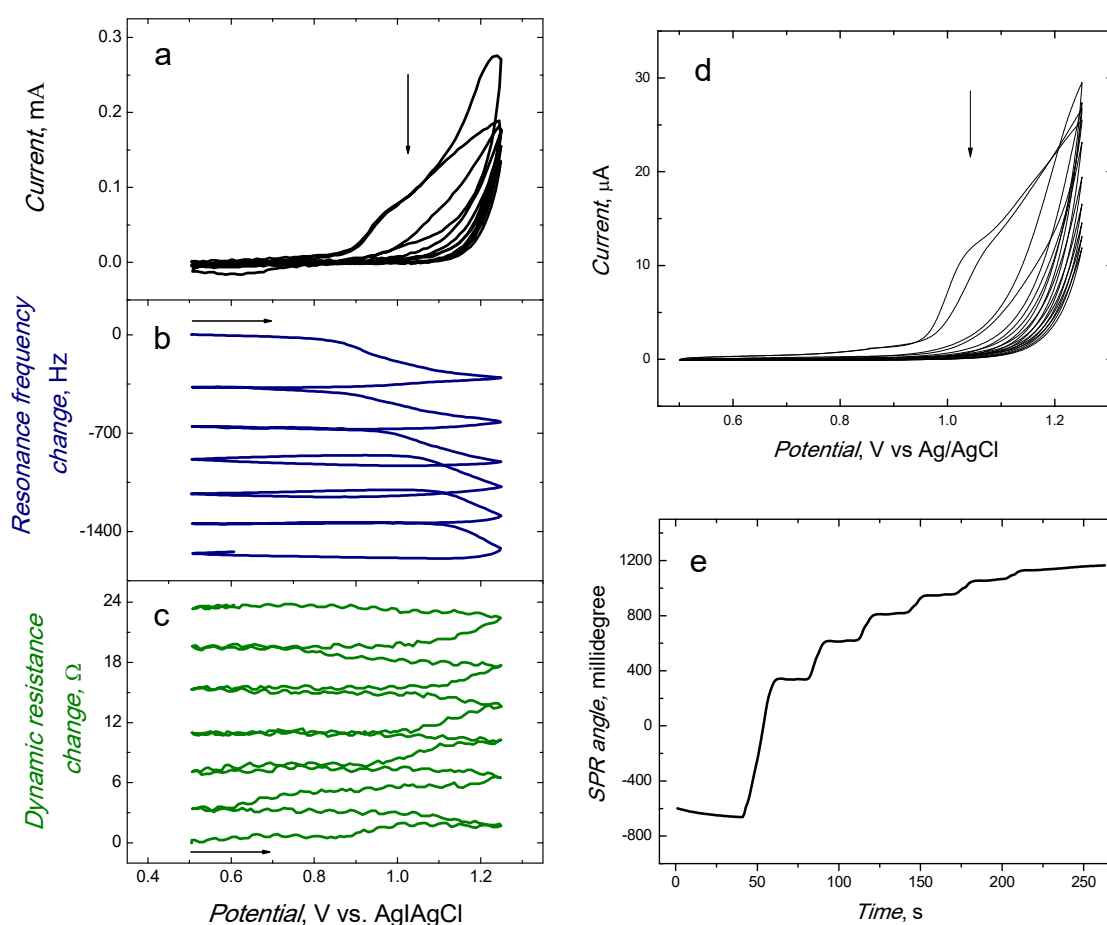
Figure 3.1-3. Simultaneously recorded multi-cycle potentiodynamic curves of (a) current, (b) resonance frequency change, and (c) dynamic resistance change vs. potential for electropolymerization of 40 µM 5'-TATAAA-3', 0.05 mM adenine functional monomer **10**, 0.1 mM thymine functional monomer **11**, and 0.2 mM cross-linking monomer **13** in the 0.1 M (TBA)ClO$_4$ solution of acetonitrile, water, toluene, and isopropanol of the volume ratio of 7.5 : 1.0 : 1.0 : 0.5 on the gold electrode of QCR.   (d) The current-potential curve simultaneously recorded with (e) the SPR angle vs. time curve, under FIA conditions, for this electropolymerization on the SPR gold disk. A potential scan rate was 50 mV s^{-1}.

The highest change in the SPR angle, accompanied by the first potential cycle, manifested the highest increase of mass of the polymer on the SPR gold electrode. Subsequent changes of the SPR signal were lower in each consecutive cycle indicating that less and less polymer mass was deposited.

According to specification of the SPR instrument, a 1-ng/mm^2 change in the density of the surface-bound analyte or deposited mass causes a 120-m° shift in the reflectance angle. Therefore, the total SPR change ($\Delta m° = 1822$) corresponded to ~15.18 ng of a polymer deposited on 1 mm^2 area of the SPR disk surface.

Next, PNA H$_2$N(CO)TATAAA-NH$_2$, soluble in aprotic solvents, was used as the template to verify the impact of the ODN analogue on the imprinting and sensing ability of the resulting MIP.
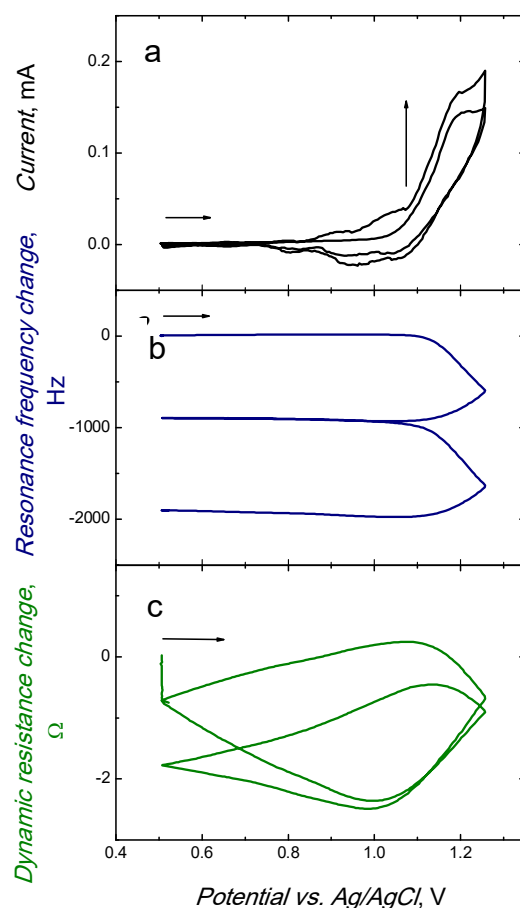

Figure 3.1-4. Simultaneously recorded two-cycle curves of (a) current, (b) resonance frequency change, and (c) dynamic resistance change vs. potential for deposition on the Au-quartz electrode of the PNA-templated MIP film by potentiodynamic electropolymerization from the 40 μM PNA H$_2$N(CO)TATAAA-NH$_2$, 0.1 mM adenine functional monomer **10**, 0.2 mM thymine functional monomer **11**, and 0.2 mM cross-linking monomer **13**, 0.1 M (TBA)ClO$_4$ solution of acetonitrile. A potential scan rate was 50 mV s^{-1}.

For preparation of the (PNA H$_2$N(CO)TATAAA-NH$_2$)-templated MIP film, pre-polymerization complex of the **10** and **11** functional monomers with PNA H$_2$N(CO)TATAAA-NH$_2$ **6** was electropolymerized on a gold electrode of QCR (Figure 3.1-4). The anodic peak at ~1.17 V vs. Ag|AgCl in the first current-potential cycle (Figure 3.1-4a) corresponds to electro-oxidation of the (2,2'-bithien-5-yl)methane moieties of functional monomers **10** and **11** as well as of cross-linking monomer **13**. In the subsequent cycle, current increased indicating deposition of an electroactive polymer film. Thus, the film did not hinder the charge transfer needed for further electro-oxidation of the monomers. This behavior can be explained by the absence of water in the pre-polymerization complex solution.

Because the PNA H$_2$N(CO)TATAAA-NH$_2$-MIP did not hinder further electropolymerization, only two potential cycles were needed for complete polymer deposition. The decrease of the resonance frequency (Figure 3.1-4b) resulted from the mass increase of the polymer film deposited on the QCR. Simultaneous negligible decrease (2 Ω) of the dynamic resistance in the first cycle, and then its return to the background curve in the second cycle (Figure 3.1-4c) indicated that the MIP film was rigid.

Thus, procedures of imprinting of the natural ODN as well as its synthetic analogue, PNA, into MIP films were developed using nucleobase-substituted 2,2'-bithien-5-yl functional monomers designed for the Watson-Crick pairing. These experiments were carried out to verify if both the 5'-TATAAA-3' and PNA H$_2$N(CO)TATAAA-NH$_2$ were capable of transferring the nucleobase sequence of the TATAAA to MIPs and if these MIPs would then recognize the analyte with the similar affinity. Moreover, the aim of the imprinting was to check if a minute amount of water in the pre-polymerization complex solution, needed to dissolve the 5'-TATAAA-3' and to maintain its native conformation during imprinting, influenced recognition properties of the resulting MIP film of the chemosensor.

3.1.4 Extraction of the sequence-programmable templates from TATAAA-templated MIP films

From polymer films deposited on different electrodes, 5'-TATAAA-3' and PNA H$_2$N(CO)TATAAA-NH$_2$ templates were chemically removed in order to vacate the imprinted cavities containing the nucleobase of the sequence programmed. These

cavities can be considered as 2,2'-bithien-5-yl TTTATA oligomers serving as recognition units of a chemosensor for selective determination of the 5'-TATAAA-3' analyte.

The experimental confirmation of the 5'-TATAAA-3' or PNA $H_2N(CO)$TATAAA-NH_2 removal was different for each type of the template imprinted. For the (PNA $H_2N(CO)$TATAAA-NH_2)-templated MIP film, the template was extracted with 20% trifluoroacetic acid for 45 min under stagnant-solution conditions. This extraction was monitored with piezoelectric microgravimetry. The increase of the resonance frequency evidenced the decrease of the (PNA $H_2N(CO)$TATAAA-NH_2)-templated MIP mass, which was caused by the removal of the PNA $H_2N(CO)$TATAAA-NH_2 template (Figure 3.1-5a).

Piezoelectric microgravimetry was also chosen for verifying the extent of occupation of the imprinted cavities of the (5'-TATAAA-3')-templated MIP film deposited on the Au-QCR. However, the PM measurement was indirect. That is, the absence of the template in the cavity was demonstrated by the capability of this cavity to bind the 5'-TATAAA-3' analyte. For that, a 20-µM sample of the analyte solution was injected after different time of template extraction with 0.1 M NaOH under flow conditions (Figure 3.1-5b). The resonance frequency decrease indicated emptying more and more cavities as a result of extending extraction time.
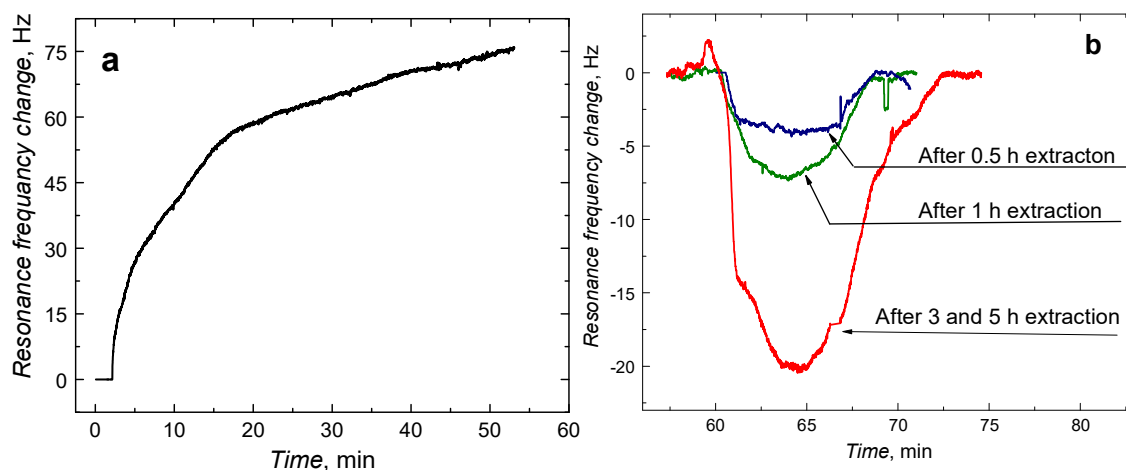
Figure 3.1-5. (a) The time dependence of the resonance frequency change of the 10 MHz Au-quartz crystal resonator under stagnant-solution conditions in response to extraction of PNA $H_2N(CO)$TATAAA-NH_2 from the (PNA $H_2N(CO)$TATAAA-NH_2)-templated MIP film with 20% trifluoroacetic acid. (b) Piezomicrogravimetric determination of 20 µM 5'-TATAAA-3' analyte after different time of extraction with 0.1 M NaOH under flow conditions.

78

However, after 3 h of the template removal there was no further decrease of the resonance frequency change after injection of the analyte, thus meaning that the extraction was complete.

Next, the films of 5'-TATAAA-3' drop-cast onto the Au-QCR electrode (Figure 3.1-6a) and the (5'-TATAAA-3')-templated MIP film (Figure 3.1-6b) were analyzed by XPS for determination of elemental surface composition. Deconvolution of both spectra revealed the same doublet of the $2p_{3/2}$ and $2p_{1/2}$ peaks of the binding energy of 133.7 and 134.5 eV,[134] respectively, thus identifying the phosphorus element. The 5'-TATAAA-3' is the only source of phosphorus in the studied system. Therefore, the phosphorus occurrence in the XPS spectra confirmed the presence of the TATAAA template in the (5'-TATAAA-3')-templated MIP film (curve *1* in Figure 3.1-6b). After treating the film with 0.1 M NaOH, the peak of phosphorus disappeared (curve *2* in Figure 3.1-6b), thus indicating that the 5'-TATAAA-3' template complete removal from the film.

Moreover, the complementary information about the (5'-TATAAA-3')-templated MIP film provided by the XPS multipoint surface analysis[135] was explored to identify surface elemental composition of the film and spatial atomic distribution (Table 3.1-2). Apparently, the MIP film with the 2,2'-bithien-5-yl TTTATA oligomer was homogeneous.
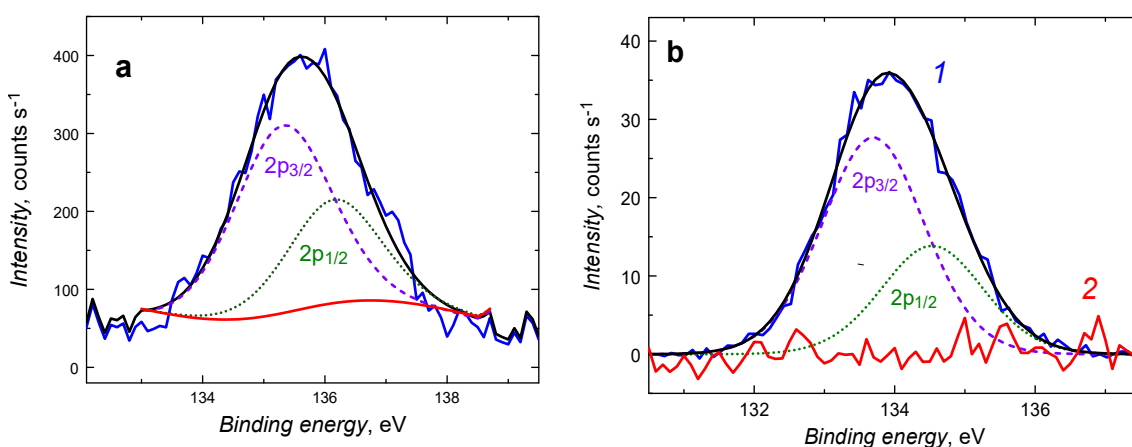
Figure 3.1-6. The high-resolution XPS spectra of phosphorus 2p for (a) the 5'-TATAAA-3' film drop-cast on the Au-QCR electrode and (Panel b, curve *1*) the (5'-TATAAA-3')-templated MIP film deposited on the Au-QCR electrode by potentiodynamic electropolymerization; deconvoluted peaks (dotted and dashed curves) stand for the P $2p_{3/2}$ and P $2p_{1/2}$ photoelectron spin-orbit states. (Panel b, curve *2*) The spectrum of P 2p of the (5'-TATAAA-3')-templated MIP film after treatment with 0.1 M NaOH for 3 h.

That is, 3-D molecular cavities were homogeneously imprinted in it and nucleobases of the electrochemically synthesized 2,2'-bithien-5-yl TTTATA were available for Watson-Crick pairing of nucleobases of the 5'-TATAAA-3' analyte..
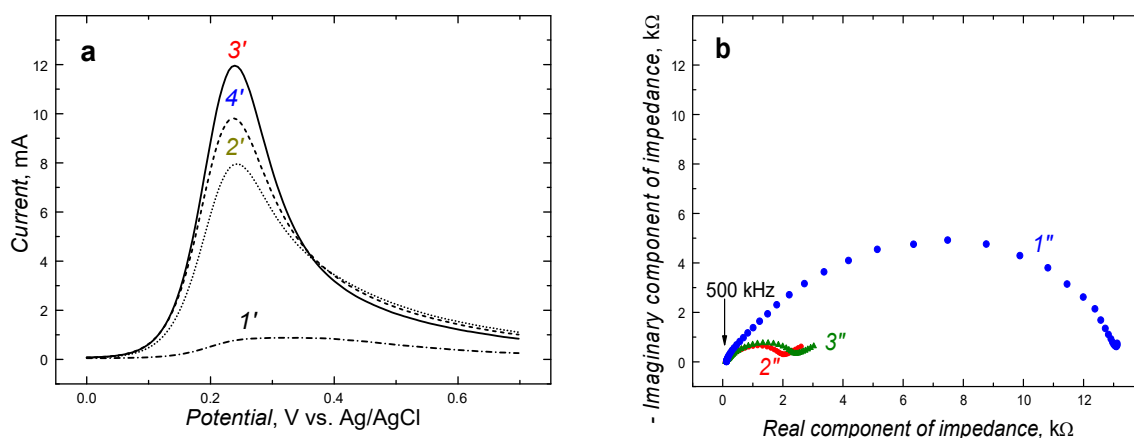
For the (5'-TATAAA-3')-templated MIP film deposited on the Pt disk electrode, template removal was confirmed electrochemically. That is, in the DPV experiment using the "gate effect" for studying the MIP film with the 5'-TATAAA-3' template molecules occupying the imprinted cavities, the anodic peak current of $Fe(CN)_6^{4-}$ redox marker oxidation was hardly seen (curve *1* in Figure 3.1-7a). Moreover, in the EIS study, the Nyquist plot for the Pt disk electrode coated with the (5'-TATAAA-3')-templated MIP film, was represented by a large arc related to a high charge transfer resistance, R_{ct} = 13 kΩ (curve *1''* in Figure 3.1-7b), of the $Fe(CN)_6^{4-}/Fe(CN)_6^{3-}$ redox marker. Apparently, the 5'-TATAAA-3' template presence in the MIP film hindered the $Fe(CN)_6^{4-}/Fe(CN)_6^{3-}$ electrode process. Next, the template was gradually extracted from imprinted cavities, thus allowing for marker molecules diffusive permeation through the film. This extraction progress was manifested by the DPV peak increase in consecutive steps of the extraction (curves *2'* and *3'* in Figure 3.1-7a). Furthermore, the diameter of the arc part of the Nyquist plot (curve *2''* in Figure 3.1-7b) smaller than that in curve *1''* in Figure 3.1-7b, implied a lower charge transfer resistance (R_{ct} = 2.04 kΩ) of the template-free MIP film coated electrode.

Table 3.1-2. Surface elemental composition of the (5'-TATAAA-3')-templated MIP film determined using the multipoint XPS spectra analysis.[a]

Element	Concentration, atomic %	
	XPS data	Stoichiometric number
N	3.4 ± 0.8	5.5
O	10.6 ± 1.3	6.9
S	14.0 ± 0.9	13.6
P	0.5 ± 0.1	0.8
C	72.0 ± 2.8	73.2

[a] The XPS spectra were acquired at five spots of surface area (250 μm × 250 μm), separated by 2 mm.

After complete template extraction, the resulting 2,2'-bithien-5-yl TTTATA, immobilized in molecular cavities of the MIP film, hybridized to the 5'-TATAAA-3' analyte. In effect, the DPV peak decreased after immersing this electrode in the 5'-TATAAA-3' analyte solution (curve *4'* in Figure 3.1-7a), thus confirming that redox marker diffusion in the film was hindered again. Moreover, the diameter of the resulting arc of the Nyquist plot increased to reach R_{ct} = 2.42 kΩ (curve *3''* in Figure 3.1-7b), thus indicating that the target 5'-TATAAA-3' analyte was bound by the TTTATA site in the MIP molecular cavity.

Figure 3.1-7. (a) Differential pulse voltammograms and (b) Nyquist plots for 0.1 M K$_4$Fe(CN)$_6$ in 0.1 M KNO$_3$, recorded at the 1-mm diameter Pt disk electrode coated with the (5'-TATAAA-3')-templated MIP film (*1'* and *1''*) before and after (*2'*) 25, and (*3'* and *2''*) 45 min of 5'-TATAAA-3' extraction with 0.1 M NaOH, and then (*4'* and *3''*) after immersing the electrode in 50 μM 5'-TATAAA-3' for 15 min. The film was prepared by potentiodynamic electropolymerization in the potential range of 0.50 to 1.25 V vs. Ag|AgCl at a 50 mV s^{-1} scan rate.

3.1.5 PM-IRRAS and AFM characterization of the TATAAA-MIP films

PM-IRRAS measurements were carried out in search for spectral properties of the TTTATA-substituted 2,2'-bithien-5-yl polymer (Figure 3.1-8). The presence of bands in regions of 1580–1320 and 1290–1140 cm^{-1}, characteristic of vibrations of polybithiophene bonds, confirmed the presence of the 2,2'-bithien-5-yl backbone of the resulting ODN TTTATA analogue. The band at ~1222 cm^{-1} (spectrum *1* in Figure 3.1-8), assigned to the PO$_2^-$ and P-O-P bond stretching vibrations in 5'-TATAAA-3', substantiated the presence of these bonds of the 5'-TATAAA-3' template in the MIP film. The relative band intensity for the (5'-TATAAA-3')-templated MIP was

significantly lower after template extraction (spectrum *2* in Figure 3.1-8) and for the corresponding NIP (spectrum *3* in Figure 3.1-8) than that before template extraction (spectrum *1* in Figure 3.1-8). Moreover, there was a broad set of bands in these regions characteristic of the vibrations of the nucleobase bonds. The relative intensity of these bands was the highest for the (5'-TATAAA-3')-templated MIP film (spectrum *1* in Figure 3.1-8). That way, hybridization of the 5'-TATAAA-3' template with the 2,2'-bithien-5-yl TTTATA oligomer in the MIP matrix was confirmed. However, relative intensities of these bands decreased after extraction of the 5'-TATAAA-3' template (spectrum *2* in Figure 3.1-8), which resulted from dehybridization in the MIP cavities.

Moreover, nucleobase pairing of the template with functional monomers was manifested by enhancement of the band at 1690 cm^{-1} corresponding to C=O stretching vibration (spectrum *1* in Figure 3.1-8). After extraction, this band disappeared (spectrum *2* in Figure 3.1-8) as a result of dehybridization.
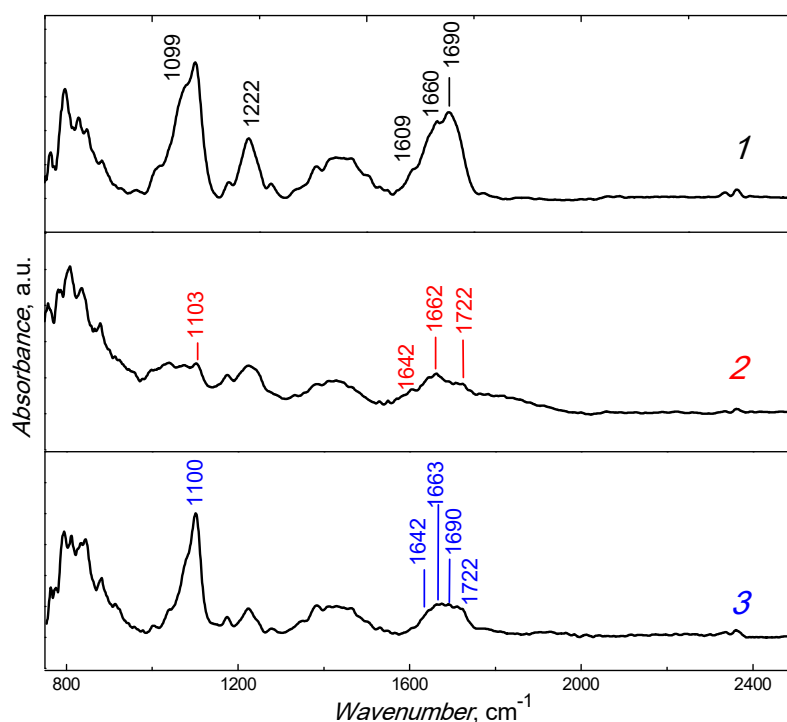
Figure 3.1-8. The normalized PM-IRRAS spectra of the (5'-TATAAA-3')-templated MIP film (*1*) before and (*2*) after 5'- TATAAA-3' template extraction with 0.1 M NaOH as well as (*3*) the non-imprinted polymer (NIP) film. All films were deposited on Au-glass slides.

The (5'-TATAAA-3')-templated MIP and (PNA H$_2$N(CO)TATAAA-NH$_2$)-templated MIP films were imaged by AFM (Figure 3.1-9) in order to unravel their morphology and determine their thickness. In case of the (5'-TATAAA-3')-templated

MIP, the film was composed of ~30-nm diameter grains (Figure 3.1-9a). Their thickness was 140(±3) nm. For the (PNA H$_2$N(CO)TATAAA-NH$_2$)-templated MIP film, the AFM imaging revealed its morphology of well-defined grains with diameter in the range of 30 to 60 nm (Figure 3.1-9b). Its thickness was 114(±5) nm.

The measured thicknesses of the (5'-TATAAA-3')-templated MIP and (PNA H$_2$N(CO)TATAAA-NH$_2$)-templated MIP films were different. Different conditions of electropolymerization of the pre-polymerization complexes and different surface areas of the gold electrodes used were the reasons of this discrepancy.
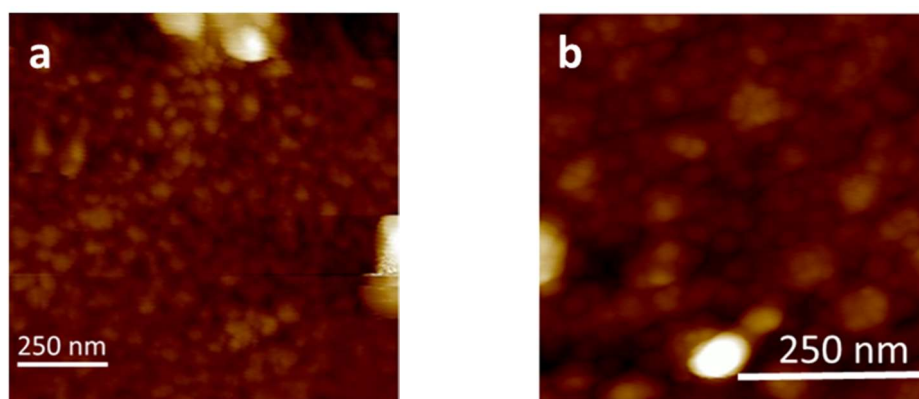
Figure 3.1-9. (a) The (0.5×0.5) μm^2 AFM image of the (5'-TATAAA-3')-templated MIP film deposited on the Au-glass slide. (b) The (1.0×1.0) μm^2 AFM image of the (PNA H$_2$N(CO)TATAAA-NH$_2$)-templated MIP film deposited on the Au-QCR.

3.1.6 Analytical performance of the (5'-TATAAA-3')-templated MIP chemosensor for 5'-TATAAA-3' determination

Analytical performance of the (5'-TATAAA-3')-templated MIP chemosensor with respect to the 5'-TATAAA-3' determination was examined with PM and CI, both under FIA conditions, as well as with SPR spectroscopy under stagnant-solution conditions. Moreover, the kinetic aspect of the 5'-TATAAA-3' recognition with the 2,2'-bithien-5-yl TTTATA oligomer was investigated using the PM transduction.

3.1.6.1 Piezoelectric microgravimetry (PM) chemosensor

Hybridization of the 5'-TATAAA-3' analyte in molecular cavities of the MIP film was studied by PM under FIA conditions. After each injection of the analyte sample solution, resonance frequency decreased (Figure 3.1-10a) because the analyte entered the film and, accordingly, the film mass increased, as Sauerbrey equation predicts.

After reaching minimum, this frequency increased to its initial baseline value indicating a complete removal of the analyte from the film by abundance of the carrier solution. Figure 3.1-10a shows the resonance frequency change with time for six consecutive injections of the 5'-TATAAA-3' analyte solutions of different concentrations, which allowed constructing the calibration plot (curve *1* in Figure 3.1-10b).

The chemosensor response to the 5'-TATAAA-3' analyte was linear in the concentration range of at least 0.5 to 10 µM. It was described by the linear regression equation of Δf [Hz] = -0.66(±0.02) [Hz] -1.07(±0.04) [Hz µM^{-1}] $c_{5'\text{-TATAAA-3'}}$ [µM]. The LOD, sensitivity, and correlation coefficient at the signal-to-noise ratio, $S/N = 3$, was 110 nM, 1.07(±0.04) Hz µM^{-1}, and 0.99, respectively. The NIP control film sensitivity to the 5'-TATAAA-3' analyte was four times lower, equaling 0.27(±0.03) Hz µM^{-1}, and, therefore, a reasonably high imprinting factor of 4.0 was calculated from the ratios of the sensitivity of the MIP and NIP film to 5'-TATAAA-3'.
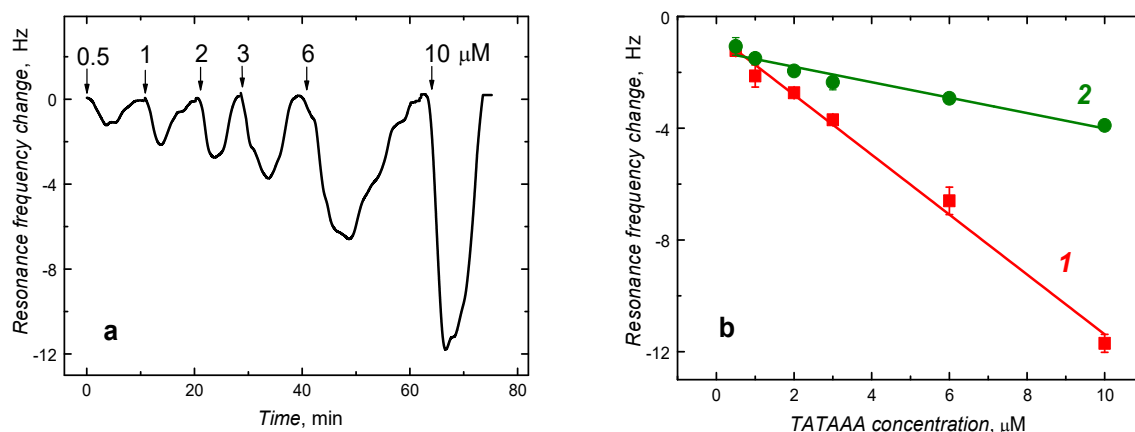
Figure 3.1-10. (a) The resonance frequency change with time for repetitive FIA injections of 5'-TATAAA-3' analyte of the concentration indicated at each peak for the (5'-TATAAA-3')-templated MIP film coated Au-QCR. (b) Calibration plots for 5'-TATAAA-3' determined at the (*1*) (5'-TATAAA-3')-extracted MIP and (*2*) NIP films. The flow rate of the PBS (pH = 7.4) carrier solution was 30 µL min^{-1}.

Determination of the 5'-TATAAA-3' analyte was possible because synthetic non-labeled probes with a very high affinity to the complementary analyte were generated inside the polymer. Advantageously, the constrained 2,2'-bithien-5-yl TTTATA oligomer, immobilized in the MIP cavities, hybridized to the 5'-TATAAA-3' analyte at room temperature under FIA conditions within 2 min.

3.1.6.2 Surface plasmon resonance spectroscopic chemosensor for selective 5'-TATAAA-3' determination

In SPR spectroscopy measurements, performed under stagnant-solution conditions, hybridization of the 5'-TATAAA-3' analyte by the complementary TTTATA probe, generated in the MIP, induced a change in the refractive index. This change was proportional to the 5'-TATAAA-3' mass load of the film, thus enabling the real-time hybridization monitoring. Herein, the 5'-TATAAA-3' analyte caused a shift of the reflectivity to higher angles as the result of a significant change in the refractive index of the MIP film coated SPR chip (Figure 3.1-11a).
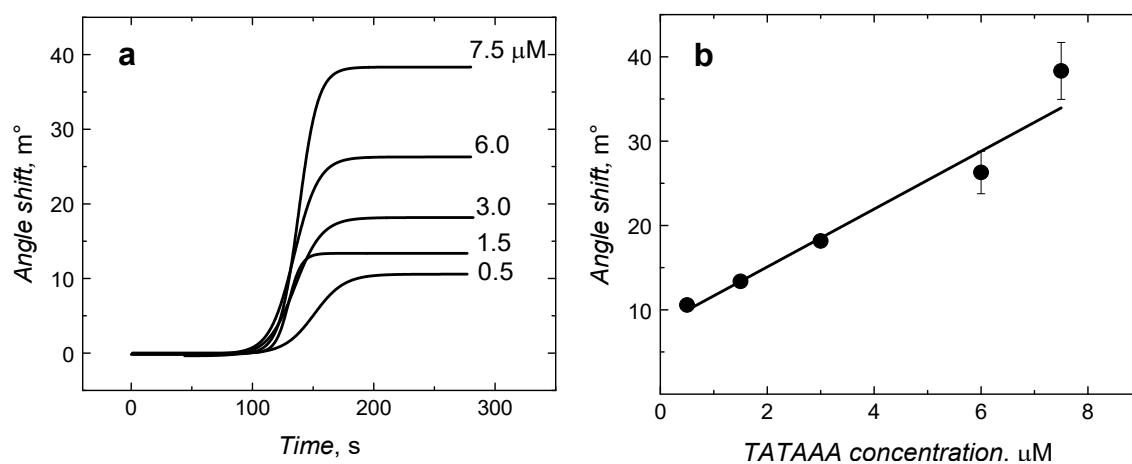
Figure 3.1-11. (a) The SPR signal vs. time transients for determination of the 5'-TATAAA-3' analyte of different concentrations indicated at curves. (b) The SPR calibration curve for the 5'-TATAAA-3' analyte determination. The film of MIP with the 2,2'-bithien-5-yl TTTATA oligomer immobilized in its molecular cavities, deposited by potentiodynamic electropolymerization on the SPR chip, was used.

The SPR calibration plot constructed for the 5'-TATAAA-3' analyte (Figure 3.1-11b) was described by the linear regression equation of ΔR [m°] = 8.22(±0.49) [m°] + 3.43(±0.30) [m° μM^{-1}] $c_{5'-TATAAA-3'}$ [μM] where R stands for the SPR signal. The LOD reached was appreciably low equaling ~50 nM 5' TATAAA -3', which is half that attained herein by PM. This impressively low LOD value is particularly important because the SPR chip response to the analyte presence was enhanced with neither AuNPs nor proteins.

3.1.6.3 Piezoelectric microgravimetry (PM) analysis of kinetic data

Kinetic analysis of the PM-FIA data of the 5'-TATAAA-3' analyte interaction with the MIP[114,136] provided values of the association, $k_a \approx 10^4\,M^{-1}\,s^{-1}$, and dissociation, $k_d = 10^{-2}\,s^{-1}$, rate constants. This analysis revealed that 2,2'-bithien-5-yl TTTATA oligomer hybridized 5'-TATAAA-3' with a high stability constant, $K_s^{TTTATA-TATAAA} = k_a/k_d \approx 10^6\,M^{-1}$, comparable to that characteristic for longer-chain DNA-PNA hybrids (Table 3.1-3). The above rate constants were determined by fitting theoretical data to experimental PM-FIA data. These constants well compared with those determined with the SPR analysis using the literature procedure.[114,136]

To date, a state-of-art SPR biosensor detected a short (15-mer) ON target ($M_w = 5\,kDa$) via complementary probe hybridization with a similar like that determined herein k_a value of $10^4\,M^{-1}\,s^{-1}$.[137] Moreover, stability constants of complexes of native nucleic acid "hosts" with their cognate ligand "guests" are relatively low being of the order of $10^3\,M^{-1}$.[138] Advantageously, the presently determined $K_s^{TTTATA-TATAAA}$ value for the probe is comparable to those for much longer-chain DNA-PNA hybrids, $10^6\,M^{-1}$ (for PNA H$_2$N(CO)GCAT**TT**GCAT-NH$_2$) $\leq K_s^{DNA-PNA} \leq 10^7\,M^{-1}$ (for PNA-H$_2$N(CO)GCAT**GA**GCAT-NH$_2$).[129,139] Notably, the described herein procedure proposes circumventing disadvantages connected with a very low stability of short ON hybrids at room temperature.

Table 3.1-3. Comparison of stability constants of the probe-target complexes for different nucleic acid chemosensors.

Probe	K_s, M^{-1}	Target	Ref.
2,2'-Bithien-5-yl ODN analogue	10^6	5'-TATAAA-3'	Present work
PNA-GCATTTGCAT	10^6	Probe-complementary ODN	[129]
PNA-GCATGAGCAT	10^7	Probe-complementary ODN	[129]

3.1.6.4 Capacitive impedimetric (CI) chemosensor for selective 5'-TATAAA-3' determination

In CI determination of 5'-TATAAA-3' under FIA conditions, the electrical double-layer capacity, C_{dl}, at the Pt-MIP interface was determined from measurements of the

imaginary component of impedance, Z_{im}. Considering only the compact part of the double layer, we determined C_{dl} at the Pt-MIP interface by measuring Z_{im} according to Equation 2.2-21. The C_{dl} changes corresponded to the changes of electric permittivity, ε, and the double-layer thickness, d_{dl}, as Equation 2.2-22 describes.

After 5'-TATAAA-3' binding, the permittivity increased, so the capacity did (Figure 3.1-12a). Apparently, the recognizing MIP film reversibly bound the analyte. Based on the CI measurements, calibration plots were constructed for the MIP and NIP film coated electrodes (curves *1 – 3*, and *4*, respectively, in Figure 3.1-12b). The linear dynamic concentration range extended from at least 0.05 to 2.0 µM 5'-TATAAA-3' (curve *1* in Figure 3.1-12b) obeying the linear regression equation of C_{dl} [µF cm^{-2}] = 2.67($\pm$0.13) [µF cm^{-2}] + 2.07($\pm$0.13) [µF cm^{-2} µM^{-1}] c_{TATAAA} [µM]. The LOD, determined at $S/N = 3$, reached as low value as ~5 nM TATAAA. The sensitivity and correlation coefficient was 2.07($\pm$0.13) µF cm^{-2} µM^{-1} and 0.98, respectively.
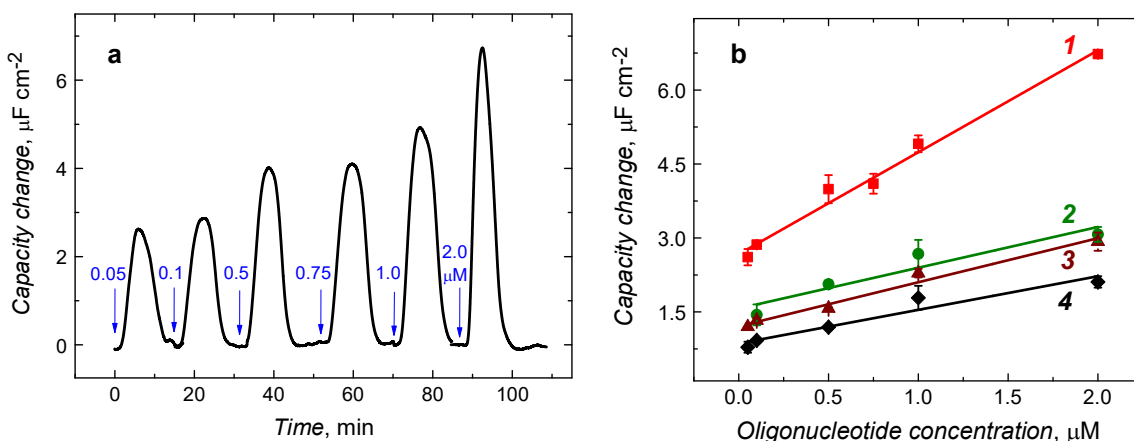
Figure 3.1-12. (a) The capacity change with time of the MIP film coated Pt disk electrode in response to repetitive FIA 200-µL injections of 0.1 M NaF solutions of 5'-TATAAA-3'. The 5'-TATAAA-3' concentration is indicated at each peak. The flow rate of 0.1 M NaF, serving as the carrier solution, was 20 µL min^{-1}. (b) Calibration plots for (*1*) 5'-TATAAA-3' and mismatched ODNs, namely, (*2*) 5'-TATA**G**A-3', (*3*) 5'-TATAA**G**-3', on the (5'-TATAAA-3')-extracted MIP film deposited on the Pt disk electrode as well as (*4*) 5'-TATAAA-3' on the NIP film deposited on the Pt disk electrode. Frequency, 20 Hz; potential, 0.50 V vs. Ag|AgCl; the sinusoidal voltage amplitude, 10 mV.

The chemosensor selectivity was determined under the same CI conditions of FIA by examining sensitivity of the MIP film to ODNs of mismatched sequences, i.e., hexamers mismatched with just one nucleobase, vis. 5'-TATAA**G**-3' and 5'-TATA**G**A-3',. The MIP chemosensor was ~3.0 and ~2.3 times more sensitive to the 5'-TATAAA-3' analyte than to the 5'-TATA**G**A-3' and 5'-TATAA**G**-3' mismatches, respectively.

Moreover, the 5'-TATAAA-3' analyte was determined at a control NIP film (curve *4* in Figure 3.1-12b) to confirm the imprinting. The 5'-TATAAA-3' binding by the NIP with the sensitivity of $0.82(\pm 0.19)$ $\mu F\ cm^{-2}\ \mu M^{-1}$ was significantly (~2.5 times) weaker than that by of the MIP.

Apparently, the present 5'-TATAAA-3' template imprinting was governed by the Watson-Crick nucleobase pairing of template nucleobases with nucleobases of functional monomers. Subsequent electropolymerization, and then template removal resulted in the nucleobase-substituted 2,2'-bithien-5-yl TTTATA oligomer probe selectively hybridizing the complementary 5'-TATAAA-3' analyte.

3.1.7 Analytical performance of the (PNA H$_2$N(CO)TATAAA-NH$_2$)-templated MIP film

The (PNA H$_2$N(CO)TATAAA-NH$_2$)-templated MIP film was used as the recognition unit of a chemosensor for selective determination of the 5'-TATAAA-3' analyte. To check whether the template-emptied cavities contain 2,2'-bithien-5-yl TTTATA recognizing probe or not, the samples of 10 µM 5'-TATAAA-3' (Figure 3.1-13a) and 10 µM PNA H$_2$N(CO)TATAAA-NH$_2$ (Figure 3.1-13b) were consecutively injected to the carrier solution under PM-FIA conditions.

The resonance frequency decrease evidenced both 5'-TATAAA-3' and PNA H$_2$N(CO)TATAAA-NH$_2$ binding with the probe. Thus, the (PNA H$_2$N(CO)TATAAA-NH$_2$)-templated MIP with emptied cavities appeared suitable for detection of the AT-rich 5'-TATAAA-3' analyte. A comparable resonance frequency drops indicated equal affinity of the MIP film to both the 5'-TATAAA-3' and its PNA close analogue. Expectedly, this was possible because the spacing between the nucleotides in the 5'-TATAAA-3' is the same as that in the PNA H$_2$N(CO)TATAAA-NH$_2$.[140]

Moreover, the 5'-TATAAA-3' analyte determination signals on both 5'-TATAAA-3' and (PNA H$_2$N(CO)TATAAA-NH$_2$)-templated MIPs were comperable. This indicated that a minute amount of water, added to the pre-polymerization solution of the (5'-TATAAA-3')-templated MIP, had no effect on recognition properties of the MIP film of the chemosensor.
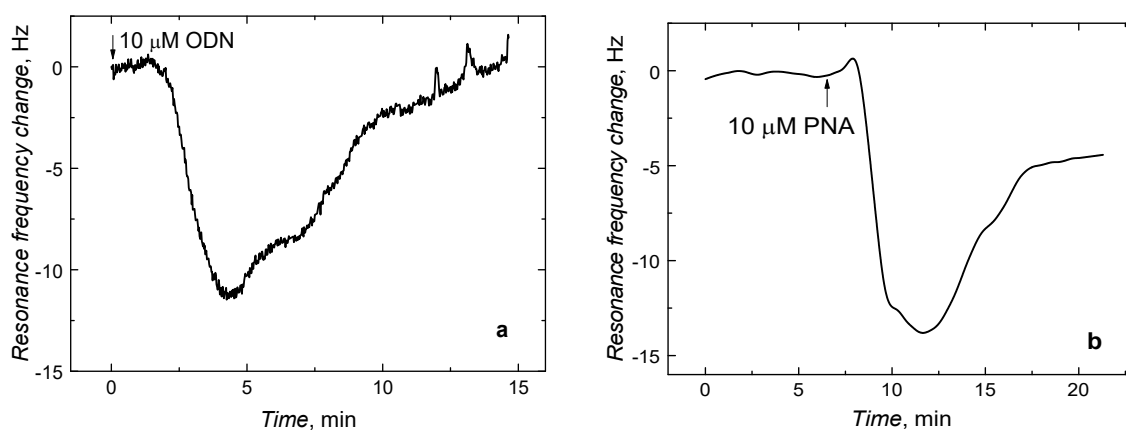
Figure 3.1-13 The resonance frequency change with time of the PNA H$_2$N(CO)TATAAA-NH$_2$-templated MIP coated 10 MHz Au-QCR for FIA injections of 10 µM (a) 5'-TATAAA-3' and (b) PNA TATAAA. The PBS (pH = 7.4) served as the carrier solution; its flow rate was 30 µL min^{-1}.

3.1.8 Synthetic TATA box affinity to amino acids

By mimicking natural Watson-Crick nucleobase pairing, we used molecular imprinting to prepare the TTTATA oligomer probe. Preparation of this oligomer involved polymerization of the complex of the 5'-TATAAA-3' template with functional monomers **10** and **11** in the presence of the cross-linking monomer **14**. The proposed structural formula of the complex is presented in Scheme 3.1-2. The electropolymerized complex can be considered as a fragment of the artificial TATA box. The research described in the present section involves an MIP governed strategy used to devise and fabricate a stable minimal motif of an undistorted (due to nucleobase stacking) artificial dsDNA fragment. This strategy aims at unraveling nucleic acids interactions with compounds providing the desired biological function. Certainly, it is premature to foresee fully-synthetic processes having the degree of complexity and reliability of natural systems. Current chemical tools do not allow approaching the replication, transcription, or translation machinery even remotely. However, each of simplified and exploited man-made platforms transforming information controlled at the molecular level in synthetic polymer chains deepens understanding of critical cell functions (a class of DNA-protein contacts). Moreover, it can open doors for developing new medical and biological applications, including rational drug designing and gene expression controlling.[141]

Several DNA-protein complexes have already been studied.[142] However, there is a long way to explain origins of specificity of these interactions. No simple rules have so far been formulated for a general recognition code that adequately explains complexation for all proteins. For study of specific DNA-protein interactions, selected pairs of amino acids and DNA nucleobases have been examined extensively.[143] In general, a large majority of both experimental and computational studies have only focused on specific binding interactions of the amino acid with nucleobases.[144] Noteworthy, it seems feasible to extend the analysis of hydrogen bonds of a simple one-to-one (amino acid)-nucleobase interaction, characterized using molecular modeling, to include complex interaction networks involving multiple nucleobase steps (stacked nucleobase pairs) in the MIP.[142] These interactions are indispensable for the overall specificity of DNA-protein complexes. Herein, main interest involved interactions of amino acids with nucleobases of the artificial TATA box and the effect they exert on specificity of short 5'-TATAAA-3' interaction with amino acids.

The artificial TATA box in the MIP film was comprehensively characterized by PM-IRRAS (Figure 3.1-8) in Section 3.1.5 and by XPS (Figure 3.1-6) in Section 3.1-4. Moreover, a high-resolution XPS was combined with a very low energy argon ion (Ar$^+$) beam sputtering for a depth-profile chemical analysis of the (5'-TATAAA-3')-templated MIP film near its surface (Table 3.1-4). In this way, depth distribution of the hybridized 5'-TATAAA-3' was evaluated in the MIP film. By measuring the high-resolution XPS spectra of C 1s, O 1s, S 2p, N 1s and P 2p after each consecutive step of Ar$^+$ ion etching, a relative content of the carbon, oxygen, sulfur, nitrogen, and phosphorus atoms, respectively, was identified in the bulk of the film.

The present depth-profile XPS chemical analysis of the (5'-TATAAA-3')-templated MIP film revealed that the nitrogen-to-phosphorus ratio in the outermost MIP layer and that for deeper located layers remained equal. The relative atomic phosphorus content detected on the 10-nm depth of probing was only slightly higher than that on the 20-nm depth (Table 3.1-4). Thus, homogeneous distribution of the 5'-TATAAA-3' in the MIP film surface vicinity was evidenced.

With XPS depth profiling, a strong relationship between nucleobase density in the MIP and MIP nucleobase affinity to their cognate amino acids was demonstrated. Homogeneous distribution of the 5'-TATAAA-3' in the MIP allows for direct interactions of nucleobases immobilized in the MIP with amino acids, including their intercalation.
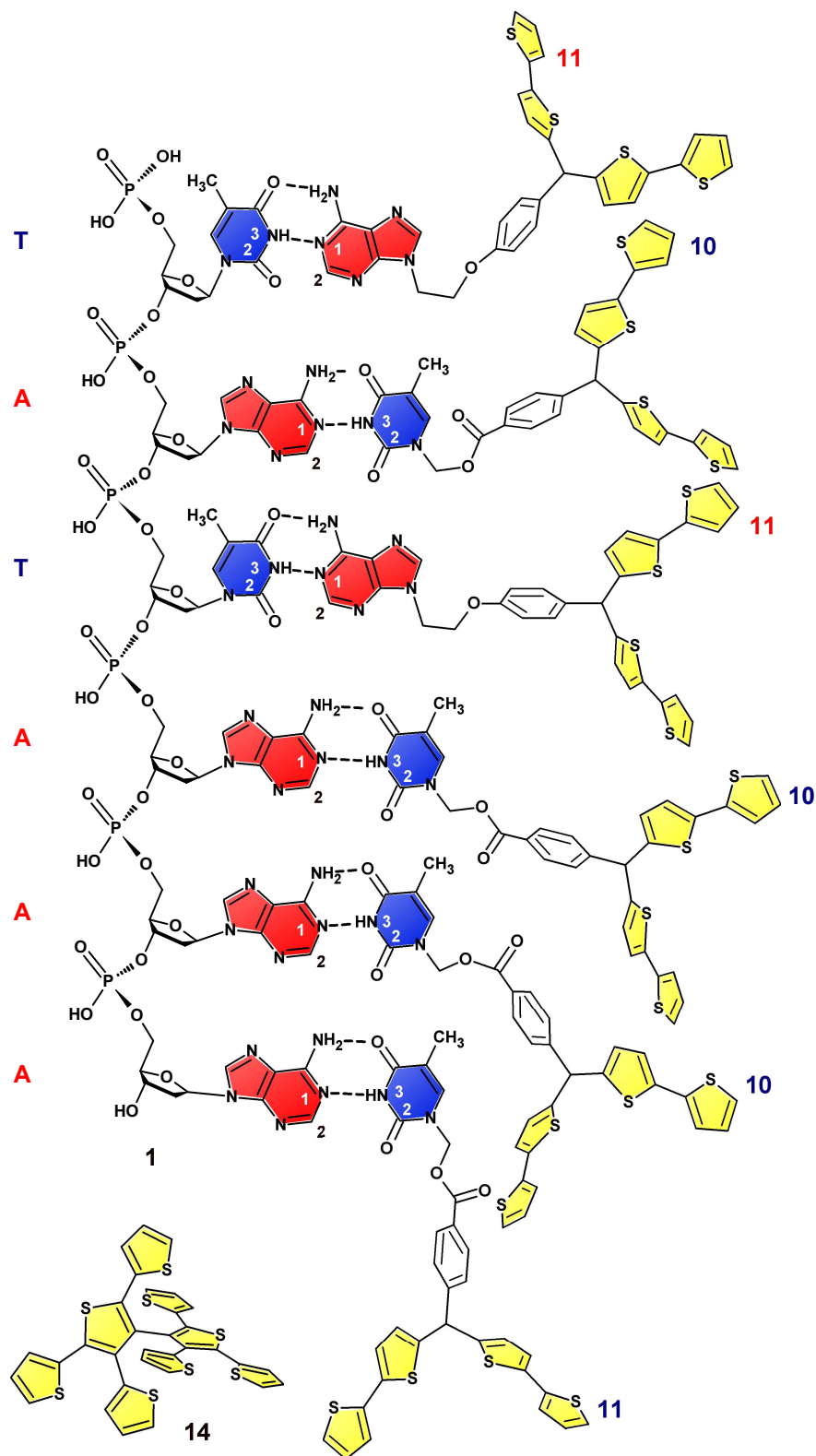
Scheme 3.1-2. Structural formulas of the pre-polymerization complex of 5'-TATAAA-3' **1** with the 4-*bis*(2,2'-bithien-5-yl)methylphenyl thymine-1-acetate **10** and 4-*bis*(2,2'-bithien-5-yl)methylphenyl 2-adenine ethyl ether **11** functional monomers in the presence of the 2,4,5,2',4',5'-hexa(thiophene-2-yl)-3,3'-bithiophene **14** cross-linking monomer.

Table 3.1-4. The elemental depth-dependent composition of the MIP-(5'-TATAAA-3') film determined using the XPS depth-profiling analysis.

Element	Elemental composition, atomic %		
	MIP-(5'-TATAAA-3') at the depth of 0 nm	MIP-(5'-TATAAA-3') at the depth of 10 nm	MIP-(5'-TATAAA-3') at the depth of 20 nm
C	71.2	67.9	70.6
O	14.2	14.7	12.2
S	8.2	9.6	9.5
N	5.6	6.8	6.5
P	0.8	1.0	1.2
Total	100	100	100

To highlight relations of the artificial TATA box structure with functioning of the natural TATA box, composition of the former and its properties was determined. For this, interactions of the MIP film with selected amino acids, which interact with the natural TATA box, were examined.

The spectroscopic characterization of the artificial TATA box embedded in the MIP confirmed that the use of the 5'-TATAAA-3' template for its molecular imprinting via Watson-Crick nucleobase pairing[85] enables exposing the sugar-phosphate backbone of the imprinted 5'-TATAAA-3' template for this backbone interaction with amino acids. Herein, the MIP film was used to serve as a matrix of an artificial TATA box containing the 5'-TATAAA-3' promoter, which can be recognized by compartmentalized amino acids interacting with the natural TATA box. For that, both PM and SPR spectroscopy measurements was used under FIA conditions. In this study, 0.2 M aqueous solution samples of just one amino acid, namely, either L-serine (Ser), L-lysine (Lys), L-glutamic acid (Glu), L-threonine (Thr), L-valine (Val), L-phenylalanine (Phe), or L-leucine (Leu) were consecutively injected to the FIA system (Table 3.1-5). These amino acids recognize the 5'-TATAAA-3' promoter in the natural TATA box.[52-53] The PM determined mass of the amino acid interacting with the MIP film (Table 3.1-5) provided the number of amino acid molecules interacting with one artificial 5'-TATAAA-3' promoter molecule of the artificial TATA box embedded in the MIP. The number of amino acid molecules per one nucleobase moiety in the 5'-TATAAA-3' of the natural TATA box varied in the range of 2 to 7.[52-53]

Considering the natural TATA box as a binding site for the TBP, we took into account TBP amino acids interaction, separately, with sugar-phosphate and nucleobase moieties of the 5'-TATAAA-3' promoter.[52-53]

Herein, molecular imprinting of non-labeled 5'-TATAAA-3' resulted in a stable hexameric dsDNA analogue with sequence-controlled nucleobases. Moreover, in the herein prepared artificial ODN, the DNA sugar-phosphate backbone was replaced by the *hexa*[bis(2,2'-bithien-5-yl)] backbone, thus resulting in a stable DNA analogue. Phosphate residues of the 5'-TATAAA-3' template were left unbound during the imprinting. Thus, their bond vibrations were identified in the PM-IRRAS spectra. Although the artificial TATA box was prepared in the MIP, it could mimic activity of the natural TATA box because it contained the 5'-TATAAA-3' hybridized with the artificial *hexa*[bis(2,2'-bithien-5-yl)] TTTATA.

The main TBP moiety interacting with the phosphate moiety of the natural 5'-TATAAA-3' contains Ser and Lys.[52-53] Both directly and indirectly, these amino acids interact with six 5'-TATAAA-3' phosphate residues to form six direct hydrogen bonds and one water-mediated hydrogen bond.[52-53] In case of our present artificial TATA box, one spherical Ser molecule and six elongated Lys molecules interacted with one and six phosphate residues, respectively, similarly as in the natural TATA box (Table 3.1-5).

Taking into account the amino acid molecule diameter and assuming tight face-centered cubic (fcc) packing of the 5'-TATAAA-3' molecules on the electrode surface, we estimated the number of amino acid moles per one 5'-TATAAA-3' monolayer (Table 3.1-5). Then, we evaluated the depth of amino acid penetration into the MIP film (Figure 3.1-14a). The 5'-TATAAA-3' concentration in the 140-nm thick MIP film was 2.1 mM, as determined using the earlier developed procedure.[145] The MIP film roughness, expressed as the relative surface area, $R_{SA} = 2.8(\pm0.2)$ nm, was relatively low.[145] The number of MIP monolayers, which the studied amino acid molecules penetrated, well correlated with the mass of the amino acid interacting with the MIP (Table 3.1-5). That is, the resonance frequency change of the Au-QCR electrode coated with the MIP-(5'-TATAAA-3') film increased for the amino acid more, the deeper the amino acid molecule penetrated into the MIP film (Figure 3.1-14a). Apparently, the Ser molecule permeated as deeply as through over ten MIP monolayers (Table 3.1-5) while the Lys molecule permeated merely through less than one-and-a-half monolayer.

Chemical properties of the amino acids govern their affinity toward the TATA box (Table 3.1-5). Polar interactions of Thr are afforded by the hydrogen bond involving

the N3 atom of A.[52-53] This atom is not engaged in the Watson-Crick nucleobase pairing.   Vibrations of the C=N3 bond are seen in the PM-IRRAS spectra (Figure 3.1-8). In the natural TATA box, two Thr molecules donate one hydrogen bond to the N3 atoms of two A moieties of TATA.[52-53]

Furthermore, molecules of amino acids are mainly inserted between dsDNA base pairs, thus distorting the DNA duplex.[52-53] This is because of a large surface contact of the amino acid molecules with this duplex. Prevailingly, the DNA is hydrophobic with the van der Waals contact to sugar moieties.   Among the amino acids interacting through non-polar forces are Val, Phe, and Leu. Their non-polar sites are in contact not only with the deoxyribose moieties but also with polar nucleobases of the dsDNA. Similarly as for the natural TATA box, one monolayer of the (5'-TATAAA-3')-templated MIP interacted herein with six hydrophobic Val molecules.   Thus, the resonance frequency decrease was substantial for this interaction (Table 3.1-5). On the contrary, the hydrophobic isobutyl substituent of Leu hindered interaction of this amino acid with the adjacent nucleobases in the central part of the artificial TATA box. Therefore, the resonance frequency did not change much (not shown).

Structural studies of the TATA box have indicated conserved kinks.[54] However, stability of these deformations upon nucleobase stacking is not well known.   Therefore, we explored stacking interactions of nucleobase steps of our artificial TATA box with the aromatic ring of Phe.

In the natural TATA box, four Phe molecules wedge between the first two and the terminal two nucleobase pairs of the TATA box without hydrogen bond formation.[52-53] Herein, we assumed that Phe can interact only with the 3'- end of 5'-TATAAA-3' of the artificial TATA box, similarly as with the natural TATA box. Surprisingly, Phe strongly interacted with the artificial TATA box (Table 3.1-5) although it permeated only through four outermost MIP monolayers (Figure 3.1-14a).   This result is in agreement with those of earlier studies indicating that the Phe aromatic ring did not penetrate deeply into the stacked base pair of the TA/TA step.[146] Two Phe molecules interactions with nucleobases distort stacking at two dinucleotide step sites.[146] Herein, structure of the artificial TATA box containing the TA/TA step was modeled (Figure 3.1-15).   Apparently, it was similar to that of the natural dsDNA containing nucleobases steps. Our calculations confirmed that the Phe aromatic ring[146] interacted via stacking with nucleobases of the artificial TATA box embedded in the MIP (Figure 3.1-16a). Moreover, the TA/TA step of the artificial TATA box with two Phe

94

**Table 3.1-5.** Interactions of amino acids with an artificial TATA box.

Amino acid	QCM resonance frequency change, Hz	Mass of amino acid interacting with the MIP-(5'-TATAAA-3') film, ng	Number of amino acid molecules per one natural TATA box[53]	Number of amino acid molecules per one MIP-(5'-TATAAA-3') monolayer ($\times 10^{12}$)
L-Glutamic acid (Glu)	-22	19.1	1	4.4
L-Serine (Ser)	-17	14.7	1	8.8
L-Lysine (Lys)	-22	19.1	6	31
L-Threonine (Thr)*	-7.5	6.5	3	13
L-Valine (Val)*	-15	13.0	6	26
L-Phenylalanine (Phe)	-20	17.3	2	17

*Inter-nucleobase pair hydrogen bonds between thymine and adenine of both strands for the TA/TA step.
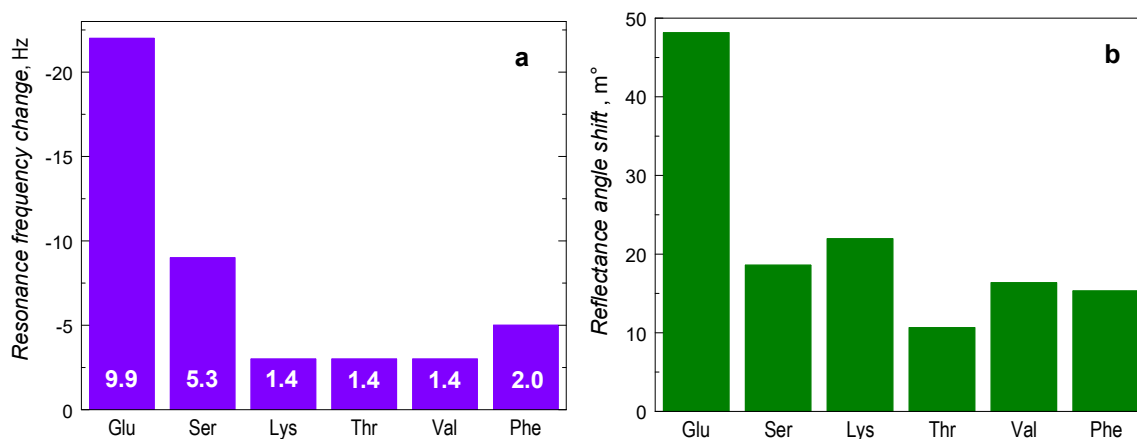
Figure 3.1-14. Histograms of amino acids interaction with the artificial TATA box. The signal of (a) PM and (b) SPR for one TATA box molecule of the MIP-(5'-TATAAA-3') film interacting with one molecule of L-glutamic acid (Glu), L-serine (Ser), L-lysine (Lys), L-threonine (Thr), L-valine (Val) and L-phenylalanine. (a) Numbers in columns indicate how many outermost MIP monolayers the amino acids molecules penetrated through. (b) The MIP-(5'-TATAAA-3') film was deposited on (a) the Au-QCR electrode or (b) the Au-coated glass slide by potentiodynamic electropolymerization of functional monomers **10** and **11** and the cross-linking monomer **14** in the presence of the 5'-TATAAA-3' template in the solution of the acetonitrile-to-water-to-toluene-to-isopropanol volume ratio of 7.5 : 1.0 : 1.0 : 0.5, respectively.
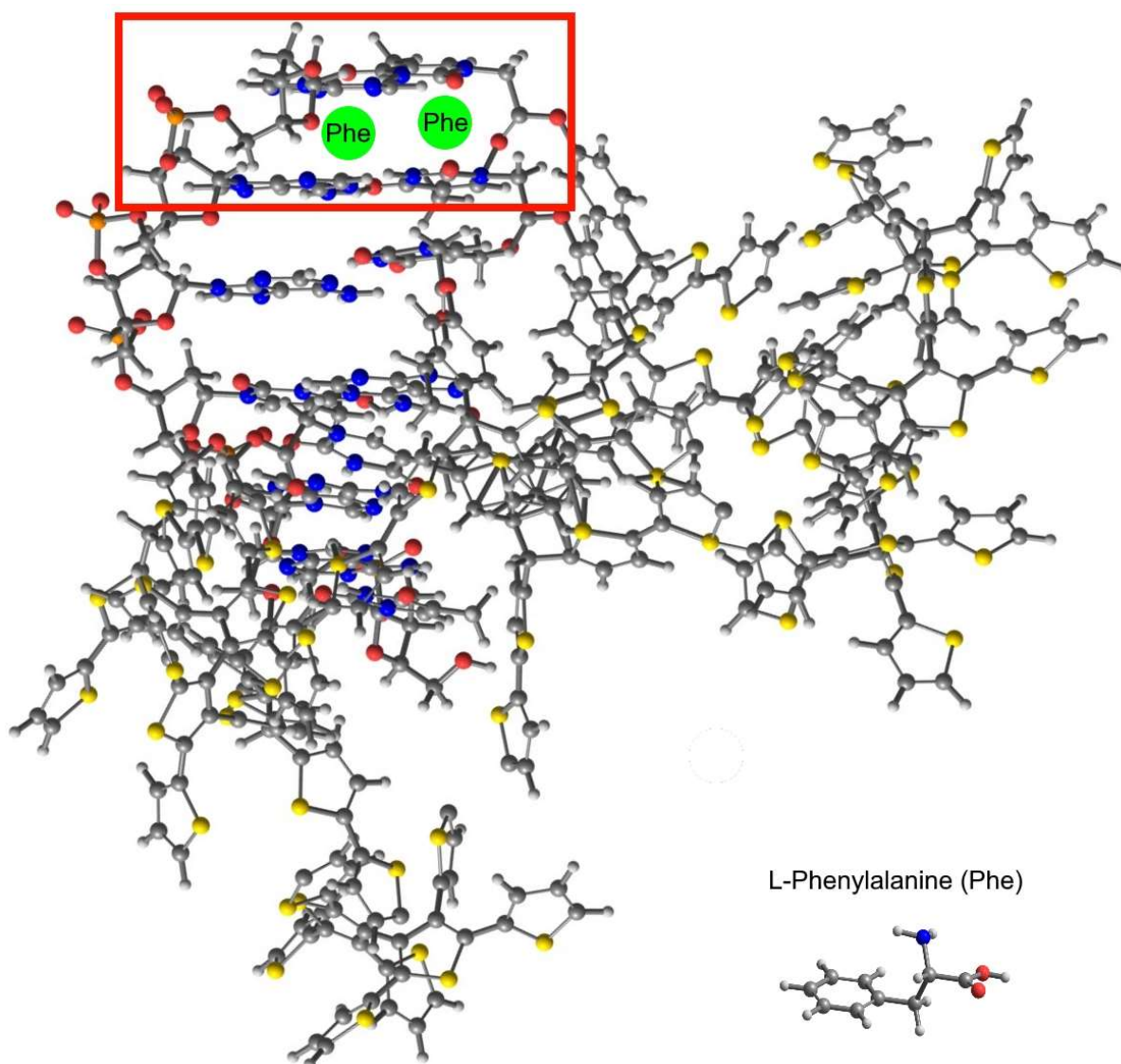
Figure 3.1-15. The artificial TATA box structure visualized using Avogadro program package.[149] In the red frame, the green circles represent two L-phenylalanine (Phe) molecules inserted in the TA/TA step of the artificial TATA box.

molecules inserted was optimized (Figure 3.1-16b). This was accomplished to demonstrate distortion of stacking interaction between nucleobases of our artificial TATA box. Thus, the Phe ring was intercalated between two nucleobase pair stacks, i.e., between nucleobase pair steps. If this assumption holds, then Phe can serve as a hydrophobic anchor of the (transcription factor)-TBP interaction, thus effectively stimulating the transcription.[54,136,144,146-148]

In the natural TATA box, one Glu molecule indirectly interacts with the A moiety of the 5'-TTTATA-3' strand of the TATA box.[142,144] Herein, also the Glu molecule was found to interact strongly with the A moiety of the *hexa*[bis(2,2'-bithien-5-yl)] TTTATA analogue in our artificial TATA box (Table 3.1-5). Moreover, the Glu

molecule penetrated as deeply as through nearly ten MIP monolayers (Figure 3.1-14a). Thus, these results agree with results of previous studies of dsDNA-protein interactions at the molecular level.[142] Apparently, the artificial TATA box embedded in the MIP was available for compartmentalization of amino acids, similarly to that of the natural TATA box.

a

b
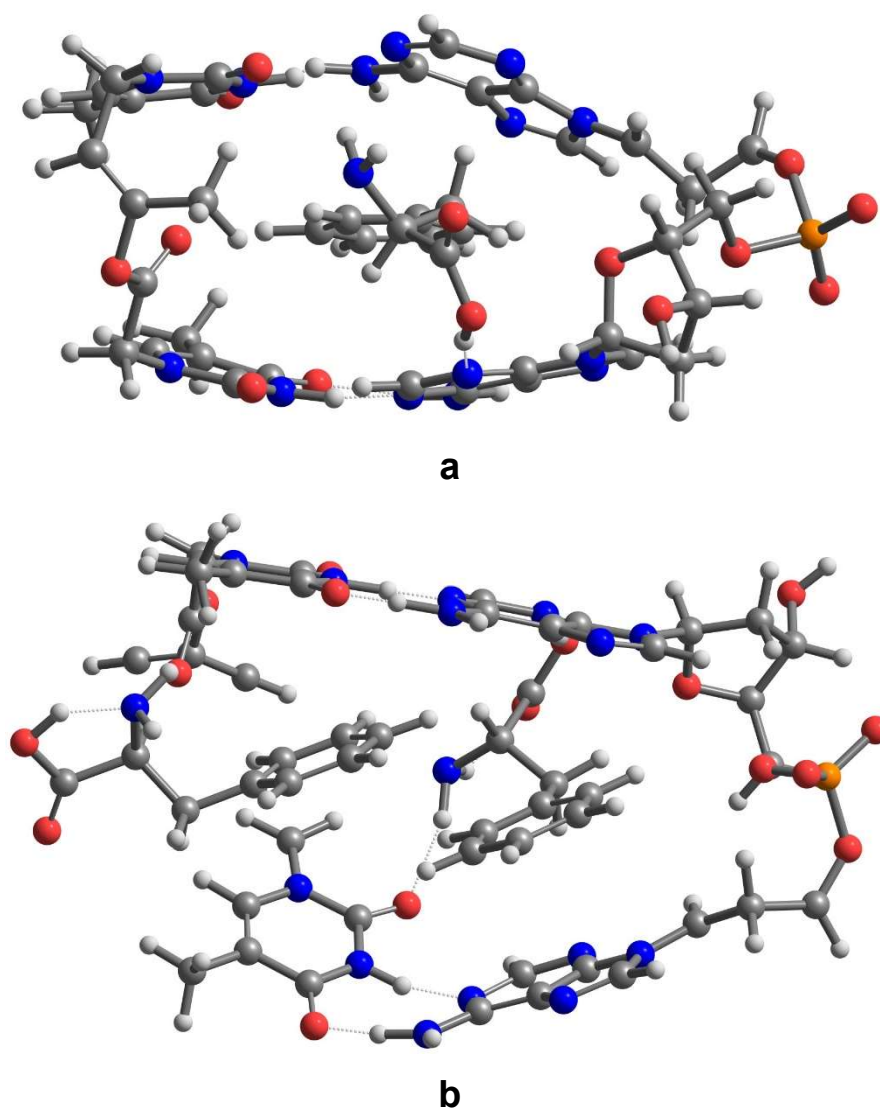
Figure 3.1-16. The optimized structure of the TA/TA step with intercalated (a) one and (b) two L-phenylalanine (Phe) molecules. The modeled structure of the TA/TA step of the artificial TATA box is similar to that of nucleobases steps of natural dsDNA. The ultrafine geometry optimization was performed using the dispersion-corrected DFT with wb97xd[150] potential, which describes π-π stacked structures and the standard base 3-21g.

Conformably, SPR results for the chip coated with the MIP-(5'-TATAAA-3') film interacting with these amino acids were in accord to the PM results (Figure 3.1-14b).

The PM and SPR results were encouraging, especially those related to the Glu molecule penetration into the MIP. Introduction of a single-negatively charged Glu residue into a potentially hydrophobic membrane-lytic peptide selectively perturbs the endosomal membranes and facilitates the cytosolic release of endocytosed biomacromolecules.[151] Therefore, Glu penetration was examined into the MIP film. For this, the Glu interface with the MIP-(5'-TATAAA-3') was examined using the XPS depth profiling. Moreover, relative elemental composition of the MIP-(5'-TATAAA-3') film after 24-h soaking in 20 mM Glu was determined using this analysis. The artificial TATA box interactions with Glu were readily recognized by following the relative content of nitrogen (N 1s) and phosphorus (P 2p) as a function of the Ar^+ sputtering time (Table 3.1-6).

Table 3.1-6. Elemental depth-dependent composition of the MIP-(5'-TATAAA-3') film after 24-h immersing in 20 mM L-glutamic acid (Glu), determined from the high-resolution XPS spectra recorded using the depth-profiling analysis.[a]

Element	Elemental composition, atomic %		
	MIP-(5'-TATAAA-3') at the depth of 0 nm	MIP-(5'-TATAAA-3') at the depth of 10 nm	MIP-(5'-TATAAA-3') at the depth of 20 nm
C	80.1	79.7	79.9
O	9.8	8.4	8.7
S	7.6	8.4	8.1
N	2.2	3.2	3.1
P	0.2	0.1	0.1

[a] The MIP-(5'-TATAAA-3') film was deposited on the Au-coated glass slide by potentiodynamic electropolymerization of the functional monomers **10** and **11** and the cross-linking monomer **14**, in the presence of the 5'-TATAAA-3' template, in the solution of the acetonitrile-to-water-to-toluene-to-isopropanol volume ratio of 7.5 : 1.0 : 1.0 : 0.5, respectively.

The nitrogen-to-phosphorus atomic per cent ratio on the surface of the MIP-(5'-TATAAA-3') film increased by ~1.6 times after film immersing in the Glu solution (Figure 3.1-17). Furthermore, this ratio was 4.7 and 5.7 times larger in the 10-nm and 20-nm depth of the film, respectively, than those at these depths for the MIP film before exposing it to Glu (Figure 3.1-17). Apparently, Glu permeated through the examined layers of the homogeneous MIP-(5'-TATAAA-3') film. Noteworthy, the phosphorus and nitrogen relative content slightly decreased and significantly increased,

respectively, with the increase of the depth of penetration. Hence, clearly, any contribution to the nitrogen content increase arose from the amine group of Glu and not from the nucleobases. Evidently, the Glu presence in the MIP-(5'-TATAAA-3') was significant. So, we have successfully demonstrated that high-resolution XPS combined with depth profiling offered a valuable nanoscale tool for analysis of the depth dependent Glu interactions with the artificial TATA box in the multilayered MIP-(5'-TATAAA-3') film.

Two types of interactions, namely, hydrogen bonding and aromatic ring stacking, determine the nucleic acid structure. Hydrogen bonding is important in the DNA-protein recognition. In DNA-protein complexes, most of hydrogen bonds are formed with the Hoogsteen edge of nucleobases. Typically, this is because, the Watson–Crick edges are unavailable, being engaged in nucleobase pairing.[152] Small aromatic molecules, which intercalate into the dsDNA helix, can impart this helix damage. Intermolecular interactions involving aromatic rings are of paramount importance in biological recognition.[153] Their understanding is essential for rational drug design in medicinal chemistry. Different investigations, such as biological studies, molecular recognition studies using artificial receptors, crystallographic database mining, gas-phase studies, and theoretical calculations, are pursued to gain a profound understanding of the structural and thermodynamic parameters of individual recognition modes involving aromatic rings.[153] Herein, the analytical approach using a stable artificial DNA fragment, namely, an artificial TATA box, was proposed for understanding the principle role of nucleobase sequence specificity. Besides, DNA sequence-specific recognition is critical in DNA repairing, especially in the context of DNA-protein interaction.
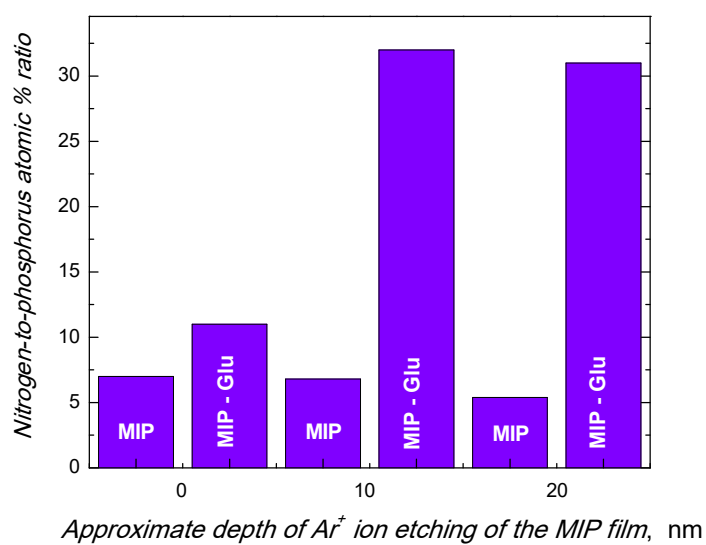
Figure 3.1-17. The nitrogen-to-phosphorous atomic % ratio for the MIP-(5'-TATAAA-3') film before and after 24-h immersing in 20 mM L-glutamic acid (Glu), labeled as MIP-Glu, at different depths of profiling.

## 3.2 MIP chemical sensor for selective 5'-GCGGCGGC-3' determination

3.2.1 Complexation of the PNA H₂N(CO)GCGGCGGC-NH₂ template and functional monomers via guanine-cytosine nucleobase pairing

For synthesis of the (PNA H$_2$N(CO)GCGGCGGC-NH$_2$)-templated MIP film, PNA H$_2$N(CO)GCGGCGGC-NH$_2$ **7** (Table 2.1-2) was used as the template, around which 4-bis(2,2'-bithien-5-yl)methylphenyl-2-guanine ethyl ether **12** (Table 2.1-3) and 2-(cytosin-1-yl)ethyl 4-bis(2,2'-bithien-5-yl)methylbenzoate **13** (Table 2.1-3) functional monomers arranged by assuming positions governed by the complementary nucleobase pairing Watson-Crick rule. To confirm experimentally the stoichiometry and thermodynamics of arrangement of **12** and **13** around **7**, ITC measurements were performed.

First, 0.030 mM **7** in DMSO was titrated with 0.70 mM **12** in DMSO (Figure 3.2-1a). The heat evolved during complexation was relatively small (ΔH = -3.7 kJ mol^{-1}). An independent model was chosen and a theoretical isotherm was fitted to the ITC data acquired (Figure 3.2-1b) yielding the complex stability constant (K_s = 1.5×10^5 M^{-1}) and the entropy change (ΔS = 86.7 J mol^{-1} K^{-1}) as well as the expected complex stoichiometry (**12** : **7** = 3 : 1). From the enthalpy and entropy changes, the Gibbs free energy change of complex formation was calculated (ΔG = -29.5 kJ/mol).

In the second ITC experiment, 0.075 mM **7** in DMSO was titrated with 4.0 mM **13** in DMSO (Figure 3.2-2a). Then, the ITC data acquired were fitted with a theoretical isotherm of the multiple sites model (Figure 3.2-2b). Apparently, there were two distinct steps in the isotherm derived (Figure 3.2-2b). These steps indicated that, first, three, and then two molecules of **13** were consecutively attached to the PNA molecule. First, three molecules of **13** strongly bound one molecule of **7** (Figure 3.2-2b) forming a relatively stable complex (K_s = 10^7 M^{-1}). The negative entropy change determined, (ΔS = -206.0 J mol^{-1} K^{-1}), corresponding to this complexation, was most likely due to the PNA pre-organization induced by the formation of nine strong hydrogen bonds of three complementary G-C pairs. Fortunately, the negative enthalpy change (ΔH = -102.0 kJ mol^{-1}) was sufficiently high to overcompensate for the strongly unfavorable loss in conformational entropy,

thus resulting in the negative Gibbs free energy change because of this complexation (ΔG = -40.61 kJ mol^{-1}).
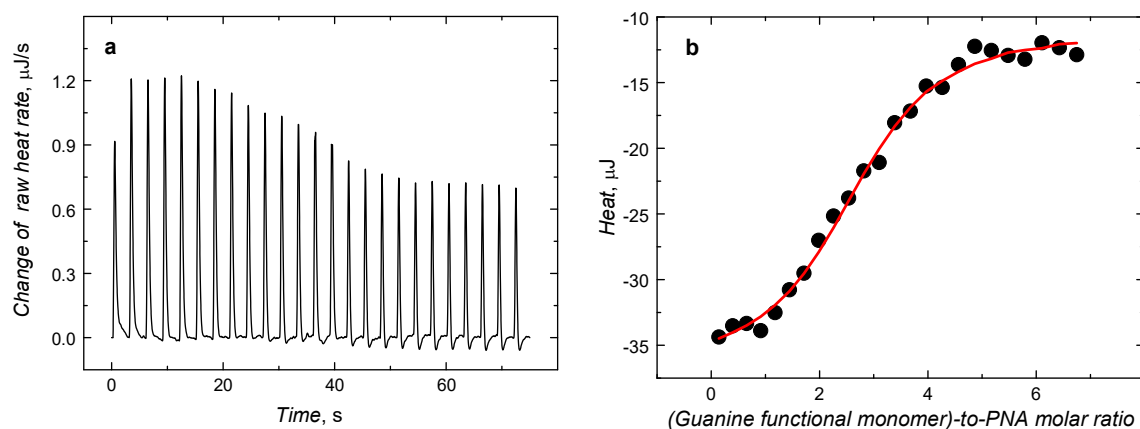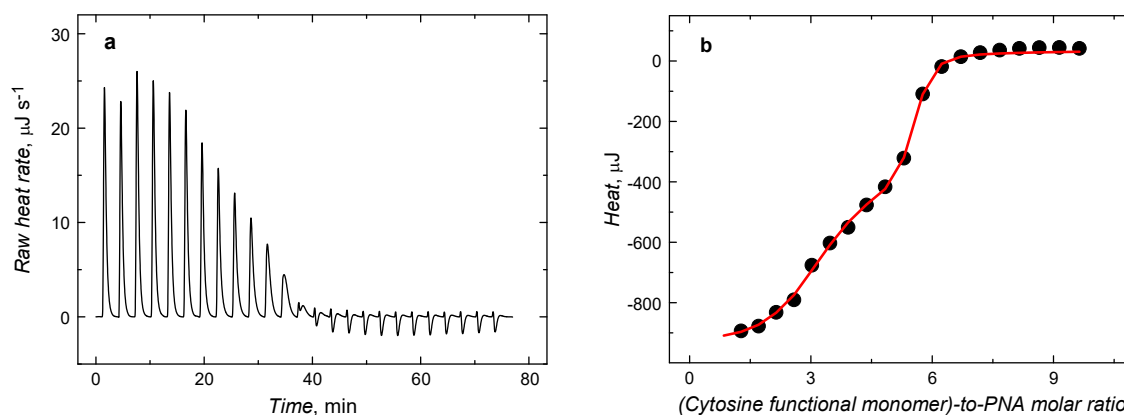

Figure 3.2-1. (a) The ITC raw heat rate change with time involving addition of 8-µL aliquots of 0.70 mM guanine functional monomer **12** in DMSO to 30 µM PNA H$_2$N(CO)GCGGCGGC-NH$_2$ **7** in DMSO at 3-min intervals. (b) The binding isotherm for this titration; the curve represents the least-square fit of an independent model to the experimental data acquired.

Next, two more molecules of **13** were attached to PNA H$_2$N(CO)GCGGCGGC-NH$_2$ **7** (Figure 3.2-2b) incurring additional adjustment of conformation of the G binding sites of the PNA. This PNA structure reorganization yielded only slightly negative entropy change (ΔS = -1.0 J mol^{-1} K^{-1}), thus leading to formation of the considerably stable complex (K_s = 8.96×10^5 M^{-1}). Apparently, the six more hydrogen bonds formed between **13** and two G binding sites of PNA in the **7-13** complex were also energetically favorable, although they were formed with a slightly lower negative enthalpy change (ΔH = -34.3 kJ mol^{-1}). Owing to these enthalpy-dominated effects, all five available guanine binding sites of **7** were recognized by the cytosine moieties of **13**, thus successfully forming the pre-polymerization complex.

However, quite different results brought the ITC experiment of the **7** titration with the C nucleobase (Figure 3.2-3). In this experiment, 0.075 mM **7** in DMSO was titrated with 4.0 mM C in DMSO (Figure 3.2-3a). After fitting the independent model to the ITC data acquired (Figure 3.2-3b), thermodynamic parameters and stoichiometry of the complex formed were calculated. Surprisingly, the molar ratio of **7** to cytosine appeared to be 1 : 3. The entropy change was positive (ΔS = 17.0 J mol^{-1} K^{-1}), thus favorably contributing to the Gibbs free energy change of complex formation (ΔG = -28.77 kJ mol^{-1}). Moreover, this positive entropy change revealed

102

that, most plausibly, C did not induce any conformational changes at the binding sites of **7**. Therefore, only three C molecules could bind one molecule of **7** with a relatively high stability constant ($K_s = 10^5$ M^{-1}). However, this constant was lower than that of the complex of 7 with C functional monomer **13**.

Figure 3.2-2. (a) The ITC raw heat rate change with time involving addition of 8-μL aliquots of 4.0 mM cytosine functional monomer **13** in DMSO to 75 μM PNA **7** in DMSO at 3-min intervals. (b) The binding isotherm for this titration; the curve represents the least-square fit of a multiple sites model to the data points acquired.

Figure 3.2-3. (a) The ITC raw heat rate change with time involving addition of 8-μL aliquots of 4.0 mM cytosine in DMSO to 75 μM PNA in DMSO at 3-min intervals. (b) The binding isotherm for this titration; the curve represents the least-square fit of an independent model to the data acquired.

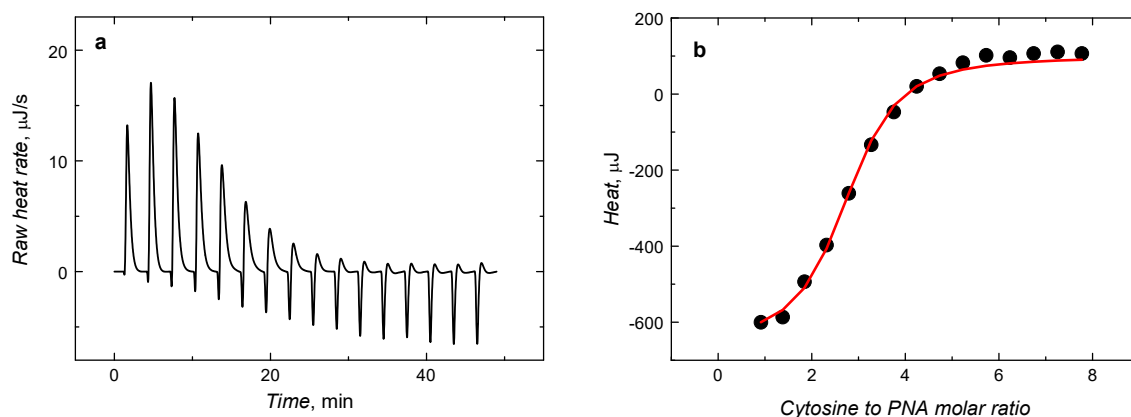The ability of the C moiety of **13** to recognize G selectively was further verified by titrating the mismatched PNA octamers, namely, PNA H$_2$N(CO)GC**T**GC**T**GC-NH$_2$ **8** (Table 2.1 2) and PNA H$_2$N(CO)GCGA**TC**GC-NH$_2$ **9** (Table 2.1-2), with **13**, as shown in Figure 3.2-4 and Figure 3.2-5, respectively. In each of these titrations,

the determined 3 : 1 stoichiometry of the complex corresponded to the number of G substituents in the mismatch PNA octamer equal to 3.
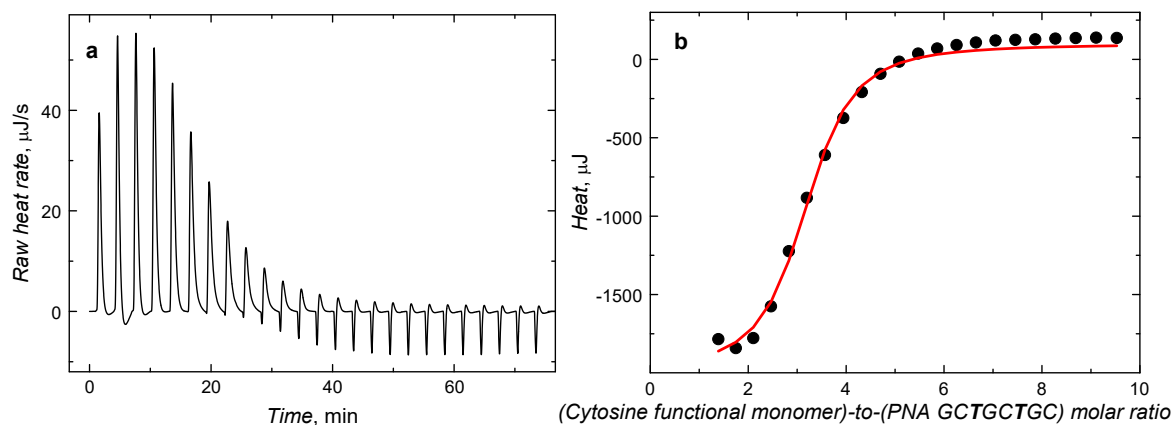

Figure 3.2-4. (a) The ITC raw heat rate change with time involving addition of 8-μL aliquots of 4.0 mM cytosine functional monomer **13** in DMSO to 75 μM PNA H$_2$N(CO)GC**T**GC**T**GC-NH$_2$ **8** in DMSO at 3-min intervals. (b) The binding isotherm for this titration; the curve represents the least-square fit of an independent model to the data acquired.

To conclude, the designed and synthesized 2,2'-bithien-5-yl functional monomers bind the PNA H$_2$N(CO)GCGGCGGC-NH$_2$ **7** template according to the complementary nucleobase pairing rule, however, through different equilibrium states. Surprisingly, **13** can accelerate activation of PNA H$_2$N(CO)GCGGCGGC-NH$_2$ by inducing its conformational changes. PNA H$_2$N(CO)GCGGCGGC-NH$_2$ bound by **13** slowly rearranged structurally, thus resulting in equilibrium between two main PNA H$_2$N(CO)GCGGCGGC-NH$_2$ conformations. This reorganization was necessary to bind all possible G sites of the PNA H$_2$N(CO)GCGGCGGC-NH$_2$ by C functional monomers as well as to obtain a high stability constant of the resulting complex. This extraordinary mechanism of PNA complexation by the C functional monomer can promote the latter complex oligomerization to more stable 2,2'-bithien-5-yl ODN analogue in the MIP.

3.2.2 Preparation of the (PNA H$_2$N(CO)GCGGCGGC-NH$_2$)-templated MIP film and its deposition on different electrodes by electropolymerization

According to the complex stoichiometry determined by ITC measurements, a mixed solvent solution for potentiodynamic electropolymerization of 0.02 mM PNA H$_2$N(CO)GCGGCGGC **7**, 0.06 mM **12**, 0.1 mM **13** 0.1 mM **14**, and 0.1 M

104

(TBA)ClO$_4$ at the acetonitrile-to-water volume ratio of 9 : 1 was prepared. By taking advantage of electroactivity of the bis(2,2-bithen-5-yl) moiety, the pre-polymerization complexes were transferred from solution into the MIP film, deposited on the electrode surface, via five potential cycles, within a few minutes. The Pt disk, Au-glass slide, and SPR
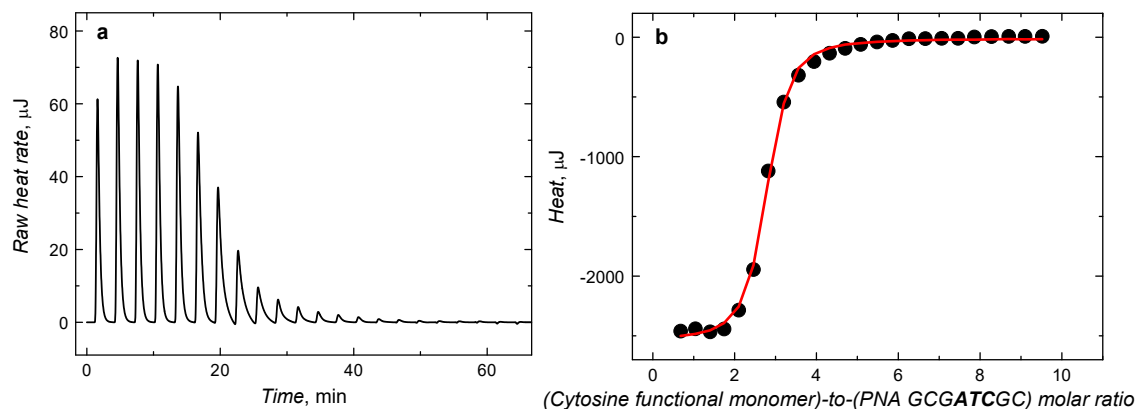

Figure 3.2-5. (a) The ITC raw heat rate change with time involving addition of 8-µL aliquots of 4.0 mM cytosine functional monomer **13** in DMSO to 75 µM PNA H$_2$N(CO)GCG**ATC**GC-NH$_2$ **9** in DMSO at 3-min intervals. (b) The binding isotherm for this titration; the curve represents the least-square fit of an independent model to the data acquired.

Au-glass disk electrodes were used. Two anodic peaks appeared during the initial positive potential scan (solid curve in Figure 3.2-6a). The less positive peak, originally present at ~1.02 V, vanished in the two last cycles. The more positive peak, initially present at ~1.13 V, shifted positively in subsequent cycles. Apparently, the initially deposited MIP layer played the role of a resistive barrier for deposition of subsequent MIP layers, thus hindering further electro-oxidation of the monomers present in the solution.

However, none of these anodic peaks corresponded to PNA H$_2$N(CO)GCGGCGGC **7** template electro-oxidation. Although the **7** template is rich in G, which is the most redox-active nucleobase,[154] the G moiety stayed in its intact form during present potential cycling (dash curve in Figure 3.2-6a). Apparently, the recorded herein anodic peaks originated from electro-oxidation of thiophene moieties of functional monomers **12** and **13**, and the cross-linking monomer **14**. This is because they were also present in multi-cycle potentiodynamic curves of all cycles corresponding to electropolymerization in the **7** absence (Figure 3.2-6b), which led to deposition of the corresponding NIP film.

105
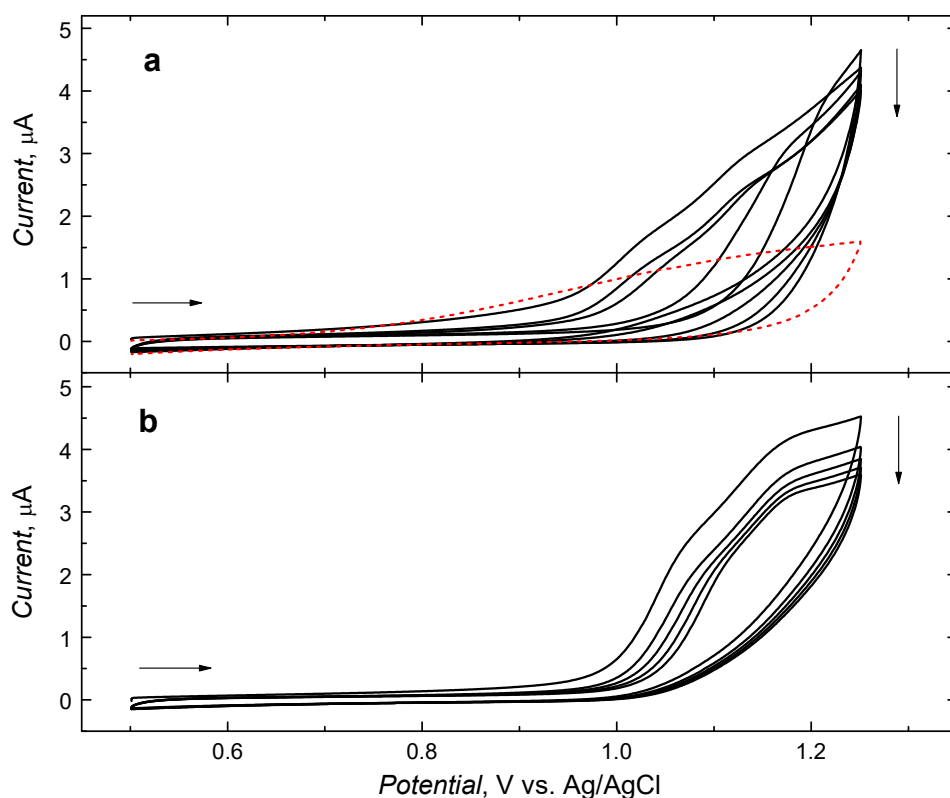
Figure 3.2-6. (Panel a, dash curve) The potentiodynamic curve for 0.05 mM PNA H$_2$N(CO)GCGGCGGC-NH$_2$ in 0.1 M (TBA)ClO$_4$ in the acetonitrile-water, 9 : 1 (*v* : *v*), solution recorded at the 1-mm diameter Pt disk electrode. (Panel a, solid curve) The multi-cycle potentiodynamic curve for simultaneous electropolymerization and deposition on the Pt disk electrode of the (PNA H$_2$N(CO)GCGGCGGC-NH$_2$)-templated MIP film from 0.02 mM PNA H$_2$N(CO)GCGGCGGC-NH$_2$, 0.06 mM **12**, 0.1 mM **13** and 0.1 mM **14** in 0.1 M (TBA)ClO$_4$, in acetonitrile-water 9 : 1 (*v* : *v*), solution. The potential scan rate was 50 mV s^{-1}. (b) The multi-cyclic potentiodynamic curve for simultaneous electropolymerization and deposition of the corresponding NIP film from 0.06 mM **12**, 0.1 mM **13** and 0.1 mM **14** in the 0.1 M (TBA)ClO$_4$ acetonitrile-water, 9 : 1 (*v* : *v*), solution.

3.2.3 Efficiency of programmable PNA templating, and then extracting from the MIP film

After electropolymerization, the PNA H$_2$N(CO)GCGGCGGC-NH$_2$ **7** template was extracted from the MIP film in order to vacate imprinted cavities and make them available for the 5'-GCGGCGGC-3' analyte molecules. For that, PNA H$_2$N(CO)GCGGCGGC-NH$_2$ **7** was extracted at a relatively high temperature of 60 °C. In a relatively basic solution of pH > 10, G is deprotonated to form its negatively charged conjugated nucleobase. Hydrogen bonding in the G-C pair is then ruptured, thus leading to dehybridization of the duplex of

106

PNA $H_2N(CO)GCGGCGGC-NH_2$ with the cavity ligand. Moreover, the temperature increase of 25 to 60 °C accelerated this dehybridization, thus allowing the template removal time shortening from 3 to 1 h, respectively. This dehybridization was verified by the XPS, DPV, and EIS measurements described below.

In the XPS core-level spectra of the (PNA $H_2N(CO)GCGGCGG-NH_2$)-templated MIP film before, and then after template extraction as well as of the corresponding NIP film, the nitrogen-to-sulfur (N-to-S) atomic per cent ratio was estimated (Table 3.2-1). The nitrogen-rich PNA template additionally enriched the MIP film with nitrogen. Therefore, the N-to-S ratio, expectedly higher than that in the NIP film, confirmed PNA $H_2N(CO)GCGGCGGC-NH_2$ templating in the MIP film during electropolymerization. The determined N-to-S ratio for this film (Table 3.2-1) was close to that of 2.0 expected for the pre-polymerization complex. Then, after template extraction, the determined ratio decreased (Table 3.2-1) to the value corresponding to both the determined and calculated N-to-S atomic per cent ratio for the NIP film of ~0.5 (Table 3.2-1). Apparently, PNA $H_2N(CO)GCGGCGGC-NH_2$ was entrapped in the MIP during the electropolymerization, and then released during the extraction.

Table 3.2-1. Surface content of the nitrogen and sulfur elements in the (PNA $H_2N(CO)GCGGCGGC-NH_2$)-templated MIP film before and after template extraction, and in the NIP film, as well as the nitrogen-to-sulfur (N-to-S) ratio determined using the high-resolution XPS analysis.

Polymer film	Nitrogen content atomic %	Sulfur content atomic %	Nitrogen-to-sulfur ratio atomic %
MIP[a] before extraction	4.47	2.58	1.7
MIP[a] after extraction	3.46	9.27	0.4
NIP[b]	4.92	10.08	0.5

[a] The (PNA $H_2N(CO)GCGGCGGC-NH_2$)-templated MIP film was deposited on the Au coated glass slide by potentiodynamic electropolymerization of the functional monomers **12** and 1**3**, and the cross-linking monomer **14** in the presence of the PNA GCGGCGGC template in the solution of the acetonitrile-to-water volume ratio of 9 : 1.

[b] The NIP film was deposited on the Au coated glass slide by potentiodynamic electropolymerization of the functional monomers **12** and 1**3** and the cross-linking monomer **14** in the solution of the acetonitrile-to-water volume ratio of 9 : 1.

Moreover, DPV was used for indirect estimation of the PNA $H_2N(CO)GCGGCGGC-NH_2$ presence, and then absence, in the MIP film before

and after extraction, respectively. In this measurements, the redox marker of 0.1 M $[Fe(CN)_6]^{4-}/[Fe(CN)_6]^{3-}$ was used. The DPV experiments resulted in different heights of the oxidation peaks of the marker, which depended upon ability of the marker diffusion through the film (Figure 3.2-7).
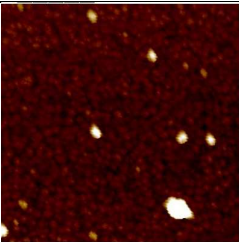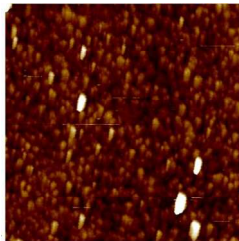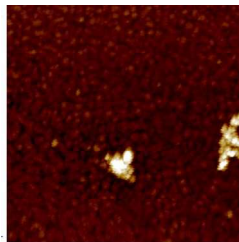
In the first experiment, the template molecules occupying cavities prevented diffusion of the marker to the electrode surface through the film. Therefore, the DPV peak for the marker was hindered (curve *1* in Figure 3.2-7). Then, it increased more the more cavities were emptied in the course of template extraction (curves *2-4* in Figure 3.2-7). Apparently, the redox marker diffused fast through the MIP film with empty cavities. Next, after immersing this film in 20 µM PNA $H_2N(CO)GCGGCGGC-NH_2$ for 15 min, the DPV peak decreased because PNA molecules entered the cavities, thus hindering diffusion of the marker (curve *5* in Figure 3.2-7).
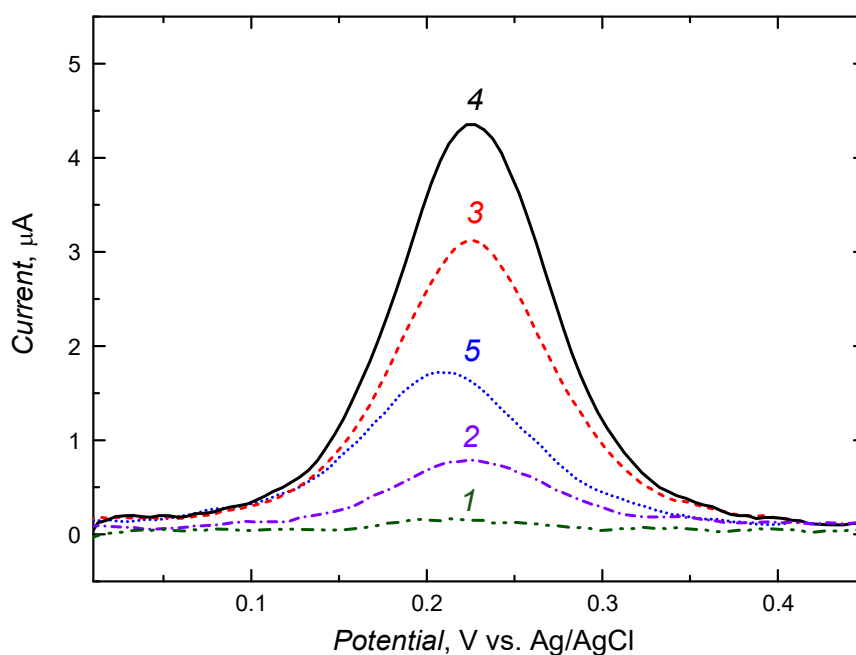
Figure 3.2-7. Differential pulse voltammograms for 0.1 M $[Fe(CN)_6]^{4-}$ and 0.1 M $[Fe(CN)_6]^{3-}$ in 0.1 M PBS (pH = 7.4) at the 1-mm diameter Pt disk electrode coated with the (PNA $H_2N(CO)GCGGCGGC-NH_2$)-templated MIP film (*1*) before and after (*2*) 15, (*3*) 45, and (*4*) 60 min of template extraction with 0.1 M trimethylamine (pH = 12.0) at 60 °C, and then (*5*) after immersing the electrode in 20 µM PNA $H_2N(CO)GCGGCGGC-NH_2$ for 15 min. The film was prepared by potentiodynamic electropolymerization in the potential range of 0.50 to 1.25 V vs. Ag|AgCl at a 50 mV s^{-1} scan rate. The potential step, pulse amplitude, and pulse duration in the DPV experiments was 5 mV, 50 mV, and 100 ms, respectively.

The (PNA H$_2$N(CO)GCGGCGGC-NH$_2$)-templated MIP film before and after template extraction as well as the corresponding NIP film were imaged with AFM in order to unravel their morphology and determine their thickness (Table 3.2-2). Apparently, the MIP film before extraction was composed of well-defined grains, 30 to 60 nm in diameter. This film was much thicker than the corresponding NIP film. Thickness of the MIP film higher than that of the NIP film may evidence the presence of the template in the former film. Moreover, it may indicate facilitated electropolymerization of the functional and cross-linking monomers in the template presence. After extraction of the template, the MIP film thickness decreased but the size of the grains was not much affected. Apparently, the film slightly shrank, most likely because of low content of the cross-linking monomer **14** in its structure. However, high cross-linking of MIPs imprinted with macromolecules is not recommended because it may result in undesired hindering of the template removal.[78]

Table 3.2-2. Atomic force microscopy (AFM) images of different polymer films as well as the determined film thickness and grain size. Image size is (2×2) μm^2.

| Polymer film	AFM image	Film thickness, nm	Grain size, nm
MIP before extraction		151 ± 3	30-60
MIP after extraction		125 ± 3	50-70
NIP		114 ± 4	30-60

3.2.4 EIS determination of the 5'-GCGGCGGC-3' with the MIP chemosensor

The (PNA $H_2N(CO)GCGGCGGC-NH_2$)-templated MIP film, deposited on a Pt disk electrode, was used for EIS determination of 5'-GCGGCGGC-3' under stagnant-solution conditions. After removal of the template from MIP cavities, the electrode was immersed in 0.1 M PBS (pH = 7.4), which was 0.1 M in the $[Fe(CN)_6]^{4-}/[Fe(CN)_6]^{3-}$ redox marker, and then the impedance spectrum was recorded. The constructed Nyquist plot (Figure 3.2-8) consisted of a small semicircle in the high frequency range (inset I in Figure 3.2-8), which partially overlapped with a semicircle in the intermediate frequency range, and a straight line in the low frequency range. For experimental data interpretation, a modified Randles equivalent circuit was used (inset II in Figure 3.2-8). Two partially superimposed semicircles in the complex plane plot were ascribed to a porous structure of the MIP film and redox reaction of the marker, similarly as postulated in earlier studies.[155-156] Herein, the film was treated as a porous membrane containing a matrix formed by the conducting polymer and pores filled with an electrolyte solution. Hence, it was assumed to consist a mixture of two phases conducting two different species, electronic and ionic. The ionic species in the pores, flooded with an electrolyte solution, can freely be exchanged with the bulk solution at the pore's mouth. Resistance of this pore phase, marked at the equivalent circuit as R_{po}, corresponds to the resistance of ion transport in pores. The smaller semicircle represents this process. A negligibly small resistance of the solution-filled pores is constant during the measurements. The interface between the porous and continuous phase is modeled as the double-layer capacitance in parallel with the kinetically controlled charge-transfer resistance, R_{ct}. The redox reaction at the pore's wall can be described by the charge-transfer resistance, which is controlled by diffusion represented by the Warburg impedance, W. The larger semicircle is responsible for this process. Other parameters of the equivalent circuit correspond to ohmic resistance of the electrolyte solution and cell components, R_s, and the constant phase element, CPE, which describes both pseudocapacitance in a high frequency range and double-layer capacitance generated because of inhomogeneity of the phases.

Nyquist plots were constructed for the MIP chemosensor immersed for 5 min in analyte solutions of different concentrations (Figure 3.2-9a). The experimental data were fitted with electric parameters of the equivalent circuit, and then the R_{ct} values were determined. The R_{ct} was dependent upon the extent of the analyte occupation of

110

the MIP cavities, as demonstrated by the R_{ct} dependence on the ODN analyte concentration in solution (inset in Figure 3.2-9a). The chemosensor response was proportional to the analyte concentration in the 3.0 to 80 nM range (curve *1* in inset to Figure 3.2-9a). The linear regression equation and the correlation coefficient of the calibration plot was

$(R_{ct,f} - R_{ct,i})$ [Ω] = 780($\pm$9.0) [Ω] + 55.53($\pm$0.28) [Ω nM^{-1}] $c_{analyte}$ [nM]   and   0.99, respectively, where $R_{ct,i}$ and $R_{ct,f}$ is the charge-transfer resistance of the MIP film before and after 5'-GCGGCGGC-3' sample injection, respectively. The sensitivity and LOD at S/N=3 was 53($\pm$0.002) Ω nM^{-1} and 200 pM, respectively.
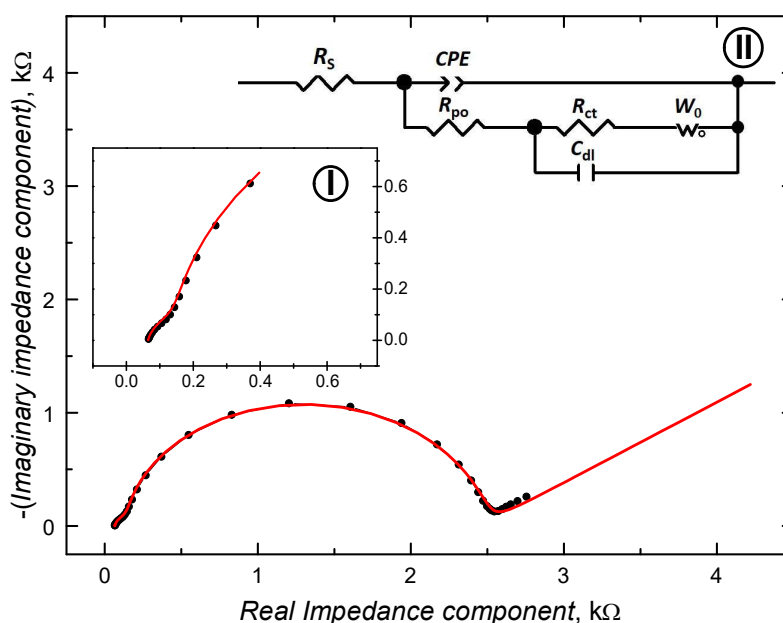
Figure 3.2-8. The Nyquist plot of the impedance spectrum for 0.1 M [Fe(CN)$_6$]$^{4-}$/[Fe(CN)$_6$]$^{3-}$ in 0.1 mM PBS (pH = 7.4) at the (PNA H$_2$N(CO)GCGGCGGC-NH$_2$)-templated MIP film coated Pt disk electrode. The fitted curve is solid. The applied potential was equal to the open circuit potential, E_{OCP} = 0.20 V vs. Ag|AgCl. Frequency was varied in the range of 200 kHz to 100 mHz at the ac amplitude of 10 mV. Inset I is a magnified small semicircle in the high frequency range. Inset II shows the equivalent circuit applied to fit the impedance spectrum.

The chemosensor selectivity with respect to interferences was determined by dividing sensitivity of the MIP film to the 5'-GCGGCGGC-3' analyte by that of the two-nucleobase mismatches, vis. 5'-GCG**AT**GGC-3' or 5'-GC**T**GC**T**GC-3' (lines *2'* and *3'* in Figure 3.2-9b) as well as the three-nucleobase mismatch, namely, PNA H$_2$N(CO)GCG**ATC**GC-NH$_2$ (line *4'* in Figure 3.2-9b). Apparently, the MIP chemosensor was ~3.0 and ~3.8 times more sensitive to the 5'-GCGGCGGC-3' analyte than to its two- and three-nucleobase mismatches, respectively. Moreover,

111

the analyte was determined at the corresponding NIP film (line *2'* in inset to Figure 3.2-9b). Its sensitivity to the analyte, 15($\pm$0.70) Ω nM^{-1}, was nearly four times lower than that of the MIP film, thus signifying that the apparent imprinting factor was, IF$\approx$4.0.

To conclude, the PNA H$_2$N(CO)GCGGCGGC-NH$_2$ template programmed and transferred the 5'-GCGGCGGC-3' sequence information into the MIP film allowing for controlled preparing the 2,2'-bithien-5-yl GCCGCCGC oligomer inside the molecular cavities. This immobilized in the MIP cavity ODN analogue was used as the probe for selective determination of the complementary 5'-GCGGCGG-3' analyte.
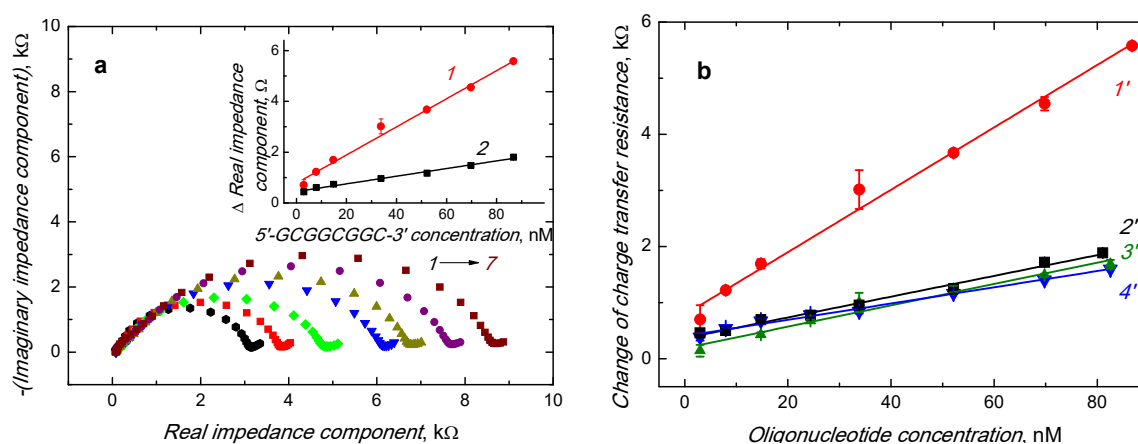
Figure 3.2-9. (a) Nyquist plots of impedance spectra for a 1-mm Pt disk electrode coated with the (PNA H$_2$N(CO)GCGGCGGC-NH$_2$)-templated MIP film after template extraction, and then immersion for 5 min in solution of the 5'-GCGGCGGC-3' analyte of different concentrations indicated at curves. Measurements were performed for 0.1 M [Fe(CN)$_6$]$^{4-}$ and 0.1 M [Fe(CN)$_6$]$^{3-}$ in 0.1 M mM PBS (pH = 7.4) at the applied potential equal to the open circuit potential, E_{OCP} = 0.20 V vs. Ag|AgCl. Inset shows calibration plots for the (*1*) 5'-GCGGCGGC-3' analyte at the (PNA H$_2$N(CO)GCGGCGGC-NH$_2$)-templated MIP film and (*2*) the corresponding NIP film. (b) Calibration plots, constructed using the data obtained by fitting electric parameters of the equivalent circuit to experimental data, for (*1'*) the 5'-GCGGCGGC-3' analyte, (*2'*) two-nucleobase mismatched 5'-GCG**AT**GGC-3', (*3'*) two-nucleobase mismatched 5'-GC**T**GC**T**GC-3', and (*4'*) three-nucleobase mismatched PNA H$_2$N(CO)GCG**ATC**GC-NH$_2$.

In view of results presented in the thesis, it can be postulated that molecular imprinting provides means to utilize the sequence programmability of ODN or PNA to prepare a stable 2,2'-bithien-5-yl oligomer designed to reveal properties of a stable ODN analogue fabricated in molecular cavities of the MIP.

3.2.5 (PNA H₂N(CO)GCGGCGGC-NH₂)-templated MIP chemosensor with the 2,2'-bithien-5-yl probe for the SPR spectroscopy selective determination of 5'-GCGGCGGC-3'

The 5'-GCGGCGGC-3' analyte binding by the (PNA H$_2$N(CO)GCGGCGGC-NH$_2$)-templated MIP film was also monitored by SPR spectroscopy under FIA conditions (Figure 3.2-10a). The analyte, dissolved in 0.1 M PBS (pH = 7.4), was passed over the SPR chip coated with the (PNA H$_2$N(CO)GCGGCGGC-NH$_2$)-extracted MIP film. This film interacted with the analyte of different concentrations in the 50 to 750 nM range. From the equilibration region (Figure 3.2-10a), the SPR signal for each analyte was measured, and then the calibration plot constructed (Figure 3.2-10b). This plot for the 5'-GCGGCGGC-3' analyte (line *1* in Figure 3.2-10b) obeyed the linear regression equation of ΔR [m°] = 15.77(±0.67) [m°] + 0.032(±0.002) [m°nM^{-1}] c_{analyte} [nM], where ΔR is the reflectance angle change. The sensitivity, correlation coefficient, and LOD determined at S/N = 3 was 0.032(±0.002) m° nM^{-1}, 0.98, and 50 nM, respectively. The MIP chemosensor was ~2.5 and ~2.7 times more selective to the matched 5'-GCGGCGGC-3' analyte than to the two- (5'-GC**T**GC**T**GC-3') and three-nucleobase (PNA H$_2$N(CO)GCG**ATC**GC-NH$_2$) PNA mismatches. From the SPR chemosensor ratio of the slopes of calibration plots for the MIP (line *1* in Figure 3.2-10b) and the corresponding NIP film (line *4* in Figure 3.2-10b), the imprinting factor was calculated. It was as high as, IF = 11, thus largely exceeding the IF value determined for the EIS chemosensor, above. Presumably, the reason for this discrepancy is that the SPR signal does not have to be strictly mass induced but can also be conformationally induced.[157] Hence, the measured signals could be accompanied by conformational changes of the resulted 2,2'-bithien-5-yl ODN analogue and the analyte upon hybridization.

From the SPR spectroscopy and ITC studies it may follow that the MIP cavity enhanced the conformational changes in the analyte molecule necessary for its hybridization with the recognizing complementary 2,2'-bithien-5-yl ODN analogue immobilized in the cavity. Apparently, the MIP exhibited enzyme-like behavior but simultaneously it was invulnerable to the surrounding conditions, such as pH, temperature, and the mass transfer of substrates or products.
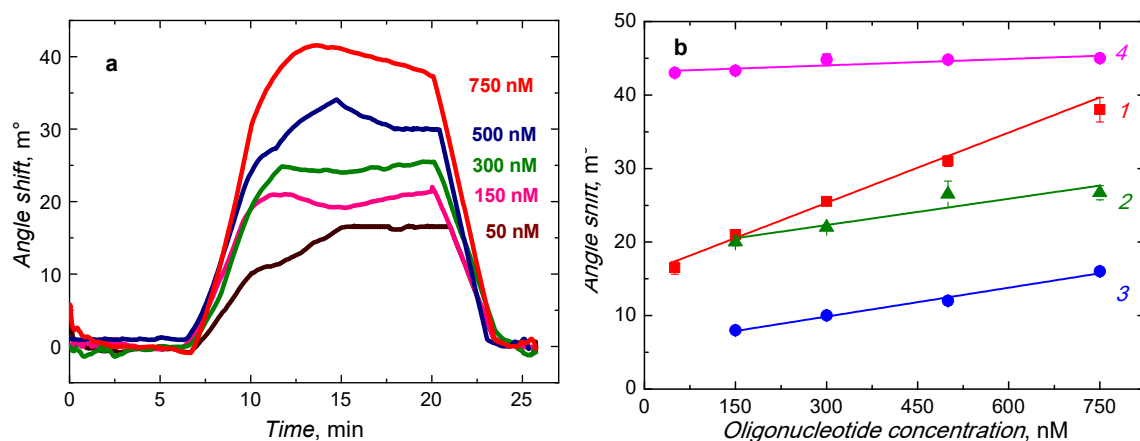
Figure 3.2-10. (a) The SPR spectroscopy signal vs. time transients, recorded under FIA conditions, for the 5'-GCGGCGGC-3' analyte of different concentrations indicated at curves. The SPR chip was coated with the (PNA H$_2$N(CO)GCGGCGGC-NH$_2$)-templated MIP film. (b) The calibration curves for the (*1*) 5'-GCGGCGGC-3', (*2*) 5'-GC**T**GC**T**GC-3', (*3*) PNA H$_2$N(CO)GCG**ATC**GC-NH$_2$ at the MIP film coated SPR chip, and (*4*) 5'-GCGGCGGC-3' at the NIP film coated SPR chip. 0.1 M PBS (pH = 7.4) served as the carrier solution. Its flow rate was 33 µL min^{-1}.
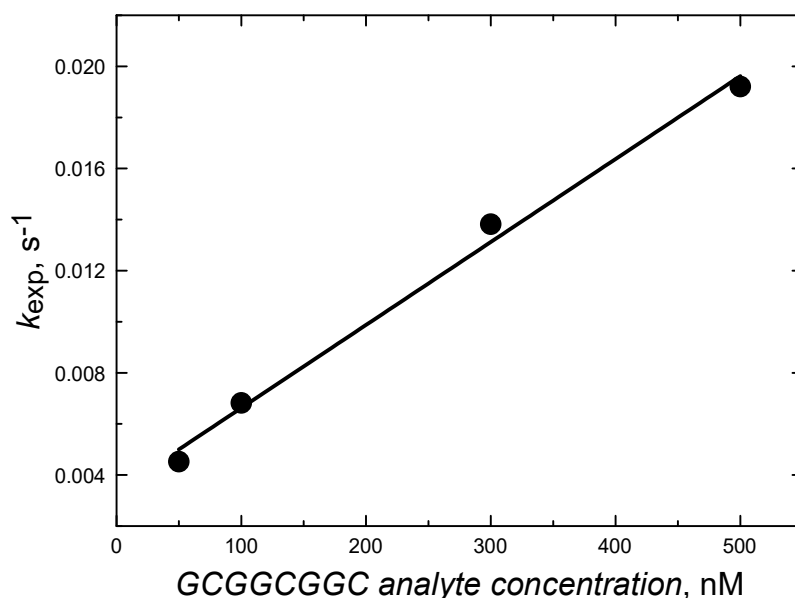
Figure 3.2-11. The dependence of the experimental rate constant, k_{exp}, on the 5'-GCGGCGGC-3' analyte concentration. The k_{exp} values were determined after non-linear fitting of kinetic parameters to association curves recorded by SPR spectroscopy.

The real-time SPR spectroscopy measurement of the analyte-analogue hybridization revealed a relatively fast kinetics ($k_a = 10^4$ M^{-1} s^{-1}, $k_d = 10^{-3}$ s^{-1}) of the

114

analyte binding and a relatively high stability constant ($K_s \approx 10^7$ M^{-1}) of the analyte-[bis(2,2'-bithien-5-yl) ODN analogue] complex (Figure 3.2-11). Moreover, this measurement provided data for calculation of hybridization efficiency (Equation 2.3-38), which was as high as ~90%. In comparison to octamers of nucleic acid analogues, the resulted MIP cavity bound complementary analyte by far faster and stronger and, most importantly, at room temperature.

3.2.6 Determination of the 5'-GCGGCGGC-3' analyte in real samples

In the polymerase chain reaction free (PCR-free) DNA or RNA detection, sample preparation usually involves three steps, i.e., extraction of the DNA from cells, isolation of the nucleic acids from the extract obtained by removing other cell components, and digestion of the extracted and isolated DNA to ONs by restriction enzymes. The second step often requires a time-consuming treatment including centrifugation, precipitation, chromatographic separation, or protein digestion. Therefore, development of an analytical procedure providing a response signal independent of the matrix components is important.

Table 3.2-3 The EIS determined matrix effect of the (PNA H$_2$N(CO)GCGGCGGC-NH$_2$)-templated MIP chemosensor for the 5'-GCGGCGGC-3' analyte in Dulbecco's Modified Eagle's Medium (DMEM).

Sample No.	$c_{5'\text{-GCGGCGGC-3'}}$ in DMEM, determined, nM	$c_{5'\text{-GCGGCGGC-3'}}$ in PBS (pH=7.4), determined, nM	Matrix effect, %
1.	2.68	2.99	89.63
2.	7.56	7.93	95.33
3.	38.82	33.81	114.81
4.	54.61	52.13	104.76
5.	71.10	69.77	101.90
Average			101.29 ± 8.56

The matrix effect was studied for the (PNA H$_2$N(CO)GCGGCGGC-NH$_2$)-templated MIP chemosensor by EIS determination of the 5'-GCGGCGGC-3' analyte in the medium with possible cell content. For that, first, the EIS measurements were

performed for the analyte of the known concentration added to the Dulbecco's Modified Eagle's Medium (DMEM). Then, this EIS signal was compared with that for the analyte of the same concentration dissolved in PBS (pH = 7.4). From the ratio of these EIS signals, the matrix effect was determined (Table 3.2-3). Advantageously, the MIP chemosensor appeared to be nearly independent of the matrix effect.

Chapter 4

Conclusions

By combining the PM, SPR spectroscopy, EIS, or CI signal transduction techniques with the MIP film recognition, we devised, fabricated, and characterized two chemical sensors for selective determination of short AT- and GC-rich oligonucleotides. Using these chemosensors, we successfully developed procedures of simple, inexpensive, rapid, and label-free chemosensing of the 5'-TATAAA-3' and 5'-GCGGCGGC-3' analytes under FIA conditions within 2 min. These determinations were possible because, inside MIPs, novel class of nucleobase-containing polymers with a very high affinity for complementary nucleic acid targets at room temperature served as probes. Similarly to syntheses of other nucleobase-containing polymers, the concept of polymerizing monomers aligned along a template to result in a preformed artificial oligomer using hydrogen bonding interactions was herein utilized for controlling the sequence of nucleobase units along a polymer chain. Stability of the complexes of functional monomers with selected templates was quantum-chemistry calculated and ITC determined. Molecular imprinting with electrochemical polymerization provided means of a simple, fast, and catalyst-free synthesis of stable bis(2,2'-bithien-5-yl) oligomers designed to reveal properties of DNA analogues.

One TTTATA probe, constrained in MIP cavities, vacated after template extraction, strongly hybridized the 5'-TATAAA-3' analyte with the complex stability constant, $K_s^{\text{TTTATA-TATAAA}} = k_a/k_d \approx 10^6 \text{ M}^{-1}$, i.e., as high as that characteristic for longer-chain DNA-PNA hybrids. Moreover, this probe was invulnerable to non-specific interaction and capable of discrimination of single purine-nucleobase mismatch, thus making it uniquely suited for hybridization-based SNP genotyping. Under carefully chosen FIA conditions, i.e., at a relatively low flow rate of the carrier solution and a large volume of the injected sample solution, the concentration limit of detection, determined by capacitive impedimetry, was as low as ~5 nM 5'-TATAAA-3', quite appreciable as for the hexadeoxyribonucleotide. Molecular imprinting increased the chemosensor sensitivity to the 5'-TATAAA-3' analyte over four times compared to that of the non-imprinted polymer.

The other sequence-defined bis(2,2'-bithien-5-yl) DNA probe was prepared according to the procedure same as that described above That is, it involved molecular imprinting with a sequence-programmable template. The combination of

electrochemical or SPR spectroscopy transduction technique with the synthesis of a new DNA analogue allowed fabricating an MIP chemosensor for determination of genetically relevant 5'-GCGGCGGC-3' oligonucleotide. In accordance with literature,[9] ITC measurements confirmed that the stability constant of the G-C pairs of the functional monomers with PNA template was by two orders of magnitude higher than that of the A-T pairs. Despite the strong interaction between recognizing sites and the analyte, the chemosensor was selective to two- and three-nucleobase mismatches and discriminative to Dulbecco's Modified Eagle's Medium sample interferences. With highly sensitive and simple to operate EIS and SPR transductions under stagnant-solution and FIA conditions, respectively, the analyte was determined using EIS with the 200 pM limit of detection. Molecular imprinting increased the chemosensor sensitivity to the 5'-GCGGCGGC-3' analyte over four times compared to that of the non-imprinted polymer. The real-time SPR spectroscopy measurement of analyte-analogue hybridization revealed a relatively fast kinetics ($k_a = 10^4$ $M^{-1}s^{-1}$, $k_d = 10^{-3}$ s^{-1}) of the analyte binding to the MIP cavity and releasing from this cavity, respectively, as well as a high stability constant ($K_s \approx 10^7$ M^{-1}) of the (analyte)-(2,2'-bithien-5-yl) DNA analogue complex. Moreover, the SPR measurement provided data for calculation of hybridization efficiency, which was as high as ~90%. In comparison to octamers of other nucleic acid analogues, the MIP cavity bound the complementary DNA analyte much faster and stronger and, importantly, at room temperature.

The developed strategy of MIP preparation enables utilization of the self-recognizing properties and sequence programmability of DNA to generate tailored artificial oligomers.

References

1. Nielsen, P. E.; Egholm, M.; Berg, R. H.; Buchardt, O., Sequence-Selective Recognition of DNA by Strand Displacement with a Thymine-Substituted Polyamide. *Science* **1991,** *254*, 1497-1500.

2. Pinheiro, V. B.; Holliger, P., Towards XNA Nanotechnology: New Materials from Synthetic Genetic Polymers. *Trends Biotechnol.* **2014,** *32*, 321-328.

3. Karkare, S.; Bhatnagar, D., Promising Nucleic Acid Analogs and Mimics: Characteristic Features And Applications Of PNA, LNA, and Morpholino. *Appl. Microbiol. Biotechnol.* **2006,** *71*, 575-586.

4. Egholm, M.; Buchardt, O.; Christensen, L.; Behrens, C.; Freier, S. M.; Driver, D. A.; Berg, R. H.; Kim, S. K.; Norden, B.; Nielsen, P. E., PNA Hybridizes to Complementary Oligonucleotides Obeying the Watson-Crick Hydrogen-Bonding Rules. *Nature* **1993,** *365*, 566-568.

5. Demidov, V. V.; Potaman, V. N.; Frankkamenetskii, M. D.; Egholm, M.; Buchard, O.; Sonnichsen, S. H.; Nielsen, P. E., Stability of Peptide Nucleic-Acids in Human Serum and Cellular-Extracts. *Biochem. Pharmacol.* **1994,** *48*, 1310-1313.

6. Hudziak, R. M.; Barofsky, E.; Barofsky, D. F.; Weller, D. L.; Huang, S. B.; Weller, D. D., Resistance of Morpholino Phosphorodiamidate Oligomers to Enzymatic Degradation. *Antisense Nucleic Acid Drug Dev.* **1996,** *6*, 267-272.

7. Taylor, M. F.; Paulauskis, J. D.; Weller, D. D.; Kobzik, L., In Vitro Efficacy of Morpholino-Modified Antisense Oligomers Directed Against Tumor Necrosis Factor-Alpha mRNA. *J. Biol. Chem.* **1996,** *271*, 17445-17452.

8. Hyrup, B.; Nielsen, P. E., Peptide Nucleic Acids (PNA): Synthesis, Properties and Potential Applications *Bioorg. Med. Chem.* **1996,** *4*, 5-23.

9. Bartold, K.; Pietrzyk-Le, A.; Golebiewska, K.; Lisowski, W.; Cauteruccio, S.; Licandro, E.; D'Souza, F.; Wlodzimierz Kutner, W., Macromolecular Imprinting of Peptide Nucleic Acid Resulting in an Electropolymerized Sequence-Controlled CG-rich Artificial Oligomer Analog for Improved Oligonucleotide Determination. *ACS Appl. Mater. Interfaces* **2018,** *10*, 27562-27569.

10. Bartold, K.; Pietrzyk-Le, A.; Huynh, T.-P.; Iskierko, Z.; Sosnowska, M.; Noworyta, K.; Lisowski, W.; Sannicolo, F.; Cauteruccio, S.; Licandro, E.; D'Souza, F.; Kutner, W., Programmed Transfer of Sequence Information into a Molecularly Imprinted Polymer for Hexakis(2,2'-bithien-5-yl) DNA Analogue Formation toward Single-Nucleotide-Polymorphism Detection. *ACS Appl. Mater. Interfaces* **2017,** *9*, 3948-3958.

11. Cutrona, G.; Carpaneto, E. M.; Ulivi, M.; Roncella, S.; Landt, O.; Ferrarini, M.; Boffa, L. C., Effects in Live Cells af a C-Myc Anti-Gene PNA Linked to a Nuclear Localization Signal. *Nat. Biotechnol.* **2000,** *18*, 300-303.

12. Hamilton, S. E.; Simmons, C. G.; Kathiriya, I. S.; Corey, D. R., Cellular Delivery of Peptide Nucleic Acids and Inhibition of Human Telomerase. *Chem. Biol.* **1999,** *6*, 343-351.

13. Gupta, A.; Quijano, E.; Liu, Y.; Bahal, R.; Scanlon, S. E.; Song, E.; Hsieh, W.-C.; Braddock, D. E.; Ly, D. H.; Saltzman, W. M.; Glazer, P. M., Anti-tumor Activity

of miniPEG-γ-Modified PNAs to Inhibit MicroRNA-210 for Cancer Therapy. *Mol. Ther. Nucleic Acids* **2017,** *9*, 111-119.

14. Singh, S. K.; Nielsen, P.; Koshkin, A. A.; Wengel, J., LNA (Locked Nucleic Acids): Synthesis and High-Affinity Nucleic Acid Recognition. *Chem. Commun.* **1998**, 455-456.

15. McTigue, P. M.; Peterson, R. J.; Kahn, J. D., Sequence-Dependent Thermodynamic Parameters for Locked Nucleic Acid (LNA)−DNA Duplex Formation. *Biochemistry* **2004,** *43*, 5388-5405.

16. Bertucci, A.; Manicardi, A.; Corradini, R., Advanced Molecular Probes for Sequence-Specific DNA Recognition. In *Detection of non-amplified genomic DNA*, Spoto, G.; Corradini, R., Eds. Springer Netherlands: Dordrecht, 2012; pp 89-124.

17. Jepsen, J. S.; Sorensen, M. D.; Wengel, J., Locked Nucleic Acid: A Potent Nucleic Acid Analog in Therapeutics And Biotechnology. *Oligonucleotides* **2004,** *14*, 130-146.

18. Petersen, M.; Wengel, J., LNA: A Versatile Tool for Therapeutics and Genomics. *Trends Biotechnol.* **2003,** *21*, 74-81.

19. Stirchak, E. P.; Summerton, J. E.; Weller, D. D., Uncharged Stereoregular Nucleic-Acid Analogs: 2. Morpholino Nucleoside Oligomers with Carbamate Internucleoside Linkages. *Nucleic Acids Res.* **1989,** *17*, 6129-6141.

20. Kang, H.; Chou, P. J.; Johnson, W. C.; Weller, D.; Huang, S. B.; Summerton, J. E., Stacking Interactions of APA Analogs with Modified Backbones. *Biopolymers* **1992,** *32*, 1351-1363.

21. Summerton, J., Morpholino Antisense Oligomers: The Case for an RNase-H Independent Structural Type. *Biochim. Biophys. Acta* **1999,** *1489*, 141-158.

22. Janson, C. G.; During, M., *Peptide Nucleic Acids, Morpholinos and Related Antisense Biomolecules*. Springer: 2006.

23. Ekker, S. C.; Larson, J. D., Morphant Technology in Model Developmental Systems. *Genesis* **2001,** *30*, 89-93.

24. Jones, A. S.; Parsons, D. G., Fractionation of Ribonucleic Acids by Means of a New Type of Exchanger. *Proc. Chem. Soc.* **1961,** *78*, 33-92.

25. Jones, A. S.; Parsons, D. G.; Roberts, D. G., The Interaction of Polynucleotides with a Guanine Derivative of Cellulose. *Eur. Polym. J.* **1967,** *3*, 187-198.

26. Kondo, K.; Iwasaki, H.; Nakatani, K.; Ueda, N.; Takemoto, K.; Imoto, M., Vinyl Compounds of Nucleic Acid Bases. Polymerization and Copolymerization Of *N*-Vinyl And *B*-Methacryloyloxyethyl Compounds of Nucleic Acid Bases and Their Polymer-Polymer Interactions. *Makromol. Chem.* **1969,** *125*, 42-47.

27. Pitha, J.; Tso, P. O. P., *N*-Vinyl Derivatives of Substituted Pyrimidines and Purines. *J. Org. Chem.* **1968,** *33*, 1341-1344.

28. Khan, A.; Haddleton, D. M.; Hannon, M. J.; Kukulj, D.; Marsh, A., Hydrogen Bond Template-Directed Polymerization of Protected 5'-Acryloylnucleosides. *Macromolecules* **1999,** *32*, 6560-6564.

120

29. Spijker, H. J.; Dirks, A. J.; Van Hest, J. C. M., Synthesis and Assembly Behavior of Nucleobase-Functionalized Block Copolymers. *J. Polym. Sci. Part A: Polym. Chem.* **2006,** *44*, 4242-4250.

30. Kang, Y.; Lu, A.; Ellington, A.; Jewett, M. C.; O'Reilly, R. K., Effect of Complementary Nucleobase Interactions on the Copolymer Composition of RAFT Copolymerizations. *ACS Macro Let.* **2013,** *2*, 581-586.

31. Cheng, C. C.; Huang, C. F.; Yen, Y. C.; Chang, F. C., A "Plug And Play" Polymer Through Biocomplementary Hydrogen Bonding. *J. Polym. Sci. Part A: Polym. Chem.* **2008,** *46*, 6416-6424.

32. McHale, R.; O'Reilly, R. K., Nucleobase Containing Synthetic Polymers: Advancing Biomimicry via Controlled Synthesis and Self-Assembly. *Macromolecules* **2012,** *45*, 7665-7675.

33. Yang, H. T.; Xi, W. X., Nucleobase-Containing Polymers: Structure, Synthesis, and Applications, Polymers. *Polymers* **2017,** *9*, 666-690.

34. Kang, Y.; Pitto-Barry, A.; Willcock, H.; Quan, W.-D.; Kirby, N.; Sanchez, A. M.; O'Reilly, R. K., Exploiting Nucleobase-containing Materials - From Monomers to Complex Morphologies using RAFT Dispersion Polymerization. *Polym. Chem.* **2015,** *6*, 106-117.

35. Nakahata, M.; Takashima, Y.; Hashidzume, A.; Harada, A., Macroscopic Self-Assembly Based on Complementary Interactions Between Nucleobase Pairs. *Chem. Eur. J.* **2015,** *21*, 2770-2774.

36. Lee, D. S.; Qian, H.; Tay, C. Y.; Leong, D. T., Cellular Processing and Destinies of Artificial DNA Nanostructures. *Chem. Soc. Rev.* **2016,** *45*, 4199-4225.

37. Xi, W. X.; Pattanayak, S.; Wang, C.; Fairbanks, B.; Gong, T.; Wagner, J.; Kloxin, C. J.; Bowman, C. N., Clickable Nucleic Acids: Sequence-Controlled Periodic Copolymer/Oligomer Synthesis by Orthogonal Thiol-X Reactions. *Angew. Chem., Int. Ed.* **2015,** *54*, 14462-14467.

38. Grubbs, R. H.; Tumas, W., Polymer Synthesis and Organotransition Metal Chemistry. *Science* **1989,** *243*, 907-915.

39. Mutch, A.; Leconte, M.; Lefebvre, F.; Basset, J. M., Effect of Alcohols and Epoxides on the Rate of ROMP of Norbornene by a Ruthenium Trichloride Catalyst. *J. Mol. Catal. A* **1998,** *133*, 191-199.

40. Lo, P. K.; Sleiman, H. F., Nucleobase-Templated Polymerization: Copying the Chain Length and Polydispersity of Living Polymers into Conjugated Polymers. *J. Am. Chem. Soc.* **2009,** *131*, 4182-4183.

41. James, C. R.; Rush, A. M.; Insley, T.; Vukovic, L.; Adamiak, L.; Kral, P.; Gianneschi, N. C., Poly(oligonucleotide). *J. Am. Chem. Soc.* **2014,** *136*, 11216-11219.

42. Caliari, S. R.; Burdick, J. A., A Practical Guide to Hydrogels for Cell Culture. *Nat. Methods* **2016,** *13*, 405-414.

43. Tan, H. P.; Xiao, C.; Sun, J. C.; Xiong, D. S.; Hu, X. H., Biological Self-Assembly of Injectable Hydrogel as Cell Scaffold via Specific Nucleobase Pairing. *Chem. Commun.* **2012,** *48*, 10289-10291.

44. Oupicky, D.; Konak, C.; Ulbrich, K.; Wolfert, M. A.; Seymour, L. W., DNA Delivery Systems Based on Complexes of DNA with Synthetic Polycations and their Copolymers. *J. Control. Release* **2000,** *65*, 149-171.

45. Harguindey, A.; Domaille, D. W.; Fairbanks, B. D.; Wagner, J.; Bowman, C. N.; Cha, J. N., Synthesis and Assembly of Click-Nucleic-Acid-Containing PEG-PLGA Nanoparticles for DNA Delivery. *Adv. Mater.* **2017,** *29*, 6.

46. Cheng, C. C.; Chang, F. C.; Dai, S. A.; Lin, Y. L.; Lee, D. J., Bio-Complementary Supramolecular Polymers with Effective Self-Healing Functionality. *RSC Adv.* **2015,** *5*, 90466-90472.

47. Ye, X.; Li, X.; Shen, Y. Q.; Chang, G. J.; Yang, J. X.; Gu, Z. W., Self-Healing pH-Sensitive Cytosine- and Guanosine-Modified Hyaluronic Acid Hydrogels via Hydrogen Bonding. *Polymer* **2017,** *108*, 348-360.

48. Yang, C. H.; Bolotin, E.; Jiang, T.; Sladek, F. M.; Martinez, E., Prevalence of the Initiator Over the TATA Box in Human and Yeast Genes and Identification of DNA Motifs Enriched in Human TATA-Less Core Promoters. *Gene* **2007,** *389*, 52-65.

49. Lodish, H.; Berk, A.; Zipursky, S. L.; Matsudaira, P.; Baltimore, D.; Darnell, J., *Mollecular Cell Biology*. 7th ed.; Freeman: New York, 2012.

50. Grunberg, S.; Hahn, S., Structural Insights into Transcription Initiation by RNA Polymerase II. *Trends Biochem. Sci.* **2013,** *38*, 603-611.

51. Nikolov, D. B.; Hu, S.-H.; Lin, J.; Gasch, A.; Hoffmann, A.; Horikoshi, M.; Chua, N.-H.; Roeder, R. G.; Burley, S. K., Crystal Structure of TFIID TATA-Box Binding Protein. *Nature* **1992,** *360*, 40-46.

52. Kim, J. L.; Nikolov, D. B.; Burley, S. K., Co-Crystal Structure of TBP Recognizing the Minor Groove of a TATA Element. *Nature* **1993,** *365*, 520-527.

53. Kim, Y.; Geiger, J. H.; Hahn, S.; Sigler, P. B., Crystal Structure of a Yeast TBP/TATA-Box Complex. *Nature* **1993,** *365*, 512-520.

54. Boon, E. M.; Salas, J. E.; Barton, J. K., An Electrical Probe of Protein-DNA Interactions on DNA-Modified Surfaces. *Nat. Biotech.* **2002,** *20*, 282-286.

55. Gorodetsky, A. A.; Ebrahim, A.; Barton, J. K., Electrical Detection of TATA Binding Protein at DNA-Modified Microelectrodes. *J. Am. Chem. Soc.* **2008,** *130*, 2924-2925.

56. Ziff, E. B.; Evans, R. M., Coincidence of the Promoter and Capped 5' Terminus of RNA from the Adenovirus 2 Major Late Transcription Unit. *Cell* **1978,** *15*, 1463-1475.

57. Doluca, O.; Withers, J. M.; Filichev, V. V., Molecular Engineering of Guanine-Rich Sequences: Z-DNA, DNA Triplexes, and G-Quadruplexes. *Chem. Rev.* **2013,** *113*, 3044-3083.

58. Mamedov, T. G.; Pienaar, E.; Whitney, S. E.; TerMaat, J. R.; Carvill, G.; Goliath, R.; Subramanian, A.; Viljoen, H. J., A Fundamental Study of the PCR Amplification of GC-Rich DNA Templates. *Comp. Biol. Chem.* **2008,** *32*, 452-457.

59. Xiao, X.; Wu, T.; Xu, L.; Chen, W.; Zhao, M., A Branch-Migration Based Fluorescent Probe for Straightforward, Sensitive and Specific Discrimination of DNA Mutations. *Nucleic Acids Res.* **2017,** *45*, e90-e90.

60. Liu, H.; Wang, Y.; Zhang, L.; Shao, Y.; Zheng, B., Fluorescent Silver Nanoclusters as Probes for Selective Recognition of DNA CGG Trinucleotide Repeat. *Mater. Lett.* **2015,** *139*, 265-267.

61. He, H.; Xia, J.; Peng, X.; Chang, G.; Zhang, X.; Wang, Y.; Nakatani, K.; Lou, Z.; Wang, S., Facile Electrochemical Biosensor Based on a New Bifunctional Probe for Label-Free Detection of CGG Trinucleotide Repeat. *Biosens. Bioelectron.* **2013,** *49*, 282-289.

62. He, H.; Peng, X.; Huang, M.; Chang, G.; Zhang, X.; Wang, S., An Electrochemical Impedance Sensor Based on a Small Molecule Modified Au Electrode for the Recognition of a Trinucleotide Repeat. *Analyst* **2014,** *139*, 5482-5487.

63. Makova, D.; Hardison, R. C., The Effects of Chromatin Organization on Variation in Mutation Rates in the Genome. *Nat. Rev. Genet.* **2015,** *16*, 213.

64. Bichenkova, E. V.; Lang, Z.; Yu, X.; Rogert, C.; Douglas, K. T., DNA-Mounted Self-Assembly: New Approaches for Genomic Analysis and SNP Detection. *Biochim. Biophys. Acta, Gene Regul. Mech.* **2011,** *1809*, 1-23.

65. Turner, A. P. F., Biosensors: Sense and Sensibility. *Chem. Soc. Rev.* **2013,** *42*, 3184-3196.

66. Janku, F.; Vibat, C. R. T.; Kosco, K.; Holley, V. R.; Cabrilo, G.; Meric-Bernstam, F.; Stepanek, V. M.; Lin, P. P.; Leppin, L.; Hassaine, L.; Poole, J. C.; Kurzrock, R.; Erlander, M. G., *BRAF* V600E Mutations in Urine and Plasma Cell-Free DNA from Patients With Erdheim-Chester Disease. *Oncotarget* **2014,** *5*, 3607-3610.

67. Menger, M.; Yarman, A.; Erdőssy, J.; Yildiz, H. B.; Gyurcsányi, R. E.; Scheller, F. W., MIPs and Aptamers for Recognition of Proteins in Biomimetic Sensing. *Biosensors* **2016,** *6*, 35.

68. Mills, D. M.; Martin, C. P.; Armas, S. M.; Calvo-Marzal, P.; D.M. Kolpashchikov; Chumbimuni-Torres, K. Y., A Universal and Label-Free Impedimetric Biosensing Platform for Discrimination of Single Nucleotide Substitutions in Long Nucleic Acid Strands. *Biosen. Bioelectron.* **2018,** *109*, 35-42.

69. Bonnet, G.; Tyagi, S.; Libchaber, A.; Kramer, F. R., Thermodynamic Basis of the Enhanced Specificity of Structured DNA Probes. *Proc. Natl. Acad. Sci. U. S. A.* **1999,** *96*, 6171-6176.

70. Nguyen, A. H.; Sim, S. J., Nanoplasmonic Biosensor: Detection and Amplification of Dual Bio-Signatures of Circulating Tumor DNA. *Biosen. Bioelectron.* **2015,** *67*, 443-449.

71. Lei, Y.; Wang, K.; Wu, S.-Y.; Huang, D.-D.; Dai, M.; Zheng, Y.-J.; Sun, Z.-L.; Chen, Y.-Z.; Lin, X.-H.; Liu, A.-L., 2′-Fluoro Ribonucleic Acid Modified DNA Dual-Probe Sensing Strategy for Enzyme-Amplified Electrochemical Detection of Double-Strand DNA of PML/RARα Related Fusion Gene. *Biosen. Bioelectron.* **2018,** *112*, 170-176.

72. Jampasa, S.; Wonsawat, W.; Rodthongkum, N.; Siangproh, W.; Yanatatsaneejit, P.; T.Vilaivan; Chailapakul, O., Electrochemical Detection of Human Papillomavirus DNA Type 16 Using a Pyrrolidinyl Peptide Nucleic Acid Probe Immobilized on Screen-Printed Carbon Electrodes. *Biosen. Bioelectron.* **2014,** *54*, 428-434.

73. Cai, B.; Wang, S.; Huang, L.; Ning, Y.; Zhang, Z.; Zhang, G.-J., Ultrasensitive Label-Free Detection of PNA–DNA Hybridization by Reduced Graphene Oxide Field-Effect Transistor Biosensor. *ACS Nano* **2014,** *8*, 2632-2638.

74. Kryscio, D. R.; Peppas, N. A., Critical Review and Perspective of Macromolecularly Imprinted Polymers. *Acta Biomater.* **2012,** *8*, 461-473.

75. Haupt, K., Molecular Imprinting In *Molecular Imprinting*, Haupt, K., Ed. Springer-Verlag Berlin: Berlin, 2012; Vol. 325, pp IX-XII.

76. Cieplak, M.; Kutner, W., Artificial Biosensors: How Can Molecular Imprinting Mimic Biorecognition? *Trends Biotechnol.* **2016,** *34*, 922-941.

77. Hvastkovs, E. G.; Buttry, D. A., Recent Advances in Electrochemical DNA Hybridization Sensors. *Analyst* **2010,** *135*, 1817-1829.

78. Li, S. J.; Cao, S. S.; Whitcombe, M. J.; Piletsky, S. A., Size Matters: Challenges in Imprinting Macromolecules. *Prog. Polym. Sci.* **2014,** *39*, 145-163.

79. Zhang, Z.; Liu, J., Molecularly Imprinted Polymers with DNA Aptamer Fragments as Macromonomers. *ACS Appl. Mater. Interfaces* **2016,** *8*, 6371–6378.

80. Huynh, T.-P.; Pieta, P.; D'Souza, F.; Kutner, W., Molecularly Imprinted Polymer for Recognition of 5-Fluorouracil by RNA-Type Nucleobase Pairing. *Anal. Chem.* **2013,** *85*, 8304-8312.

81. Shea, K. J.; Spivak, D. A.; Sellergen, B., Polymer complements to nucleotide bases - selective binding of adenine derivatives to imprinted polymers *J. Am. Chem. Soc.* **1993,** *115*, 3368-3369.

82. Spivak, D.; Gilmore, M. A.; Shea, K. J., Evaluation of binding and origins of specificity of 9-ethyladenine imprinted polymers. *J. Am. Chem. Soc.* **1997,** *119*, 4388-4393.

83. Tiwari, A.; Deshpande, S.; Kobayashi, H.; Turner, A. P. F., Detection of P53 Gene Point Mutation Using Sequence-Specific Molecularly Imprinted PoPD Electrode. *Biosens. Bioelectron.* **2012,** *35*, 224-229.

84. Slinchenko, O.; Rachkov, A.; Miyachi, H.; Ogiso, M.; Minoura, N., Imprinted Polymer Layer for Recognizing Double-Stranded DNA. *Biosen. Bioelectron.* **2004,** *20*, 1091-1097.

85. Watson, J. D.; Crick, F. H. C., Genetical Implications of the Structure of Deoxyribonucleic Acid. *Nature* **1953,** *171*, 964-967.

86. Ratautaite, V.; Topkaya, S. N.; Mikoliunaite, L.; Ozsos, M.; Oztekin, Y., Molecularly Imprinted Polypyrrole for DNA Determination. *Electroanalysis* **2013,** *25*, 1169-1177.

87. Pietrzyk-Le, A.; D'Souza, F.; Kutner, W., Applications of Supramolecular Self-Assembly Governed Molecularly Imprinted Polymers for Selective Chemical Sensing. In *Supramolecular Chemistry for 21st Century Technology*, Schneider,

H.-J., Ed. Taylor & Francis/CRC Press: Boca Raton London New York, UK, 2012, pp. 105-128.

88. Spivak, D. A.; Shea, K. J., Investigation into the Scope and Limitations of Molecular Imprinting with DNA Molecules. *Anal. Chim. Acta* **2001,** *435*, 65-74.

89. Huynh, T.-P.; Sharma, P. S.; Sosnowska, M.; D'Souza, F.; Kutner, W., Functionalized Polythiophenes: Recognition Materials for Chemosensors and Biosensors of Superior Sensitivity, Selectivity, and Detectability. *Prog. Polym. Sci.* **2015,** *47*, 1-25.

90. Jolly, P.; Tamboli, V.; Harniman, R. L.; Estrela, P.; Allender, C. J.; Bowen, J. L., Aptamer–MIP Hybrid Receptor for Highly Sensitive Electrochemical Detection of Prostate Specific Antigen. *Biosen. Bioelectron.* **2016,** *75*, 188-195.

91. Dechtrirat, D.; N., G.-E.; F.F., B.; Scheller, F. W., Hybrid Material for Protein Sensing Based on Electrosynthesized MIP on a Mannose Terminated Self-Assembled Monolayer. *Adv. Funct. Mater.* **2014,** *24*, 2233–2239.

92. Bai, W.; Gariano, N. A.; Spivak, D. A., Macromolecular Amplification of Binding Response in Superaptamer Hydrogels. *J. Am. Chem. Soc.* **2014,** *135*, 6977−6984.

93. Poma, A.; Brahmbhatt, H.; Hannah, M. P.; Jonathan, K. W.; Nicholas, W. T., Generation of Novel Hybrid Aptamer–Molecularly Imprinted Polymeric Nanoparticles. *Adv. Mater.* **2014,** *27*, 750-758.

94. Culver, H. R.; Clegg, J. R.; Peppas, N. A., Analyte-Responsive Hydrogels: Intelligent Materials for Biosensing and Drug Delivery. *Acc. Chem. Res.* **2017,** *50*, 170-178.

95. Nielsen, P. E., In *Peptide Nucleic Acids: Protocols and Applications* Nielsen, P. E., Ed. Horizon Bioscience: Wymondham, UK, 2004; p 37.

96. Watson, J. D.; Crick, F. H. C., Molecular structure of nucleic acids: A structure for deoxyribose nucleic acid. *Nature* **1953,** *171*, 737-738.

97. Board, R. E.; Thelwell, N. J.; Ravetto, P. F.; Little, S.; Ranson, M.; Dive, C.; Hughes, A.; Whitcombe, D., Multiplexed Assays for Detection of Mutations in PIK3CA. *Clin. Chem.* **2008,** *54*, 757-760.

98. Frisch, M. J.; Trucks, G. W.; Schlegel, H. B.; Scuseria, G. E.; Robb, M. A.; Cheeseman, J. R.; Scalmani, G.; Barone, V.; Mennucci, B.; Petersson, G. A.; Nakatsuji, H.; Caricato, M.; Li, X.; Hratchian, H. P.; Izmaylov, A. F.; Bloino, J.; Zheng, G.; Sonnenberg, J. L.; Hada, M.; Ehara, M.; Toyota, K.; Fukuda, R.; Hasegawa, J.; Ishida, M.; Nakajima, T.; Honda, Y.; Kitao, O.; Nakai, H.; Vreven, T.; Montgomery Jr., J. A.; Peralta, J. E.; Ogliaro, F.; Bearpark, M. J.; Heyd, J.; Brothers, E. N.; Kudin, K. N.; Staroverov, V. N.; Kobayashi, R.; Normand, J.; Raghavachari, K.; Rendell, A. P.; Burant, J. C.; Iyengar, S. S.; Tomasi, J.; Cossi, M.; Rega, N.; Millam, N. J.; Klene, M.; Knox, J. E.; Cross, J. B.; Bakken, V.; Adamo, C.; Jaramillo, J.; Gomperts, R.; Stratmann, R. E.; Yazyev, O.; Austin, A. J.; Cammi, R.; Pomelli, C.; Ochterski, J. W.; Martin, R. L.; Morokuma, K.; Zakrzewski, V. G.; Voth, G. A.; Salvador, P.; Dannenberg, J. J.; Dapprich, S.; Daniels, A. D.; Farkas, Ö.; Foresman, J. B.; Ortiz, J. V.; Cioslowski, J.; Fox, D. J. *Gaussian 09, Revision B.01,*, Gaussian, Inc., Wallingford CT: 2010.

99. Koh, W.; Kutner, W.; Jones, M. T.; Kadish, K. M., An Improved Holder for the Electrochemical Quartz Crystal Microbalance and Its Cyclic Voltammetry Characteristics. *Electroanalysis* **1993,** *5*, 209-214.

100. Soucaze-Guillous, B.; Kutner, W., Flow Characteristics of Versatile Wall-jet or Radial Flow Thin-layer Large-volume Cell for Electrochemical Detection in Flow-through Analytical Techniques *Electroanalysis* **1997,** *9*, 32-38.

101. Kochman, A.; Krupka, A.; Grissbach, J.; W. Kutner; Gniewinska, B.; Nafalski, L., Design and performance of a new thin-layer radial-flow holder for a quartz crystal resonator of an electrochemical quartz crystal microbalance. *Electroanalysis* **2006,** *18*, 2168-2173.

102. Leavitt, S.; Freire, E., Direct Measurement of Protein Binding Energetics by Isothermal Titration Calorimetry. *Curr. Opin. Struct. Biol.* **2001,** *11*, 560-566.

103. Song, C.; Zhang, S.; Huang, H., Choosing a Suitable Method for the Identification of Replication Origins in Microbial Genomes. *Front. Microbiol.* **2015,** *6*, 1049.

104. Chiu, M. H.; Berezowski, N. S.; Prenner, E. J., DSC Applications: Macromolecules In *Drug–Biomembrane Interaction Studies*, Woodhead Publishing: 2013; pp 237-263.

105. Chakrabarti, M. C.; Schwarz, F. P., Thermal Stability of PNA/DNA and DNA/DNA Duplexes by Differential Scanning Calorimetry. *Nucleic Acids Res.* **1999,** *27*, 4801-4806.

106. Galus, Z., *Fundamentals of Electrochemical Analysis*. Polish Scientific Publishers PWN: Warsaw, 1994.

107. Monk, P., *Fundamentals of Electroanalytical Chemistry*. John Wiley and Sons: England, 2001.

108. Iskierko, Z.; Sharma, P. S.; Bartold, K.; Pietrzyk-Le, A.; Noworyta, K.; Kutner, W., Molecularly Imprinted Polymers For Separating and Sensing of Macromolecular Compounds and Microorganisms. *Biotechnol. Adv.* **2016,** *34*, 30-46.

109. Orazem, M. E.; Tribollet, B., *Electrochemical Impedance Spectroscopy*. John Wiley and Sons: New Jersey, 2008.

110. Gamry https://www.gamry.com/assets/Uploads/Basics-of-Electrochemical-Impedance-Spectroscopy.pdf.

111. Ruhi, G.; Dhawan, S. K., Conducting Polymer Nano Composite Epoxy Coatings for Anticorrosive Applications. In *Modern Electrochemical Methods in Nano, Surface and Corrosion Science*, InTech: Rijeka, 2014.

112. Lasia, A., *Electrochemical Impedance Spectroscopy and its Applications*. Modern Aspects of Electrochemistry ed.; Springer-Verlag: New York, 2009; Vol. 43.

113. Buck, R. P.; Lindner, E.; Kutner, W.; Inzelt, G., Piezoelectric Chemical Sensors - (IUPAC Technical Report). *Pure Appl. Chem.* **2004,** *76*, 1139-1160.

114. Skládal, P., Piezoelectric Quartz Crystal Sensors Applied for Bioanalytical Assays and Characterization of Affinity Interactions. *J. Braz. Chem. Soc.* **2003,** *14*, 491-502.

115. Ordal, M. A.; Long, L. L.; Bell, R. J.; Bell, S. E.; Bell, R. R.; Alexander, R. W.; Ward, C. A., Optical Properties of the Metals Al, Co, Cu, Au, Fe, Pb, Ni, Pd, Pt, Ag, Ti, and W in the Infrared and Far Infrared. *Appl. Optics* **1983,** *22*, 1099-1119.

116. Davies, J., *Surface Analytical Techniques for Probing Biomaterial Processes*. CRC Press: Boca Raton, 1996.

117. Šípová, H.; Homola, J., Surface Plasmon Resonance Sensing of Nucleic Acids: A Review. *Anal. Chim. Acta* **2013,** *773*, 9-23.

118. Marquart, A. https://www.sprpages.nl.

119. Binnig, G.; Quate, C. F.; Gerber, C., Atomic Force Microscope. *Phys. Rev. Lett.* **1986,** *56*, 930-933.

120. Barret, C. J. www.barret-group.mcgill.ca.

121. Furche, F.; Ahlrichs, R.; Hattig, C.; Klopper, W.; Sierka, M.; Weigend, F., Turbomole. *WIREs Comput. Mol. Sci.* **2014,** *4*, 91-100.

122. Cybulski, S. M.; Bledson, T. M.; Toczydlowski, R. R., Comment on Hydrogen Bonding and Stacking Interactions of Nucleic Acid Base Pairs: A Density-Functional-Theory Treatment. *J. Chem. Phys.* **2002,** *116*, 11039-11040.

123. Elstner, M.; Hobza, P.; Frauenheim, T.; Suhai, S.; Kaxiras, E., Hydrogen Bonding and Stacking Interactions of Nucleic Acid Base Pairs: A Density-Functional-Theory Based Treatment. *J. Chem. Phys.* **2001,** *114*, 5149-5155.

124. Hobza, P.; Šponer, J., Toward True DNA Base-Stacking Energies: MP2, CCSD(T), and Complete Basis Set Calculations. *J. Am. Chem. Soc.* **2002,** *124*, 11802–11808.

125. Graziano, G.; Klimeš, J.; Fernandez-Alonso, F.; Michaelides, A., Improved Description of Soft Layered Materials with Van der Waals Density Functional Theory. *J. Phys. Condens. Matter.* **2012,** *24*, 424216-424223.

126. Sen, A.; Nielsen, P. E., On The Stability of Peptide Nucleic Acid Duplexes in the Presence of Organic Solvents. *Nucleic Acids Res.* **2007,** *35*, 3367-3374.

127. Dragulescu-Andrasi, A.; Rapireddy, S.; Frezza, B. M.; Gayathri, C.; Gil, R. R.; Ly, D. H., A Simple *γ*-Backbone Modification Preorganizes Peptide Nucleic Acid into a Helical Structure. *J. Am. Chem. Soc.* **2006,** *128*, 10258-10267.

128. Simeonov, A.; Nikiforov, T. T., Single Nucleotide Polymorphism Genotyping Using Short, Fluorescently Labeled Locked Nucleic Acid (LNA) Probes and Fluorescence Polarization Detection. *Nucleic Acids Res.* **2002,** *30*, e91-e91.

129. Schwarz, F. P.; Robinson, S.; Butler, J. M., Thermodynamic Comparison of PNA/DNA and DNA/DNA Hybridization Reactions at Ambient Temperature. *Nucleic Acids Res.* **1999,** *27*, 4792-4800.

130. Buttry, D. A.; Ward, M. D., Measurement of Interfacial Processes at Electrode Surfaces with the Electrochemical Quartz Crystal Microbalance. *Chem. Rev.* **1992,** *92*, 1355-1379.

131. Thompson, M.; Kipling, A. L.; Duncan-Hewitt, W. C.; Rajaković, L. V.; Čavić-Vlasak, B. A., Thickness-Shear-Mode Acoustic Wave Sensors in the Liquid Phase: A Review. *Analyst* **1991,** *116*, 881-890.

132. Thompson, M.; Stone, D. C., In *Chemical Analysis: A Series Of Monographs on Analytical Chemistry and Its Application*, Winefordner, J. D., Ed. Wiley: New York, 1997; Vol. 144.

133. Li, X.; Zhan, Z.-Y. J.; Knipe, R.; Lynn, D. G., DNA-catalyzed polymerization. *J. Am. Chem. Soc.* **2002,** *124*, 746-747.

134. Naumkin, A. V.; Kraut-Vass, A.; Gaarenstroom, S. W.; Powell, C. J. *NIST X-ray Photoelectron Spectroscopy Database 20*, 4.1; 2012.

135. Dueholm, K. L.; Petersen, K. H.; Jensen, D. K.; Egholm, M.; Nielsen, P. E.; Buchardt, O., Peptide Nucleic Acid (PNA) with a Chrial Backbone Based on Alanine. *Bioorg. Med. Chem. Lett.* **1994,** *4*, 1077-1080.

136. Pietrzyk, A.; Kutner, W.; Chitta, R.; Zandler, M. E.; D'Souza, F.; Sannicolo, F.; Mussini, P. R., Melamine Acoustic Chemosensor Based on Molecularly Imprinted Polymer Film. *Anal. Chem.* **2009,** *81*, 10061-10070.

137. Šípová, H.; Vrba, D.; Homola, J., Analytical Value of Detecting an Individual Molecular Binding Event: The Case of the Surface Plasmon Resonance Biosensor. *Anal. Chem.* **2012,** *84*, 30-33.

138. Marshall, K. A.; Robertson, M. P.; Ellington, A. D., A Biopolymer by Any Other Name Would Bind as Well: A Comparison of the Ligand-Binding Pockets Of Nucleic Acids and Proteins. *Structure* **1997,** *5*, 729-734.

139. Mateo-Martí, E.; Pradier, C.-M., A Novel Type of Nucleic Acid-Based Biosensors: The Use of PNA Probes, Associated with Surface Science and Electrochemical Detection Techniques. In *Intelligent and Biosensors*, Somerset, V. S., Ed. INTECH, Croatia: 2010; pp 323-344.

140. Egholm, M.; Buchardt, O.; Christensen, L.; Behrens, C.; Freier, S. M.; Driver, D. A.; Berg, R. H.; Kim, S. K.; Norden, B.; Nielsen, P. E., PNA hybridizes to complementary oligonucleotides obeying the Watson–Crick hydrogen-bonding rules. *Nature* **1993,** *365*, 566-568.

141. Wilson, K. A.; Kellie, J. L.; Wetmore, S. D., DNA–protein π-interactions in nature: abundance, structure, composition and strength of contacts between aromatic amino acids and DNA nucleobases or deoxyribose sugar. *Nucleic Acids Res.* **2014,** *42*, 6726-6741.

142. Luscombe, N. M.; Laskowski, R. A.; Thornton, J. M., Amino Acid–Base Interactions: a Three-dimensional Analysis of Protein–DNA Interactions at an Atomic Level. *Nucleic Acids Res.* **2001,** *29*, 2960-2874.

143. Steffen, N. R.; Murphy, S. D.; Tolleri, L.; Hatfield, G. W.; Lathrop, R. H., DNA sequence and structure: direct and indirect recognition in protein-DNA binding. *Bioinformatics* **2002,** *18*, S22-S30.

144. de Ruiter, A.; Zagrovic, B., Absolute Binding-Free Energies Between Standard RNA/DNA Ncleobases and Amino-acid Sidechain Analogs in Different Environments. *Nucleic Acids Res.* **2015,** *43*, 708-718.

145. Pietrzyk, A.; Kutner, W.; Chitta, R.; Zandler, M. E.; D'Souza, F.; Sannicolo, F.; Mussini, P. R., Melamine acoustic chemosensor based on molecularly imprinted polymer film. *Anal. Chem.* **2009,** *81*, 10061-10070.

146. Chelli, R.; Gervasio, F. L.; Procacci, P.; Schettino, V., Stacking and T-shape Competition in Aromatic-Aromatic Amino Acid Interactions. *J. Am. Chem. Soc.* **2002,** *124*, 6133-6143.

147. Anandapadamanaban, M.; Andresen, C.; Helander, S.; Ohyama, Y.; Siponen, M. I.; Lundström, P.; Kokubo, T.; Ikura, M.; Moche, M.; Sunnerhagen, M., High-resolution Structure of TBP with TAF1 Reveals Anchoring Patterns in Transcriptional Regulation. *Nat. Struct. Mol. Biol.* **2013,** *20*, 1008-1014.

148. Kandiah, E.; Trowitzsch, S.; Gupta, K.; Haffke, M.; Berger, I., More Pieces to the Puzzle: Recent Structural Insights into Class II Transcription Initiation. *Curr. Opin. Struct. Biol.* **2014,** *24*, 91-97.

149. Hanwell, M. D.; Curtis, D. E.; Lonie, D. C.; Vandermeersch, T.; Zurek, E.; Hutchison, G. R., Avogadro: an advanced semantic chemical editor, visualization, and analysis platform. *J. Cheminf.* **2012,** *4*, 17-34.

150. Salzner, U.; Aydin, A., Improved Prediction of Properties of π-Conjugated Oligomers with Range-Separated Hybrid Density Functionals. *J. Chem. Theory Comput.* **2011,** *7*, 2568-2583.

151. Akishiba, M.; Takeuchi, T.; Kawaguchi, Y.; Sakamoto, K.; Yu, H.-H.; Nakase, I.; Takatani-Nakase, T.; Madani, F.; Gräslund, A.; Futaki, S., Cytosolic antibody delivery by lipid-sensitive endosomolytic peptide. *Nat. Chem.* **2017,** *9*, 751.

152. de Ruiter, A.; Zagrovic, B., Absolute binding-free energies between standard RNA/DNA nucleobases and amino-acid sidechain analogs in different environments. *Nucleic Acids Res.* **2015,** *43*, 708-718.

153. Meyer, E. A.; Castellano, R. K.; Diederich, F., Interactions with Aromatic Rings in Chemical and Biological Recognition. *Angew. Chem. Int. Ed.* **2003,** *42*, 1210-1250.

154. Boussicault, F.; Robert, M., Electron Transfer in DNA and in DNA-Related Biological Processes. Electrochemical Insights. *Chem. Rev.* **2008,** *108*, 2622-2645.

155. Bisquert, J., Influence of the Boundaries in the Impedance of Porous Film Electrodes. *Phys. Chem. Chem. Phys.* **2000,** *2*, 4185-4192.

156. Uygun, Z. O.; Uygun, H. D. E., A Short Footnote: Circuit Design for Faradaic Impedimetric Sensors and Biosensors. *Sens. Actuators, B* **2014,** *202*, 448-453.

157. Gestwicki, J. E.; Hsieh, H. V.; Pitner, J. B., Using Receptor Conformational Change To Detect Low Molecular Weight Analytes by Surface Plasmon Resonance. *Anal. Chem.* **2001,** *73*, 5732-5737.